
First Optical Lattice Frequency Standard Based on ^{24}Mg Atoms

Der QUEST-Leibniz-Forschungsschule der
Gottfried Wilhelm Leibniz Universität Hannover

zur Erlangung des akademischen Grades

Doktor der Naturwissenschaften
- Dr. rer. nat. -

genehmigte Dissertation von

Dipl. Phys. Dominika Barbara Fim

2021

Referent: Prof. Dr. Ernst M. Rasel
Institut für Quantenoptik
Leibniz Universität Hannover

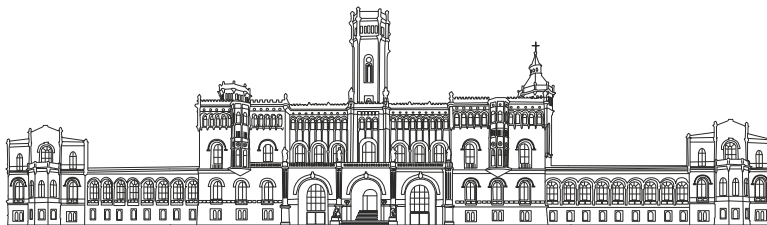
Koreferent: Prof. Dr. Wolfgang Ertmer
Institut für Quantenoptik
Leibniz Universität Hannover

Koreferent: Prof. Dr. Kai Bongs
School of Physics and Astronomy
University of Birmingham

Tag der Disputation: 06. Oktober, 2021

First Optical Lattice Frequency Standard Based on ^{24}Mg Atoms

PhD thesis
Dominika Barbara Fim



QUEST-Leibniz-Forschungsschule
Gottfried Wilhelm Leibniz Universität Hannover

2021

Für Florian und Christian

Abstract

The primary frequency and time standard, defined via a transition frequency of caesium-133, is realized by microwave clocks reaching relative uncertainties in the 10^{-16} level. This performance has been surpassed by state-of-the-art lattice clocks, with transition frequencies in the optical regime, leading to two orders of magnitude lower uncertainties. The key to this performance is the confinement in the *Lamb-Dicke regime* at the *magic wavelength* enabling a Doppler- and recoil-free spectroscopy with a first-order suppressed AC Stark shift.

In atomic clocks, several effects contribute to the uncertainty of the transition frequency. Through continuous global characterization efforts, the individual uncertainty of these effects have been subsequently reduced. Yet one effect, namely the frequency shift induced by blackbody radiation has been identified as a dominant contribution which is difficult to overcome by technical means. In this regard, magnesium-24 excels as a species of choice as its blackbody radiation sensitivity is one order of magnitude lower than in the most frequently used atomic clock species. Furthermore, magnesium offers a relatively simple electronic structure which enables theoretical support through high-precision calculations.

This thesis features the first characterization of a magnesium optical lattice clock operating at the magic wavelength. The characterization of the magnesium frequency standard presented in this thesis depends essentially on the resolution of the transition linewidth, which could be reduced from kHz range to 51(3) Hz in a complementing work. The realization of a transition linewidth with a quality factor of $Q = 1.3 \times 10^{13}$ has contributed to an improved determination of the magic wavelength within this thesis to 468.4106(2) nm. Compared to earlier work, this represents an improvement of two orders of magnitude. Furthermore, the lower transition linewidth also allowed the first observation of the probe AC Stark shift and thus the first characterization of effects in the lattice that falsify the frequency of the trapped magnesium atoms. Overall, the relative uncertainty of the frequency-related effects influencing the clock transition could be determined to be 7.1×10^{-15} . The dominant contributions can be assigned to tunneling broadening and the lattice and probe AC Stark effects, induced by the probe and lattice light. All these effects can be traced back to technical limitations and are part of future work.

Following the characterization, a first frequency comparison between the magnesium lattice clock against the primary frequency standard as well as the ytterbium ion clock at the PTB has been performed and thus a first realization of a lattice based frequency standard with magnesium atoms was demonstrated. The determined transition frequency of 655 058 646 681 864.1(5.3) Hz complies with former measurements.

Key words: optical frequency standard, precision spectroscopy, frequency comparison

Zusammenfassung

Der primäre Frequenz- und Zeitstandard, definiert über eine Übergangsfrequenz des Cäsium-133 Atoms, wird anhand Mikrowellenuhren realisiert, die relative Unsicherheiten im Bereich von 10^{-16} erreichen. Diese Performance wurde durch modernste Gitteruhren mit Übergangsfrequenzen im optischen Bereich, um eine um zwei Größenordnungen geringere Unsicherheit übertroffen. Im Falle sogenannter Neutralatomuhren, wird die Speicherung von Atomen in einem optischen Gitter im *Lamb-Dicke Regime* bei der *magischen Wellenlänge* ausgenutzt, welche eine Doppler- und Rückstoßfreie Spektroskopie mit einer unterdrückten AC Stark Verschiebung in erster Ordnung erlaubt.

In Atomuhren tragen mehrere Effekte zur Unsicherheit der Übergangsfrequenz bei. Eine weltweit kontinuierliche Weiterentwicklung optischer Gitteruhren konnte die Unsicherheit dieser frequenzverschiebenden Effekte reduzieren und ermöglichte eine genauere bestimmung der Übergangsfrequenz. Ein Effekt, nämlich die durch die Schwarzkörperstrahlung induzierte Frequenzverschiebung, wurde als dominanter Beitrag identifiziert und ist anhand von technischen Maßnahmen nur schwer zu überwinden. In dieser Hinsicht zeichnet sich Mg dadurch aus, dass seine Sensitivität auf Schwarzkörperstrahlung um eine Größenordnung geringer ist als bei den am häufigsten verwendeten Uhrenelementen. Darüber hinaus bietet Mg eine relativ einfache elektronische Struktur, welche eine Validierung von hochpräzisen theoretischen Berechnungen ermöglicht.

In dieser Arbeit wurde die erste Charakterisierung einer optischen Gitteruhr basierend auf Magnesium bei der magischen Wellenlänge durchgeführt. Die Charakterisierung hängt im Wesentlichen von der Übergangslinienbreite ab, welche in einer komplementären Arbeiten vom kHz-Bereich auf 51(3) Hz reduziert werden konnte. Die Realisierung einer Übergangslinienbreite von nur 51(3) Hz mit einem Gütefaktor von $Q = 1,3 \times 10^{13}$ hat zu einer um zwei Größenordnungen verbesserten Bestimmung der magischen Wellenlänge, verglichen mit der vorhergehenden Messung, beigetragen. Die verminderte Linienbreite ermöglichte des Weiteren die erste Beobachtung einer AC Stark Verschiebung induziert durch das Spektroskopielicht und ermöglichte somit die erste Charakterisierung von Effekten im Gitter, welche die Frequenz der gefangenen Magnesium Atomen verfälschen können. Die hier erreichte relative Unsicherheit frequenzverschiebender Effekte beträgt 7×10^{-15} . Die dominierenden Limitierungen können auf eine Tunnelverbreiterung und die AC Stark Verschiebung, induziert durch den Spektroskopielaser und das optische Gitter, zurückgeführt werden, welche sich wiederum auf technische Probleme zurück führen lassen. Diese stellen die Themen zukünftiger Arbeit dar.

Die erste vollständige Charakterisierung erlaubte einen Frequenzvergleich zwischen der gitterbasierten Magnesium Uhr und dem primären Zeitstandard sowie der Ytterbium Uhr an der PTB und somit die erste Realisierung eines Frequenzstandards basierend auf einer Magnesium- Gitteruhr. Die hier ermittelte Übergangsfrequenz von 655 058 646 681 864.1(5.3) Hz stimmt mit früheren indirekten Messungen überein.

Schlüsselwörter: Optischer Frequenzstandard, hoch präzise Spektroskopie, Frequenzvergleich

CONTENTS

1	Introduction	3
2	Description of the ^{24}Mg Lattice Clock at the Magic Wavelength	9
2.1	Clock Operation with Magnesium	9
2.2	Experimental Apparatus	11
2.2.1	Vacuum Chamber and Atomic Source	11
2.2.2	Magnetic Fields	13
2.2.3	Detection	15
2.2.4	Singlet MOT	17
2.2.5	Intercombination Transition	18
2.2.6	Triplet MOT	18
2.2.7	Continuous Loading of a Dipole Trap at 1064 nm	20
2.2.8	1D Optical Lattice at the Magic Wavelength	21
2.2.9	Ultra Stable Laser for Clock Spectroscopy	24
2.3	Magnetic Field Induced Spectroscopy	25
2.4	Highest Line Q Value for the Magnesium Clock Transition	27
2.5	Clock Operation	28
3	Systematic Evaluation of the $^1\text{S}_0 \rightarrow ^3\text{P}_0$ Transition Spectroscopy in ^{24}Mg	29
3.1	The Influence of the Polarizability	30
3.1.1	Polarizability Effects I: The Magic Wavelength	31
3.1.2	Polarizability Effects II: Hyperpolarizability	34
3.1.3	Polarizability Effects III: The Probe AC Stark Shift	35
3.1.4	In Situ Measurement of the Probe AC Stark Shift	36
3.1.5	Polarizability Effects IV: Blackbody Radiation Induced Shifts	38
3.2	2nd Order Zeeman Shift	42
3.3	Other Lattice Related Effects	44
3.4	Second Order Doppler Shift	46
3.5	Collisional Frequency Shift	46

3.6	Gravitational Redshift	49
3.7	Summary	50
4	Measurement of the $^1S_0 \rightarrow ^3P_0$ Transition Frequency in Magnesium	53
4.1	The Comparison of Remote Clocks	54
4.1.1	The Transfer Beat	54
4.1.2	Remote Frequency Transfer	55
4.2	Absolute Frequency Measurement of the Magnesium Lattice Clock .	58
4.3	$^{171}\text{Yb}^+ / ^{24}\text{Mg}$ Optical Frequency Measurement	61
4.4	Summary	62
5	Outlook	65
5.1	Reducing the Resolvable Transition Linewidth	65
5.2	Improvement of Systematic Uncertainties	67
5.3	Operational Magic Wavelength	70
5.4	Cooling of Magnesium	72
5.5	Priority recommendation of new implementations at the experiment	75

Introduction

*Never measure anything but
frequencies*

Arthur Schawlow [1]

Units serve to contextualize a value and are firmly integrated into our daily lives. Because of their great importance, they must be [...] *readily available to all, are constant throughout time and space, and are easy to realize with high accuracy.*

- Bureau International des Poids et Mesures, The International System of Units (SI) [2]

This is realized with the help of the international system of units SI¹, which is the most widely used unit system. It derives all physical units from seven basic units: *length* (meter), *mass* (kilogram), *time* (second), *electric current* (ampere), *temperature* (kelvin), *amount of matter* (mole) and the *intensity* (candela).

Through further technical development, clocks, the measuring instruments for elapsed time, were realized more and more precisely. The unit *second* became due to this the unit which could be determined with the highest accuracy and is today the most exactly measurable physical unit. Its current definition was determined by the redefinition during the 13th General Conference on Weights

¹Système international (d'unités).

and Measures (GCPM1) in 1967². Accordingly, the second is determined by the duration of 9 192 631 770 periods of radiation between the transition between the two hyperfine levels of the ground state of the caesium-133 atom [3]. As a consequence, atomic clocks referencing the caesium microwave transition have been setup in national metrology institutes all around the world.

The impressive accuracy that the realization of the second achieved led to the fact that further units were gradually referred to the second by a redefinition. The first of these re-definitions was decided during the 17th General Conference on Weights and Measures in 1983, where the meter has been defined³ to be "the length of the path traveled by light in vacuum during a time interval of 1/299 792 458 of a second" [3].

Another milestone, demonstrating the impact of the second is the redefinition of the base units during the 26th *Conférence Générale des Poids et Mesures* which came into force on 20 May 2019. The units kilogram, ampere, kelvin, and mole have been redefined in terms of the Planck constant (h), elementary charge (e), Boltzmann constant (k_B) and Avogadro constant (N_A), respectively. With the exception of the Avogadro constant, these constants refer to the second. Due to the new definition, 6 of 7 SI base units are now defined in relation to the second and thus also in relation to the frequency of the primary clock [5, 6]. Therefore, frequency measurements constitute the foundation of virtually all physical science.

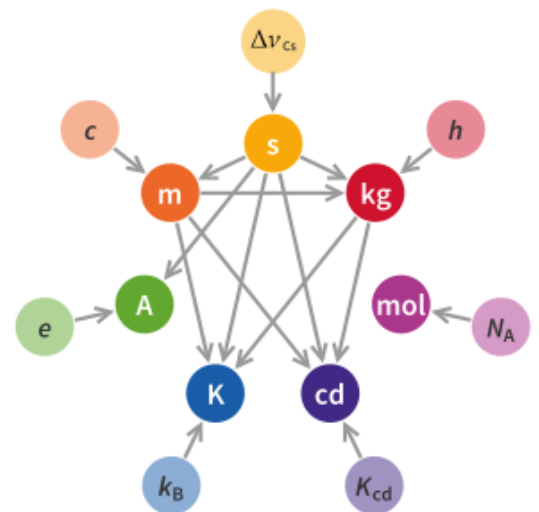


Figure 1.1: Base units of the SI system after the latest redefinition. *Source:* [4]

Optical Atomic Clocks

The unit second is realized by counting periodic events. Counting many cycles increases the accuracy of the frequency measurement. Therefore, higher cycle rates allow in principle faster and more accurate frequency measurements. This

² French: Conférence générale des poids et mesures

³The definition of the meter from 1889, based on the international prototype of platinum-iridium, was replaced in 1960 using a definition based on the wavelength of krypton-86 radiation.

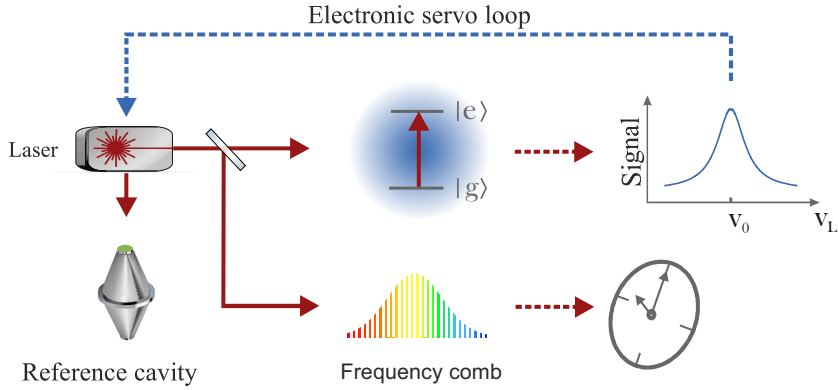


Figure 1.2:

Principle of an optical atomic clock. An interrogation laser is pre-stabilized to an ultra-stable cavity, imprinting its low-noise characteristic on the laser. A further stabilization to an atomic transition enables a long term stability. This stabilization is based on the interrogation of an atomic transition with a narrow linewidth. A detection of the absorption signal can be converted electronically into an error signal offering a correction of the laser frequency within a servo loop. A frequency comb translates the optical laser frequency into a radio frequency.

behaviour can be expressed in terms of the *instability* of an atomic clock which is given by the *Allan deviation* [7, 8]

$$\sigma(\tau) \approx \frac{\Delta\nu}{\nu_0} \frac{1}{(S/N)} \sqrt{\frac{T_c}{\tau}}, \quad (1.1)$$

with the atomic transition frequency ν_0 and the resolved linewidth $\Delta\nu$. Here, S/N denotes the *signal-to-noise ratio*, τ the averaging time and T_c the clocks cycle time. The first term in this equation is called the line quality factor $Q = \Delta\nu/\nu_0$. According to the Allan deviation, the instability gets reduced for higher transition frequencies and/or a reduced resolved linewidth.

Frequencies of forbidden ($^1S_0 \rightarrow ^3P_1$) and strictly forbidden intercombination transition ($^1S_0 \rightarrow ^3P_0$) in alkaline earth metals with frequencies in the optical range are up to five orders of magnitude higher than those of the clock transition used in caesium clocks. This enables them to outperform the performance of microwave clocks.

Initially, optical clocks were implemented using Ramsey-Bordé schemes on free-falling atoms, which extend a Ramsey sequence to compensate for the photon

recoil. Since the spectroscopy was performed on a freely expanding atomic ensemble, the residual velocity of the atomic cloud led to a first-order Doppler shift, limiting the performance of such clocks. At that time, this effect was largely suppressed in ion-based optical clocks trapped in so-called Paul traps. In these traps ions are confined in a varying electromagnetic quadrupole potential via the Coulomb force in a volume with an expansion smaller than half of the transition wavelength in the presence of a nearly negligible trapping-field [9, 10, 11]. Both are the main requirements for Lamb-Dicke spectroscopy, where a Doppler- and recoil-free interrogation is enabled [12].

In 2005 H. Katori proposed a technique enabling Lamb-Dicke spectroscopy also with neutral atoms [13]. In order to capture the atoms in a sufficiently small area, he suggested using an optical lattice confinement generated by a retro-reflected laser beam. In order to minimize AC Stark shifts induced by the trapping laser during spectroscopy, this laser has to be operated at the *magic wavelength*⁴. This technique enabled optical lattice clocks based on neutral atoms to overcome the limitations imposed by Doppler broadening for the first time.

By now, optical lattice clocks are operating on the strictly forbidden clock transition $^1S_0 \rightarrow ^3P_0$ of alkaline earth(-like) elements with natural linewidth in the sub-Hertz regime. Among various frequency shifting effects such as the Zeeman effect, density dependent effects and the AC Stark effect, the shift induced by blackbody radiation (*BBR*) is the most important contribution to the uncertainty of state-of-the-art clocks. Nevertheless, an impressive improvement on the control of these effects led to the realization of optical lattice clocks reaching relative accuracies in the low 10^{-18} [14, 15].

Motivation for a Lattice Clock Based on Magnesium

Optical lattice clocks based on elements such as *strontium* (Sr), *ytterbium* (Yb), *mercury* (Hg) and also *magnesium* (Mg) are set up all around the world. Compared to ytterbium or strontium, magnesium features an one order of magnitude smaller sensitivity to frequency shifts induced by the blackbody radiation [16, 17]. Additionally, the relative simple electronic structure of Mg allows the development of a high-precision relativistic model, leading to more accurate values for the blackbody radiation shift compared to the theoretical predictions of other clock species.

⁴The magic wavelength is defined as the wavelength where the differential polarizability of both involved atomic states vanish in first order.

A further remarkable feature of the bosonic isotope of magnesium is the strictly forbidden clock transition $^1S_0 \rightarrow ^3P_0$. An interrogation of this transition becomes possible by magnetic field induced spectroscopy [18]. Here, a magnetic field enables the clock transition via state mixing. The resulting adjustable transition linewidth can be arbitrary small such as a few tens of μHz , representing the smallest clock transition among the above mentioned clock species. A drawback of this method is an additional second-order Zeeman frequency shift. The realization of a lattice clock based on magnesium also entails challenges such as the lack of suitable sub-Doppler cooling techniques, ionization processes occurring while operating the MOT and the magic wavelength lattice, and its low mass demanding a high trap depth for sufficient suppression of tunneling effects in the lattice environment. Nevertheless, in 2011, the first magnesium optical frequency standard with a Ramsey-Bordé scheme on free-falling atoms was demonstrated, reaching an accuracy of 7×10^{-14} . In order to avoid limitations by the first-order Doppler-effect, an optical lattice was set up within the scope of the work of [19] and [20] in which magnesium atoms could be captured for the first time. The resolution of the linewidth has been treated in [21] and [22], whereby finally a linewidth of 51 Hz could be realized representing the starting point of this work.

Outline of This Thesis

The highest line quality factor $Q = \nu/\Delta\nu$ observed with magnesium atoms is approximately 1.3×10^{13} and was realized within [22]. This paved the way for the achievement of two important milestones for an optical lattice clock based on magnesium atoms within this thesis: (i) the first fully systematic evaluation of the magnesium lattice clock and (ii) the first frequency comparison of a magnesium lattice clock. Hereby, the frequency of the strictly forbidden clock transition $^1S_0 \rightarrow ^3P_0$ was absolutely measured for the first time resulting in an accuracy improved by one order of magnitude compared to former measurements on the $^1S_0 \rightarrow ^3P_1$ transition.

This thesis is organized as follows: In **Chapter 2**, the apparatus for trapping magnesium in the magic lattice is presented. **Chapter 3** focuses on the characterization of the lattice clock and gives a detailed description of effects to which the clock is sensitive. **Chapter 4** describes the remote frequency comparison and the achieved total uncertainty of the clock. **Chapter 5** finally gives an outlook on

future perspectives of the magnesium lattice clock on how to make Mg competitive with state-of-the-art devices.

Description of the Magnesium Lattice Clock at the Magic Wavelength

Before exploring effects that have an impact on a clock's transition frequency and therefore influencing the accuracy of a clock, I will discuss the experimental realization of a lattice clock based on the bosonic isotope of magnesium in this chapter. The main characteristics of alkaline-earth (-like) elements will be explained first, followed by the most important devices as well as steps for the realization of a magnesium lattice clock. At the end of this chapter, I will present the result of this apparatus with the smallest transition linewidth achieved so far with magnesium, yielding to the highest line quality factor of $\approx 1,3 \times 10^{13}$.

2.1 Clock Operation with Magnesium

Magnesium exists in three stable Isotopes, the bosonic isotope ^{24}Mg with a abundance of 78.99 %, the fermionic isotope ^{25}Mg with a natural abundance of 10.00 % and a second bosonic isotope ^{26}Mg with a natural abundance of 11.01 % [23]. Due to the lower abundance, the second bosonic isotope ^{26}Mg will not be further discussed in this thesis.

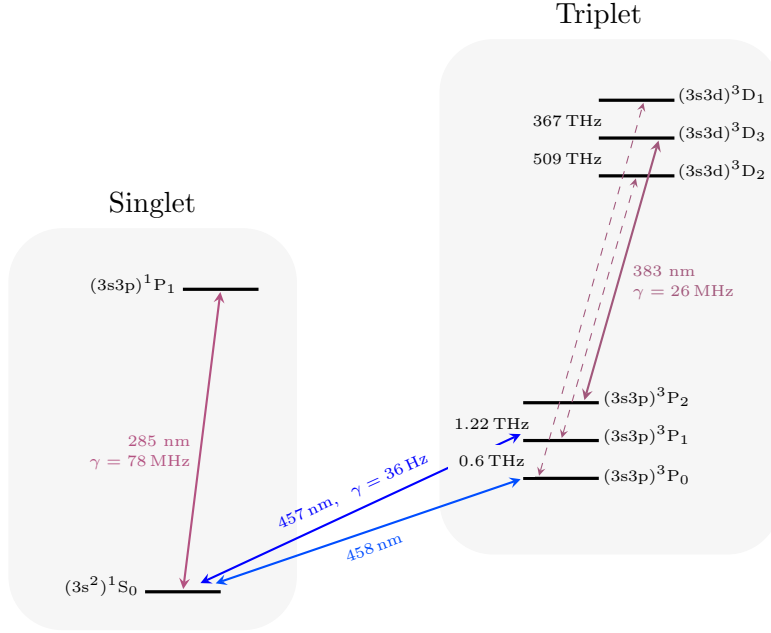


Figure 2.1:
Extract of the relevant level scheme of ^{24}Mg with cooling and repumping transitions (magenta), intercombination transition (blue) and the $^1\text{S}_0 \rightarrow ^3\text{P}_0$ clock transition (cyan). All transitions are given in $\Gamma/2\pi$ and are addressed by laser.

Both remaining isotopes provide two strong transition lines for cooling, shown in figure 2.1. The cooling transition in the singlet system $^1\text{S}_0 \rightarrow ^1\text{P}_1$ is 78 MHz broad, the second one is 26 MHz broad and can be found in the triplet manifold at the $^3\text{P}_2 \rightarrow ^3\text{D}_3$ transition. The intercombination transition $^1\text{S}_0 \rightarrow ^3\text{P}_1$ is only 36 Hz narrow. This transition rate does not provide enough scattering processes to trap atoms against gravity. The triplet system provides a fine structure resulting in a splitting of the triplet ground state 3P into three states $^3\text{P}_0$, $^3\text{P}_1$ and $^3\text{P}_2$. These states are called metastable due to their lifetime of 4.4 ms [24] for the $^3\text{P}_1$ state and 38 min [25] for the $^3\text{P}_2$ state.

After magnesium atoms are cooled by a two-stage MOT, the atoms need to be transferred to the optical lattice. To avoid light shifts induced by the trapping field, light at the magic wavelength has to be used which was predicted for magnesium to be at 468.45(23) nm by M. Safronova [26].

Alkaline earth metals such as magnesium have an even atomic number Z . For bosonic isotopes, the atomic number and also the mass number are even, which

leads to a spinless nuclear momentum I . Therefore hyperfine splitting ($F = I + J$), only emerge in fermionic alkaline earth metals. The resulting hyperfine mixing couples the 3P_0 to the 3P_1 state, leading to a non-vanishing transition probability for the $^1S_0 \rightarrow ^3P_0$ transition and a linewidth of the order of μHz . For bosons, this intercombination transition stays strongly forbidden due to the absence of a nuclear spin. The clock transition of the bosonic magnesium $^1S_0 \rightarrow ^3P_0$ is therefore strongly forbidden.

Nevertheless, applying an external homogeneous magnetic field will mix the 3P_1 to the lower clock state 3P_0 and introduce an adjustable transition rate, proposed by Taichenachev [18]. The drawback of this is a Zeeman shift, which needs to be controlled. This will be further discussed in chapter 3. This work was performed with the bosonic isotope, even if clock operation with the bosonic isotope involves the control of a magnetic field applied during spectroscopy resulting in an additional systematic and uncertainty contribution. Cooling of the fermionic isotope leads to more stringent requirements for the cooling laser.

2.2 Experimental Apparatus

In this section I will at first discuss the main devices necessary for the operation of a bosonic magnesium lattice clock, like for example the science chamber or coils used for generating magnetic fields. Later on I will present the laser sources used in our experiment together with the implemented improvements of the overall system.

2.2.1 Vacuum Chamber and Atomic Source

Experiments based on cooled atoms are performed in vacuum chambers to minimize collisions between trapped and cooled atoms and background gas particles. Collisions can lead to losses by kicking out trapped atoms and induce frequency shifts. The requirements on the gas pressure in the chamber are given by the application.

In the Magnesium experiment the vacuum chamber consists of two chambers, the source chamber and the main chamber, connected via a 5 mm diameter aperture, allowing to have a high vapor pressure on the source side and a high vacuum in

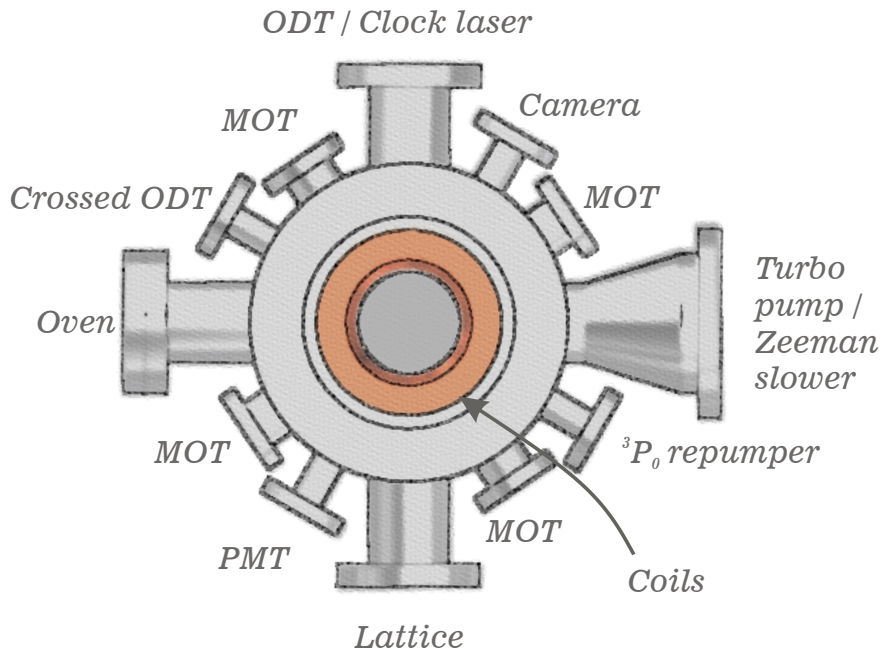


Figure 2.2:

View from top on the main science chamber with viewports denoted by their application. For Zeeman slowing only a beam is applied exploiting the field gradient created by the MOT coils. The beams used for both MOT's are overlapped by means of dichroic mirrors and are using the same viewport except for the $^3\text{P}_0$ repumper. The lattice is contrary overlapped with the ODT and clock laser. Apart from the spectroscopy signal a Camera is used for imaging. The PMT is optimized for low noise detection of the spectroscopic signal. Not shown is a Kapton film shutter placed inside the chamber in front of the oven for reduction of collisions between atoms from the thermal atom beam and the atoms in the center of the chamber.

the main chamber. The source chamber is basically a DN63CF T-piece adapter, pumped via a turbomolecular pump¹ with a pumping speed of 60l/s connected via a DN40CF flange.

The main chamber, showed in figure 2.2, is basically a 210 mm diameter stainless steel cylinder sealed with DN200CF flange with viewports for optical access. Opposite the source chamber a DN63Cf flange connects the main chamber to a cross, connecting a turbomolecular pump² with a pumping speed of 200l/s and an ion getter pump³ with a pumping speed of 120l/s, a vacuum sensor⁴ and an optical viewport for irradiating light used for Zeeman slowing. Additionally ten hollow cylinders are mounted to the vacuum chamber, with eight optical viewports connected via a DN40CF flange and two DN63CF flanges with two additional viewports for optical access.

The oven inside the source chamber is made of a cylindrical steel reservoir, closed by a drilled-out M8 × 10 screw and heated up to 440 degrees by a heating cartridge [27, 28]. A miniaturized atomic source was developed in [29] with a distance to the center of the main chamber of 165 mm in order to increase the solid angle for a sufficient loading of the MOT.

2.2.2 Magnetic Fields

In atomic experiments magnetic fields are applied in different configurations for different applications. For MOT cooling for example a quadrupole field is needed for local spacial enclosure whereas during magnetic field induced spectroscopy homogeneous fields are required. On the other side, additional stray fields like the earth-magnetic field or fields arising by the ion getter pump interfere with the well designed quadrupole or homogeneous field, which needs to be minimized. The undesired magnetic fields can be reduced by utilizing compensation coils.

Quadrupole Field

As a consequence of the Earnshaw's Theorem for trapping atoms in a magneto optical trap, a quadrupole field is required, where the minimum of the magnetic field is overlapped with the crossed cooling lasers [30]. Magnetic fields can be

¹TMU 071 P, Pfeiffer

²TMU 260, Pfeiffer

³StarCell, VacIon Pump, Varian

⁴Balzer

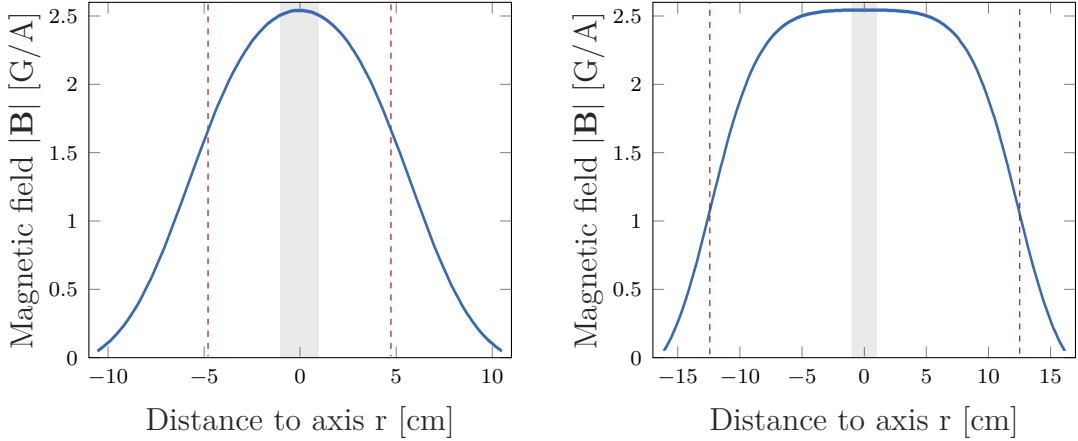


Figure 2.3:

Homogeneous magnetic field applied for state mixing resulting from the MOT coils (*left*) and the new pair of coils being optimized for a homogeneous field (*right*). A distance of 1 cm away from the center is shown via the gray bar. The red dashed line indicates the distance of the coils in respect to the center. *Source:* [22].

generated by current flow through two parallel coils. In the *Anti-Helmholtz configuration*, where the current flow is counter-propagating and the distance between the coils is equal to the coil radius, the generated magnetic field will have a zero field strength in the center between the coils. In case where the current flow direction is some for both coils, a homogeneous magnetic field can be generated. This configuration is called *Helmholtz configuration*.

The quadrupole coils are placed close to the view ports mounted in the DN200CF flange. This flange is embedded in the main chamber where a distance between the coils and the minimum of the magnetic field of only 4 cm has been achieved. The coils are wounded by 33 layer and are connected to a power supply delivering maximum 200 A resulting in a 500 G magnetic field in the strong direction and 250 G in the weak direction. Since the magnetic field has a linear increase over an area of around 4 cm, consequently a magnetic field gradient of 131.5 G/cm results at zero position [27]. Because current flow heats up the coils, tubular cooper wire are used for water cooling. The applied water pressure is around 10 Bar reducing the final temperature to 55 °C during continuous operation at 200 A.

Homogeneous Magnetic Fields

For many applications like measurements of the second order Zeeman shift, homogeneous magnetic fields are necessary. In the magnesium experiment this can

be generated by switching the current flow of one coil, used for the quadrupole field, from *Anti-Helmholtz* to *Helmholtz configuration*. For this purpose four IGBT (*Insulated Gate Bipolar Transistor*) are connected in a so-called *H-bridge* circuit where the current flow in either direction can be created. The IGBT enables a switching within 30 μs . Nevertheless, eddy currents created by fast switching off limit the coil regulation to 2 ms [7].

The main application of this coil pair is the trapping within the MOT and therefore the coils were optimized for the magnetic field gradient by means of the distance of the coils and not for a homogeneous magnetic field, where they generate 2.49 G/A measured by Zeeman spectroscopy of the $^1\text{S}_0(m_J = 0) \rightarrow ^3\text{P}_1(m_J = \pm 1)$.

Since the spectroscopy of the atoms is performed within the optical lattice, which itself is loaded from a dipole trap at 1064 nm, the atoms can be distributed within the Rayleigh range of the dipole trap of more than 2.5 cm. This requires a magnetic field with a homogeneity of at least the same area. Therefore a new pair of coils has been set up consisting of a copper band measuring 15 mm \times 0.3 mm. The copper band can be operated with a maximal current of 30 A. The coils are placed around the main science chamber leading to a diameter of 253 mm with a distance of 134 mm and a thickness of 4 mm. The coils have also been characterized via the magnetic sub- levels $m_J = 0, \pm 1$ of the $^1\text{S}_0 \rightarrow ^3\text{P}_1$ transition, giving a magnetic field strength of 0.6569(2) G/A [22].

Homogeneous Magnetic Field for Stray Field Compensation

As mentioned before, stray magnetic fields can manipulate well designed magnetic fields or influence atomic spectra. Therefore three additional coil pairs are placed around the vacuum chamber in all three dimensions.

The coils are made of 25 windings per each dimension around a cage with a size of 30.5 cm. By applying a current of 1.5 A a magnetic field strength of 1 G can be created with a homogeneity better than 25 % in an area of ± 5 mm. The coil current has been optimized within this thesis for canceling the earth magnetic field measured via the $^1\text{S}_0 \rightarrow ^3\text{P}_1$, $m_F = \pm 1$ magnetic field sensitive transition. Also a stabilization was developed to ensure a stable and drift free magnetic field.

2.2.3 Detection

Detection of atoms can be performed by either a fluorescence or by absorption detection. In the later an atomic cloud is illuminated by a detection beam creating

a shadow through absorption which is detected on a CCD camera. For this detection method, a sufficient dense cloud is required. Whereas, fluorescence detection is based on displaying emitted photons traveling in the direction of the imaging system which can be used also with dilute gases.

Detection via a CCD Camera

In the magnesium experiment detuned light is already used for MOT cooling, thus only detecting the emitted photons has to be performed. The implemented imaging system is creating a 1:1 display on a CCD chip of an ultraviolet (UV) sensitive CCD camera⁵.

The required light power for detection can be estimated by the photon scattering rate γ_{sc} and the saturation parameter s [31]. In steady state the number of excited state atoms in a two level system is given by

$$\rho_e = \frac{s/2}{1 + s + (2\Delta/\Gamma)^2}, \quad (2.1)$$

with $\Delta = 2\pi(\nu_{\text{Laser}} - \nu_{\text{Atom}})$ the detuning, Γ the linewidth and the saturation parameter $s = I/I_s$ given by the intensity of light I and the saturation Intensity $I_s = \frac{\pi\hbar c}{3\tau_e\lambda^3}$ with $\tau_e = 1/\Gamma$ the life time of the excited state. The photon scattering rate results from the excited state population times the linewidth

$$\gamma_{\text{sc}} = \Gamma\rho_e = \frac{s\Gamma/2}{1 + s + (2\Delta/\Gamma)^2}. \quad (2.2)$$

In the case where $s \ll 1$ most atoms will be found in the ground state. Whereas, both states are equally filled if $s \gg 1$. Varying the saturation parameter in equation 2.2 and letting it evolve to infinite, one will find the photon scattering rate is limited by the lifetime of the atomic state $\gamma_{\text{sc}}^{s \rightarrow \text{inf}} = \frac{\gamma}{2}$ leading to saturation broadening for intensities higher than the saturation intensity.

Fluorescence Detection via a PMT

In clock spectroscopy shot to shot fluctuation of the atom number during detection reduces signal-to-noise ratio (SNR) of the detected signal. Detecting both, the excited atomic fraction and also the fraction remained in the ground state, the signals

⁵MaxCam, Finger Lakes Instrumentation combined with a "back-thinned" CCD47-10 Chip, Marconi

can be normalized to improve the signal to noise ration. The CCD camera used in our experiment can not shoot fast enough in order to detect the ground state and the excited atoms without increasing the time of the experimental sequence. Instead, we set up a photo-multiplier tube (PMT) for detecting the spectroscopic signal. For reduction of stray light the scattered detection light is collimated at first by a lens with a focal length of $f = 75$ mm and afterwards passing an aperture at the position of the focus.

2.2.4 Singlet MOT

Cooling of magnesium is performed at first on a strong transition in the singlet system $^1S_0 \rightarrow ^1P_1$, called singlet-MOT or S-MOT. This transition has a linewidth of 78 MHz corresponding to a Doppler-limit of 1.9 mK. In the fermionic isotopes where a hyperfine structure is present, temperatures below the Doppler-limit are observable.

The singlet-MOT is operated at 285 nm. With adequate diode laser sources unavailable, we are using a commercial laser unit generating light at 1140 nm by an ECDL (*External Cavity Diode Laser*) amplified by a Raman fiber amplifier (RFA) and frequency doubled to 570 nm⁶ [19]. Finally, we are using a self-built bow-tie SHG (*second harmonic generation*) to further frequency double the light to 285 nm. Typically, the commercial unit is operated at powers below 3 W. A small amount of light is fiber guided through a polarization maintaining (PM) fiber to an iodine spectroscopy cell in order to stabilize the unit by means of a Doppler-free polarization spectroscopy, set up by M. Riedmann [32]. The linewidth achieved by the stabilization is a few MHz narrow, sufficient for cooling on the 78 MHz broad transition.

The maximum generated UV light at 3 W amplifier power is around 350 mW in the UV. At first, this amount of power is not necessary for operating the MOT in the singlet system. The second, UV radiation acts aggressively on coated surface leading to faster degradation of the generated power. Therefore in order to operate the experiment with stable conditions, the amplifier power is leveled to a SHG output power of 100 mW.

The generated UV light is split by an *acousto-optical modulator* (AOM) into two parts. The 0th diffraction order is used for Zeeman slowing. It is guided to a

⁶DL-RFA-SHG Pro, Toptica

second AOM, detuned by -220 MHz and further guided through a viewport into the chamber, counter propagating the atomic beam. The -1^{st} diffraction order is frequency shifted by -78 MHz corresponding to γ and splitted into 6 beams by *polarizing beam splitters* (PBS) and further guided to the science chamber in three dimensions counter propagating respectively. With this configuration we are able to trap and cool down 10^9 atoms to temperature of 3 mK.

2.2.5 Intercombination Transition

The intercombination transition is only 36 Hz broad and thus is not sufficient for laser cooling or narrow line transition cooling. This transition is only used to drive atoms to the triplet manifold, where they are further cooled down. This transition is driven by a Toptica unit⁷ consisting of an ECDL at 914 nm and a frequency doubling stage to generate light at 457 nm. The typical output power is 200 mW. The available light is splitted by the means of a PBS, where one part is at first guided through a double pass AOM and subsequently fiber guided to an *Ultra Low Expansion* (ULE) glass cavity. The special feature of ULE is its low thermal expansion at room temperature and therefore a reduced sensitivity to length changes for temperature fluctuations. By stabilizing the frequency of the 457 nm laser via the *Pound-Drever-Hall* (PDH) technique the laser linewidth can be reduced to approximately 30 Hz. The second part, splitted at the PBS, passes an AOM operated at -79 MHz and is then fiber guided to the experimental chamber. Finally 30 mW are available for optically pumping the atoms from the singlet manifold into the triplet manifold.

2.2.6 Triplet MOT

To further cool down the atoms a second cooling stage is applied in the triplet manifold at the $^3\text{P}_2 \rightarrow ^3\text{D}_3$ transition. The Doppler-limit for this transition is with $616 \mu\text{K}$ slightly below the first cooling stage. Nevertheless, the size of the triplet-MOT is $500 \mu\text{m}$. This is 5 times smaller compared to the singlet-MOT and is therefore more suitable for loading of follow-up optical traps, which is in our case an optical dipole trap.

⁷TA-SHG-110, Toptica Photonics

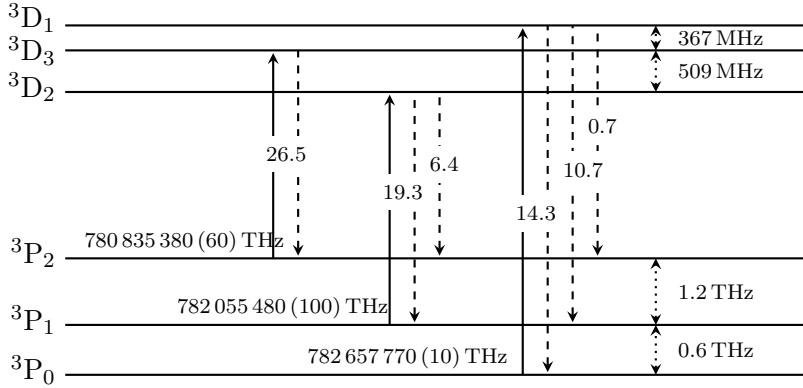


Figure 2.4:

Level scheme of the triplet system with laser driven transitions (*solid line*) and decay channel (*dashed line*). Transition frequencies are given in THz while transition linewidth $\gamma = \Gamma/2\pi$ are given in MHz placed on the transition lines [7]. The finestructure splitting is given on the right side depicted by dotted lines.

Once atoms are transferred to the triplet manifold, one cooling laser and two repumper are applied. The cooling transition ${}^3P_2 \rightarrow {}^3D_3$ in the triplet manifold is a closed transition, but at high detuning off-resonant excitation to the 3D_1 and 3D_2 state is possible [32]. To avoid atoms decaying into the states 3P_1 and 3P_0 and getting lost out of the cooling cycle, both repumper are irradiated to bring these atoms back into the cooling cycle.

The energy spacing between the transitions in the triplet states is shown in figure 2.4, whereas the necessary light can not be provided by one laser. The Laser system for the T-MOT was build in [33, 34] and consists of three master ECDL at 766 nm injecting *tapered amplifier* (TA). The laser are based on a grating creating a cavity with some light fed back to the optical medium in the laser diode and the first diffraction order to couple out of the resonator, in the so-called Littrow design. The frequency can be aligned by the angle of the grating respectively to the laser diode. For this purpose a fine-thread screws are implemented to tilt the grating combined with a *stack piezo* driven by a high voltage piezo driver. To avoid damage of the laser diode by back-reflections, an optical isolator is placed directly behind the laser. The generated light injects a tapered amplifier to enhance the light from 50 mW to around 1 W. The light is further frequency doubled via a frequency doubling stage built and described by [33] and [34]. The power

enhancement necessary for efficient frequency doubling is provided by a *bow-tie*-cavity avoiding a standing wave in the crystal. The nonlinear medium generating the frequency doubled light is a LBO crystal. The LBO is biaxial crystal, where phase matching is ensured by the crystals angle and temperature, regulated by a temperature controller and a peltier element.

Light at 383 nm generated by the SHG is coupled through an AOM for optical switching purpose, splitted after the AOM into six beams for MOT cooling and fiber guided to the vacuum chamber. With this setup we are finally able to trap around 10^8 atoms at 1 mK.

2.2.7 Continuous Loading of a Dipole Trap at 1064 nm

The lack of sub-Doppler cooling in the MOT, ionization of the upper ^3D states in the presence of light at the magic wavelength and also density limitations by light-assisted two-body collisions in the T-MOT gives strong challenges for a sufficient loading of an optical dipole trap at the magic wavelength. A continuous loading scheme of a dipole trap at 1064 nm developed by M. Riedmann [32, 35] overcomes this limitations and enables a transfer of 10^5 atoms into the dipole trap which allows for the subsequent loading of 10^4 atoms into the magic wavelength lattice.

The dipole trap is realized by an ytterbium doped fiber laser (*YLM, IPG Photonics*) with 48 W maximum output power at 1064 nm, fiber guided to the science chamber and focused down to $72\ \mu\text{m}$, yielding a maximum trap depth of $U_0/k_b = -142\ \mu\text{K}$. The optical dipole trap sequentially separates the laser light from the T-MOT and the lattice phase and thus avoids the temporal overlap of both and therefore ionization. For the continuous loading of the dipole trap, the Zeeman-slower, S-MOT, intercombination laser and T-MOT are driven simultaneously, but without the $^3\text{P}_0$ repumper. The lack of the repumper creates a loss channel in the T-MOT, whereby a quasi continuously loading of the $^3\text{P}_0$ atoms is achieved and overcomes the density limit, yielding around 10^5 atoms at $100\ \mu\text{K}$ trapped in the ODT.

A spectroscopy of the clock transition where atoms get excited from the ground state has the advantage of a better signal to noise ratio. Therefore, atoms captured in the ODT in the $^3\text{P}_0$ are transferred previous to the spectroscopy into the $^3\text{D}_J$ -states where they further decay to the ground state via the intercombination transition.

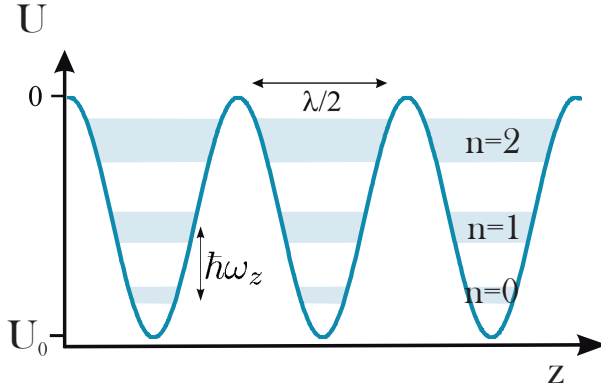


Figure 2.5:
Axial lattice potential with periodicity of $\lambda/2$ and n vibrational bands (blue-shaded).

2.2.8 1D Optical Lattice at the Magic Wavelength

Atoms trapped in an optical lattice experience a trapping force resulting from the optical potential given by the dipole trap. The potential $U(r, z)$ created by an optical lattice and hence by a retro-reflected laser beam can be described by

$$U(r, z) \approx -U_0 e^{(-2r^2/w^2(z))} \cos(k_L z) + mgh, \quad (2.3)$$

with the trap depth U_0 , the Gaussian dependence on the radial distance to the lattice axis $r = \sqrt{x^2 + y^2}$ and the beam waist $w(z) = w_0 \sqrt{1 + (\frac{z}{z_0})^2}$, as well as the periodicity in the z -direction depending on the lattice wave number ($k_L = 2\pi/\lambda$), given by the interference pattern. The standing wave forms nodes and potentials. Atoms are trapped in the antinodes which can have different height and hence different gravitational potential, described by the last term in the equation. The effect of the polarizability on the trap depth is $U_0 = 4P\alpha_i/(\pi c\epsilon_0 w(z)^2)$.

The atoms experience a potential, created by the optical lattice which is leading to a tight confinement along the direction of the axis, whereas a weak confinement in the radial direction. In the case where the confinement in the axis direction fulfills the Lamb-Dicke criterion $\eta = \sqrt{\frac{w_R}{w_z}} \ll 1$ a Doppler- and recoil-free spectroscopy can be performed. This is the case, when the axial trap frequency ω_z is bigger than the recoil frequency ω_R . The first spectroscopy of magnesium atoms in the Lamb-Dicke regime was performed by T. Wübenna [19]. Further investigations performed by A. Kulosa have been directed to tunneling effects in shallow lattices and their influence on the carrier line-shape [21].

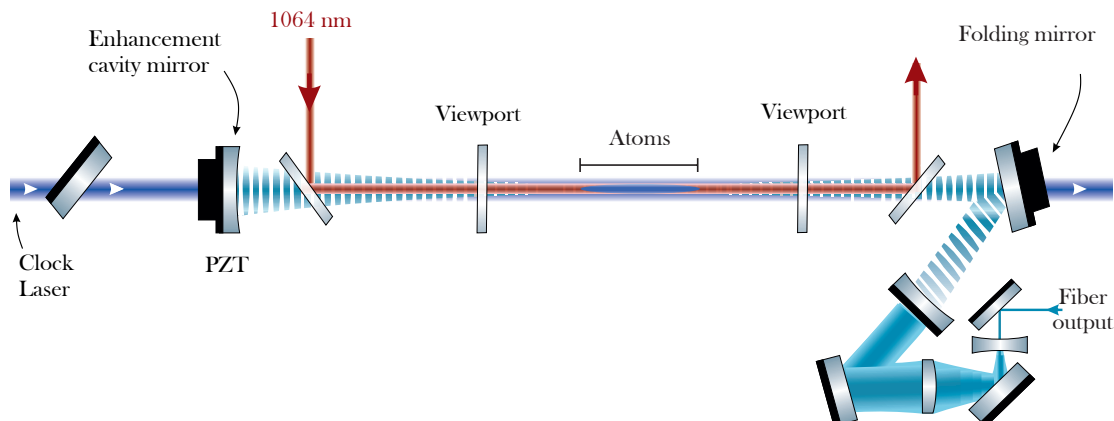


Figure 2.6:
Schematic of the enhancement cavity set up for the magic lattice. The enhancement cavity is realized within a folded design outside the chamber. Between the science chamber viewports and the enhancement cavity, dichroic mirrors are placed for overlapping the optical lattice and the ODT at 1064 nm. The clock laser is pointing opposite to the lattice laser and was supposed to be fully transmitted through the folding mirror, which however turned out to be not the case. A deeper discussion on the implications can be found in section 3.1.3.

Magnesium's low atomic mass and short magic wavelength requires strong trap depths of the optical lattice for sufficient suppression of tunneling and the resulting broadening of the transition linewidth [21]. A high power laser source is generating light at the magic wavelength by means of a frequency doubled titanium-sapphire⁸ (Ti:Sa) laser pumped by a Verdi G12⁹, providing 12W at 532 nm. The Ti:Sa provides roughly 1W at 936 nm which is further frequency doubled by a SHG¹⁰ to 400 mW at 468 nm. After passing an AOM for intensity modulation and an EOM for sideband modulation for a later stabilization, it is fiber guided to the science chamber, where 240 mW are available for the generation of an optical lattice.

The frequency of the Ti:Sa laser itself is stabilized to the clock laser via a transfer cavity with a mode spacing of around 100 MHz [36]. The frequency selection of the Ti:Sa laser is limited according to this spacing. The implementation of an AOM in double-pass configuration in the near future will enable to tune the frequency of the system closer to the magic wavelength.

⁸TIS-SF-07, Tekhnoscan

⁹Verdi G12, Coherent

¹⁰SHG Pro, Toptica

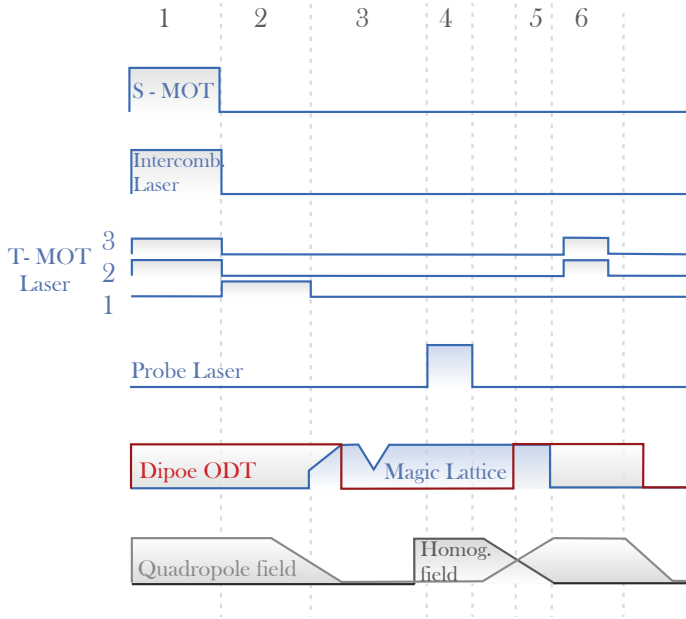


Figure 2.7:

Experimental sequence of the preparation of magnesium atoms, clock spectroscopy and detection. *Zones*: 1. Continuous loading to the ODT at 1064 nm 2. Optical pumping to the 1S_0 ground state. 3. Transfer to the optical lattice at 468 nm and release of hot atoms by trap depth variation. 4. Interrogation pulse and homogeneous magnetic field applied. 5. Transfer to the ODT at 1064 nm and 5. detection of excited atoms via T-MOT.

The easiest way to generate an optical lattice is to retro-reflect laser light whereby the counter propagating waves create an interference pattern with potential minima and maxima. Depending on the detuning of the trapping wavelength atoms can be captured either in blue or red detuned traps. The trapping force the atoms experience is proportional to the lattice power.

An optical lattice for magnesium generated only by back-reflection is not sufficient for Lamb-Dicke spectroscopy of magnesium at the available laser power. But with the addition of a cavity utilized for enhancement of the in-coupled light to higher circulating intracavity powers, sufficient high trap depths have been realized. The enhancement cavity was set up and is described in more detail by [20] and [19]. To summarize both, a horizontal 1D optical lattice placed around the science chamber shown in figure 2.6 is created within a folded cavity design. The folded design enables an enhancement of the lattice light at 468 nm and was supposed to couple out the probe light at 458 nm by a dichroic mirrors coated highly reflective for 468 nm and highly transmitted for light at 458 nm. Since the lattice is loaded from the ODT, a spatial overlap between both needs to be ensured, which is realized by dichroic mirrors placed inside the cavity.

The stabilization of the lattice to the enhancement cavity is performed by the PDH technique using sidebands generated by the EOM, mentioned above. The highest circulating power reached with this setup was roughly 8 W. Unfortunately,

the transmission of the viewports is degrading by applying such high laser powers, leading to decreased enhancement given by the cavity. The reason for this is not fully understood until now, but we could observe coating damage on the inside of the vacuum windows. One explanation can be light enhanced deposition of magnesium on the viewport surface. Nevertheless, the enhancement factor during the measurements of this thesis was typically 25.

The transfer of atoms from the ODT into the magic lattice is performed within an overlapping time of 50 ms between both. The whole loading sequence is shown in 2.7. After the dipole trap is switched off, the hottest atoms trapped in the lattice get released by adiabatically ramping down the trap in 100 ms to 1.5 W circulating power and up again to the operating power resulting in 1000 atoms [21] and ensure the same atomic temperature and the same atomic condition for subsequent experiments.

After the spectroscopy pulse the atoms get transferred back into the ODT. By applying the triplet MOT, excited atoms get detected. A subsequent resonant blow away pulse now clears the atoms on the excited states. The remaining ground state atoms get optically pumped back to the triplet manifold via the intercombination transition and are also detected for normalization purpose. After another blow away pulse a third detection is applied for a background detection [22].

2.2.9 Ultra Stable Laser for Clock Spectroscopy

The laser system used for probing the clock transition is operated at 916 nm which is generated via an ECDL in Littman design. The output power of the laser is enhanced by a tapered amplifier, where one part is fiber guided for stabilization purpose to the ultra stable resonator, consisting of a 10 cm long mushroom design cavity made of ULE glass with a finesse $\mathcal{F} \approx 600,000$, shown in figure 2.8. The laser is stabilized via the *Pound-Drever-Hall* (PDH) technique yielding an instability of $\sigma_y(1s) = 5 \times 10^{-16}$. Two identical system have been set up for the purpose of comparison by A. Pape [37] and further improved by S. Rühmann [38] in terms of stability.

The second part of the enhanced light is fiber guided via a 30 m long polarization maintaining fiber to the lab where the science chamber is placed and is again enhanced in term of power via a tapered amplifier yielding ~ 800 mW at 916 nm. The

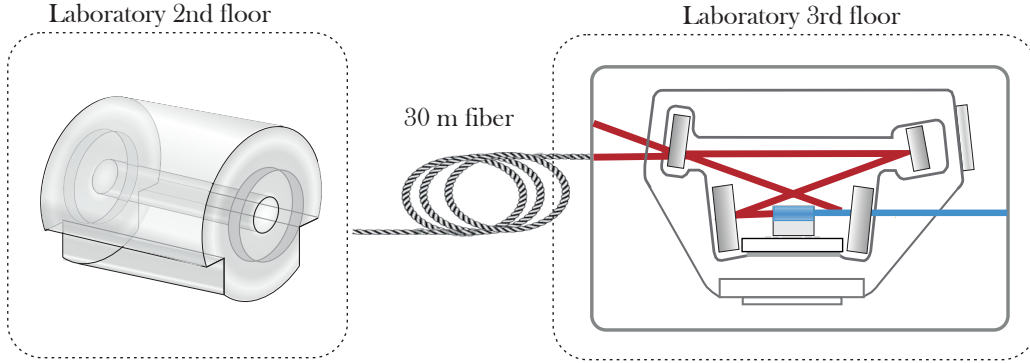


Figure 2.8:

Schematic Scheme of the clock laser setup including the ULE Resonator in mushroom design and commercial frequency doubling stage. The light is fiber guided between two laboratories from the cavity to the SHG via a 30 m long PM fiber and amplified by means of an tapered amplifier.

ultra stable light is frequency doubled via a commercial SHG¹¹ in bow-tie configuration using a KNbO_3 crystal. This system generates ~ 120 mW at 458 nm which is again fiber guided to the science chamber, where it is used for spectroscopy. Both, the fiber between the labs and the following to the science chamber are stabilized based on a heterodyne detection [22].

2.3 Magnetic Field Induced Spectroscopy

Optical dipole excitation of the strictly forbidden clock transition in bosons can be enabled by mixing the states 3P_1 and 3P_0 via an applied homogeneous magnetic field inducing a Rabi frequency Ω_B .

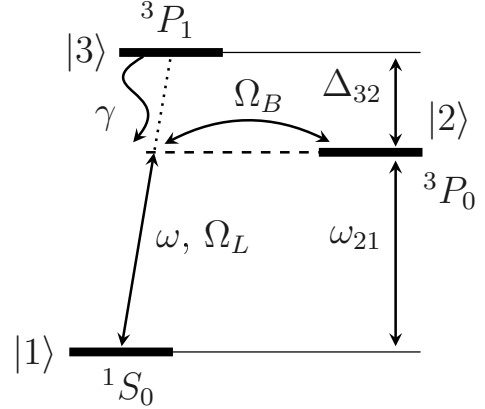
The coupling between both clock states leads to a partially allowed state $|2'\rangle$

$$|2'\rangle = |2\rangle + \frac{\Omega_B}{\Delta_{32}} |3\rangle, \quad (2.4)$$

with Ω_B being the magnetic coupling matrix element and Δ_{32} the splitting between $|2\rangle$ and $|3\rangle$. Applying a probe beam with $\omega \approx \omega_{21}$ allows to observe the transition

¹¹SHG pro, Toptica

Figure 2.9: Scheme of the magnetic field induced spectroscopy of the $^1\text{S}_0 \rightarrow ^3\text{P}_0$ clock transition. A magnetic field B induces a coupling between states $|2\rangle$ ($^3\text{P}_0$) and $|3\rangle$ ($^3\text{P}_1$) which enables a transition between $^1\text{S}_0$ and $^3\text{P}_0$. Source: [18].



$|1\rangle \rightarrow |2\rangle$ with a Rabi frequency Ω_{12} of

$$\Omega_{12} = \frac{\Omega_L \Omega_B}{\Delta_{32}^2} = \alpha \sqrt{I} |\mathbf{B}| \cos \theta. \quad (2.5)$$

All the constants of both relations are combined via α , I is the intensity of the probe beam and $|\mathbf{B}|$ the magnetic field. Taking $\gamma(^1\text{S}_0 \rightarrow ^3\text{P}_1) = 36 \text{ Hz}$ into account, one can calculate α to be $\alpha = 69.0 \text{ Hz/T} \sqrt{\text{mW/cm}^2}$.

The finite lifetime induced by the magnetic field results from atoms transferred to state $|3\rangle$ and decays with the decay rate γ

$$\gamma_{12} \approx \gamma \frac{\frac{\Omega_L^2}{4} + \Omega_B^2}{\Delta_{32}^2}. \quad (2.6)$$

In addition, the intensity of the probe laser leads to a saturation broadening

$$\gamma_s = \gamma_{12} \sqrt{1 + I/I_s}, \quad (2.7)$$

described by the saturation intensity I_s . For our experimental values this effect is negligible with respect to the tunneling broadening [22].

Compared to the fermionic isotopes with a natural transition linewidth in the order of mHz, we expect in magnesium an induced natural linewidth in the μHz regime with an applied magnetic field of a few Gauss and probe intensities of a few watts per square centimeter.

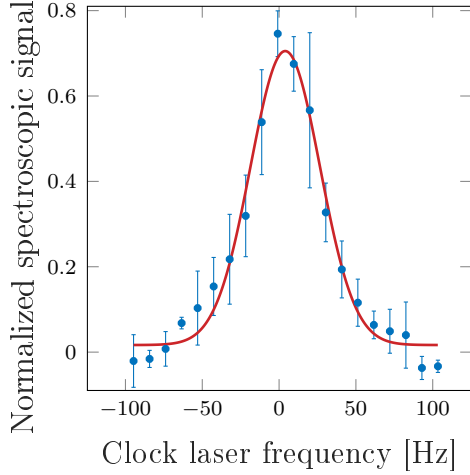


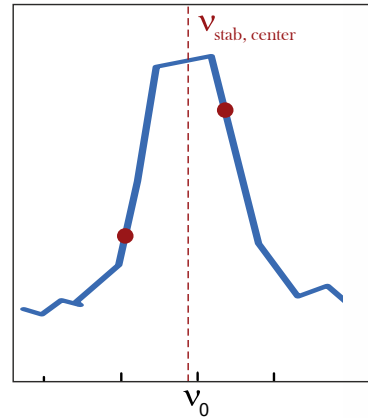
Figure 2.10: First observed clock transition of magnesium with a linewidth of 51(3) Hz and a line quality factor of $1,3 \times 10^{-13}$. The plotted data is averaged across four data sets at trap depth of $36.7 E_R$.

2.4 Highest Line Q Value for the Magnesium Clock Transition

After implementing partially new and partially cleaned viewports in the path of the optical lattice, a circulating lattice power of 8 W was realized for the first time with this setup. In a first step, further measurements of the magic wavelength have been performed which are discussed in chapter 3. Due to the reduced tunneling rate and additionally operation of the lattice closer to the magic wavelength, smaller transition linewidths have been realized, which paved the way for the reduction of the clock laser intensity and the magnetic field. The dependence of the transition linewidth on both was studied by K. Zipfel and is described in his thesis [22]. A further improvement implemented in the experiment are the already described new homogeneous coils.

All in all, the enhanced trap depth, an optical lattice only a few MHz detuned from the magic wavelength, reduced clock laser intensity and magnetic field and also an optimized homogeneous magnetic field lead to a spectroscopy signal with a clock laser pulse of 650 ms of only 51(3) Hz, which is shown in figure 2.10. Compared to the previous measurements with a linewidth in the tens of kHz, the transition linewidth could be reduced by more than two orders of magnitude leading to the highest line quality factor of $Q = \nu/\Delta\nu \approx 1,3 \times 10^{13}$ achieved with magnesium atoms so far.

Figure 2.11:
 The stabilization points at $\nu = \nu_0 \pm \delta$ of the clock laser to the atomic transition in the case where the clock laser is slightly off resonance. This behaviour is indicated by different signal amplitude. The clock laser frequency is corrected after each stabilization sequence.



2.5 Clock Operation

In order to quantify the impact of various effects on the frequency measurement, we lock the frequency of the spectroscopy laser to the atomic transition and measure the frequency shift of the resonance in dependence of the corresponding parameter values. The lock on the resonance is realized by tuning the laser resonance on both edges of the probe frequency curve. The detected number of atoms at both slopes can be used in order to calculate the center transition frequency and based on this to generate a correction to steer the laser, allowing for a compensation of a laser drift. In respect to a scan across the atomic transition this technique requires only two experimental cycles for the determination of the transition frequency leading to an improvement of the stability.

Unfortunately, the lock of the laser on the atomic transition was not working reliably in the case of large cavity drift rates, leading to increased uncertainties of the measurements. Therefore a drift pre-compensation was realized via a beat measurement to an optical frequency comb being referenced to a maser.

Systematic Evaluation of the $^1S_0 \rightarrow ^3P_0$ Transition Spectroscopy in ^{24}Mg

This chapter discusses effects contributing to the uncertainty budget of the frequency measurement and the methods employed for quantifying their impact. Polarizability related effects like the AC Stark shifts induced by applied laser light or the blackbody radiation as well as the second order Zeeman shift, Doppler shifts and also the collisional and gravitational red shift will be discussed.

The analysis on the magic wavelength and the frequency shift due to the Zeeman effect is based on a work by A. Kulosa, who performed experiments in a shallower magic wavelength lattice and therefore observed a larger linewidth due to stronger tunneling [21]. These effects have been studied in this thesis with a higher resolution due to a higher lattice trap depth and hence reduced tunneling. The resulting narrower transition linewidth paved the way to a reduction of the uncertainty of these effects to the low 10^{-15} regime and also to the first direct observation of the probe AC Stark shift.

Nevertheless, the two main contributions to the resulting uncertainty budget are still the tunneling enlarged line width of the transition and at a similar level, the AC Stark effect induced by the lattice light in combination with the associated uncertainty of this frequency of the order of 5.4×10^{-15} . Table 3.10 summarizes the role of these effects for the frequency evaluation of the $^1S_0 \rightarrow ^3P_0$ transition in magnesium.

3.1 The Influence of the Polarizability

The shift of electronic energies due to an external electric field \mathcal{E} is known as the Stark effect and is given by

$$\delta E_i = -\frac{1}{2}\alpha_i \langle \mathcal{E}^2 \rangle - \frac{1}{24}\gamma_i \langle \mathcal{E}^4 \rangle - \dots \quad (3.1)$$

where α_i and γ_i are the polarizability and hyperpolarizability of the state $|i\rangle$ [8]. The interaction energy between the atom and the external field is in general small with respect to the Coulomb interaction of the electron with the nucleus. Therefore, the Stark effect is calculated by employing the perturbation theory [8]:

$$\delta E_i(\omega) = \frac{1}{2\hbar} \sum_{k \neq i} \frac{\omega_{ik} |\langle i | e \vec{r} \vec{\mathcal{E}} | k \rangle|^2}{\omega_{ik}^2 - \omega^2}, \quad (3.2)$$

where the coupling between the states $|i\rangle$ and $|k\rangle$ is given by the angular frequency of the external electrical field ω_{ik} and the dipole momentum $e \cdot \vec{r}$ with e being the elementary charge and \vec{r} the position operator.

The electric field might have a DC as well as AC components. Therefore a case analysis needs to be done for different field frequencies in respect to the transition frequency and the linewidth [39]:

Case I: Quasistatic field. If the frequency of the external electric field is much smaller with respect to the natural transition linewidth, the atoms will follow the field adiabatically. Hence, the effect can be treated as static.

Case II: Slowly oscillating field. In the case where the atoms are exposed to a slowly varying electric field with a frequency larger than the natural linewidth, but much less than the transition frequency, the atoms can no longer follow the variation of the perturbation. In this case the energy of the electronic states will be shifted according to 3.1.

Case III: Rapidly oscillating nonresonant field. The frequency dependence of the polarizability $\alpha_i = \alpha_i(\omega)$ and the hyperpolarizability $\gamma_i = \gamma_i(\omega)$ needs to be taken into account for frequencies of the applied electric field being much larger than the natural linewidth and in the order of the transition frequency.

Case IV: Resonant field. Equation 3.2 shows a singularity in the case of an applied resonant electric field. The interaction between a two-level system and a resonant electric field can be treated with the rotating-wave approximation, leading to the Rabi frequency.

Equating the coefficients of equation 3.1 and 3.2 one can find the scalar polarizability to be

$$\alpha_{s,i}(\omega) \approx \frac{2}{\hbar} \sum_k \frac{\omega_{ik} d_{ik}^2}{\omega_{ik}^2 - \omega^2}. \quad (3.3)$$

or in the case of a DC field

$$\alpha_i = \frac{2}{\hbar} \sum_k \frac{d_{ik}^2}{\omega_{ik}}. \quad (3.4)$$

According to equation 3.1 the AC Stark shift is also influenced by the hyperpolarizability γ_i which is related to two-photon-processes. Even if the hyperpolarizability is having a smaller impact on the energy of the electronic state with respect to the polarizability, it has to be considered in applications with high laser intensities and high resolutions [40]. The hyperpolarizability related frequency shift belongs to the higher order frequency shifts, and will be discussed in 3.1.2.

3.1.1 Polarizability Effects I: The Magic Wavelength

The frequency dependence of the polarizability of the electronic states allows to operate the optical lattice at the so called *magic wavelength*. Here, the differential polarizability of both clock states 1S_0 and 3P_0 vanish in first order $\Delta\alpha(\omega_{\text{mag}}) = 0$. The polarizabilities for both clock states of magnesium-24 have been calculated by M. S. Safronova, shown in figure 3.1. The crossing point between both is indicating the *magic wavelength* to be at 468.45(23) nm [26].

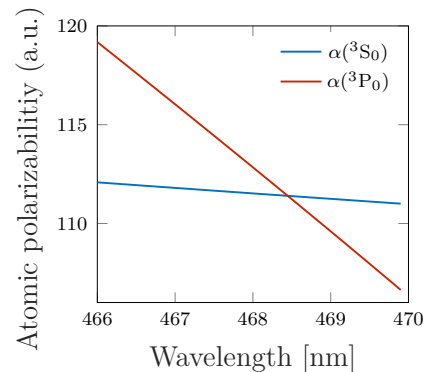


Figure 3.1: Polarizabilities of the clock states of Mg calculated by M. S. Safronova.

Measurement of the Magic Wavelength

The first measurement of the magic wavelength for the $^1S_0 \rightarrow ^3P_0$ transition in magnesium was performed by A. Kulosa [26, 21] in a shallow lattice with a maximum trap depth of $14.5 E_R$ and a resulting linewidth on the order of tens of kHz, which allowed to evaluate the λ_{mag} to be 468.46(21) nm.

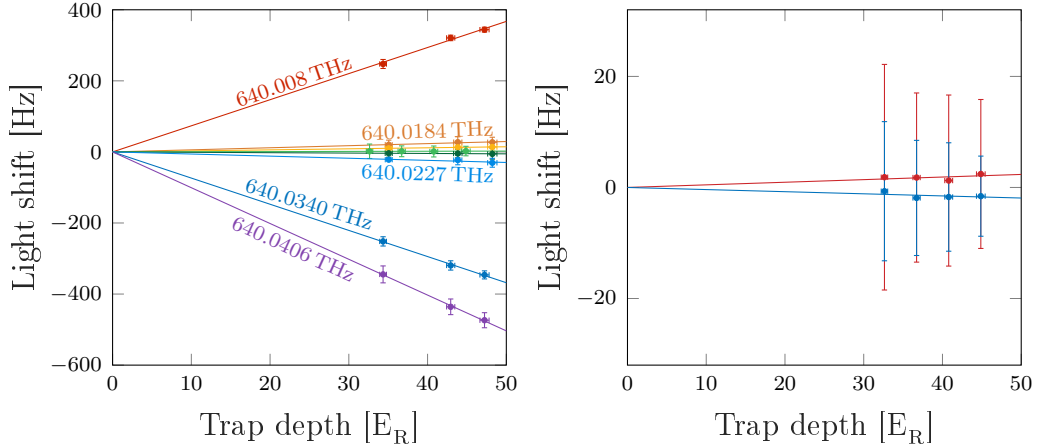


Figure 3.2:
 (Left) Eight measurements of the AC Stark shift with different lattice frequencies and
 (Right) two additional measurements at 640.02054(1) THz close to the magic frequency
 of 640.02071(29) THz. The sample data counts more than 250 data points per trap
 depth and each frequency value averages down to the low 10^{-15} regime.

In the scope of [22] and this work, line width as small as 51(3) Hz have been achieved permitting a more precise determination of systematic shifts. The re-determination of the magic wavelength was performed at eight different wavelengths of the optical lattice with lattice intensities varying between $34 E_R$ and $48 E_R$. The resulting AC Stark shift was determined by locking the laser to the atomic resonance and measuring the frequency shift in respect to the trap depth. For each wavelength, the linear coefficient of the Stark shift was determined, see figure 3.2. With this, the magic wavelength was estimated with improved precision to be 468.4106(2) nm complying with the values of M. Safronova and A. Kulosa. The current precision is still limited by the transition linewidth and hence, the trap depth of the horizontally oriented lattice, and also the lattice light frequency.

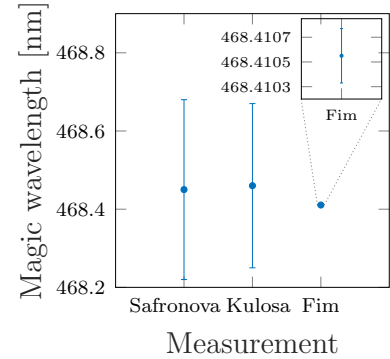


Figure 3.3: Determined values and uncertainties for the magic wavelength.

Day	06/23	06/26	06/27	06/28	06/29	06/30	07/07
$\Delta\nu_{m,\text{lat}}[\text{MHz}]$	32	48	100	96	52	94	32
$\Delta\nu_{\text{lat}}[\text{Hz}]$	0.4	0.6	1.2	1.2	0.6	1.1	0.4

Table 3.1: Detuning of the lattice frequency in MHz with respect to the magic frequency and the resulting frequency shift of the $^1\text{S}_0 \rightarrow ^3\text{P}_0$ clock transition of magnesium.

During the frequency measurement campaign, described in the next chapter (chapter 4), the optical lattice was operated at a circulating power of 2.80(1) W corresponding to a trap depth of 22.9(3) E_{R} . The frequency of the lattice was set between 640.02062(6) THz and 640.02070(6) THz, with the fundamental of the frequency doubled light being characterized against a wavemeter¹ with 30 MHz accuracy, referenced to the 36 Hz narrow intercombination transition. The detuning of the lattice with respect to the magic wavelength has been 32(60) MHz minimum and maximum of 100(60) MHz, depending on the choice of the transfer resonator mode used to stabilize the laser (see section 2.2.8). This resulted in an AC Stark frequency shift of 0.4 Hz in the case of minimum frequency detuning and 1.2 Hz in the case of maximum detuning. Due to the changing frequency during the campaign, the lattice induced light shift was post corrected for every day, respectively and thus does not contribute to the total frequency shift in the error budget. The resulting uncertainty of the lattice AC Stark shift, is composed of the uncertainty of the magic wavelength, the lattice laser frequency and the trap depth and contributes to the total uncertainty.

	ν [Hz]	$\Delta\nu$ [Hz]	ν [10^{-15}]	$\Delta\nu$ [10^{-15}]
Lattice AC Stark	0.0	3.5	0.0	5.4

Table 3.2: Frequency shift and uncertainty contribution to the error budget of the magnesium lattice clock induced by the lattice potential.

¹WSU30, HighFinesse

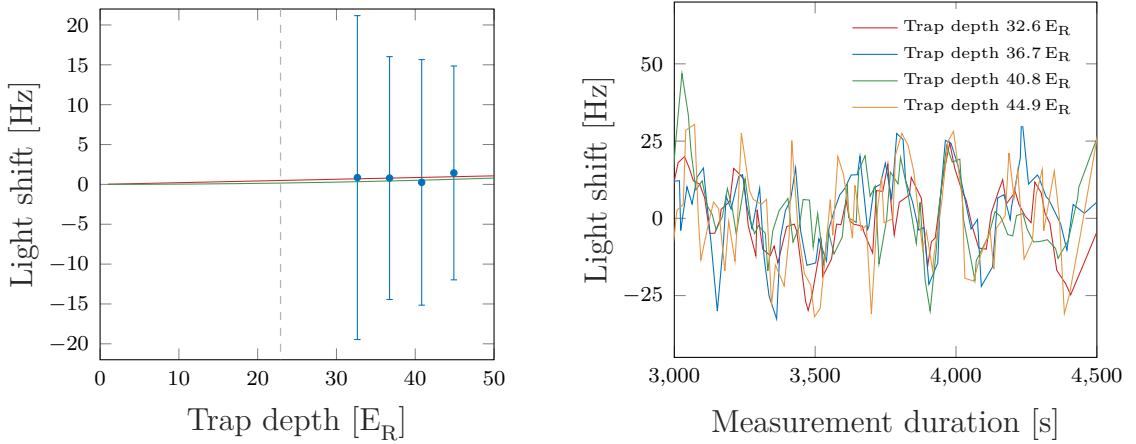


Figure 3.4:

(Left) Measurement of a lattice power dependent frequency shift at high trap depths. Since higher order frequency shifts would lead to a non-linear behaviour a linear (red) and a quadratic (green) fit have been performed. At a trap depth of $22.9 E_R$ (dashed line) the difference of both fits results in a frequency shift of -0.025 Hz. (Right) Associated data after a post correction of the clock laser drift. Non-linear changes of the clock laser frequency drift led to oscillations induced by the lock on the transition which are reflected in enlarged error bars.

3.1.2 Polarizability Effects II: Hyperpolarizability

The hyperpolarizability depends on the square of the lattice trap depth and the lattice frequency. In the case of the strontium clock, for example, the value of the lattice wavelength of 813.428 nm is close to the one of the $5s5p\ ^3P_0 - 3s4f\ ^3F_2$ transition of 818.57 nm. This causes a frequency shift of several kHz at trap depths above $125 E_R$.

In magnesium, states coupling to the clock levels via two-photon processes have a much higher difference in frequency and should therefore have less influence. However, ionization processes² which also contribute to the hyperpolarizability, are larger than for other earth alkalis.

In order to estimate the influence of the hyperpolarizability on the clock transition, we performed measurements at the highest trap depth feasible at this time, shown in figure 3.4 with 4 different lattice parameters from $32.6 E_R$ up to $44.9 E_R$ with 287 data points per trap depth. The difference between two fit functions, a linear and a quadratic one, results in a relative frequency difference of -3.9×10^{-17} for a

²In magnesium the closest transitions to the clock transition which are leading to ionization have transition wavelength of 202 nm and 255 nm.

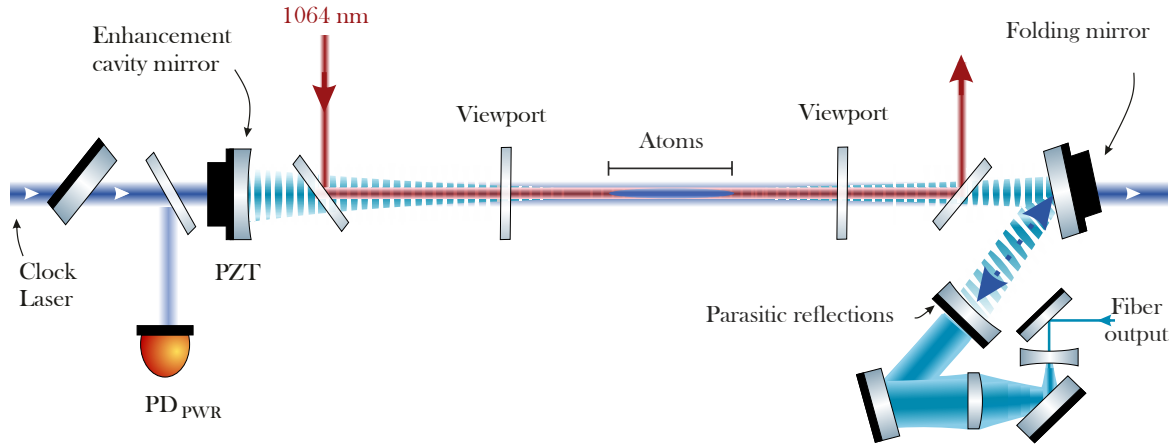


Figure 3.5:

Scheme of the lattice setup as well as the optics to control the light intensity of the probe laser. At first, a fraction of the clock laser light is coupled out in front of the enhancement cavity, which is used for intensity stabilization. The main part of the clock laser is coupled into the resonator via the enhancement mirror on the left but is not completely coupled out by the folding mirror on the right side. Due to technical limitations the required angle on the dichroic mirror could not be maintained which is leading to parasitic reflections and a standing wave arises.

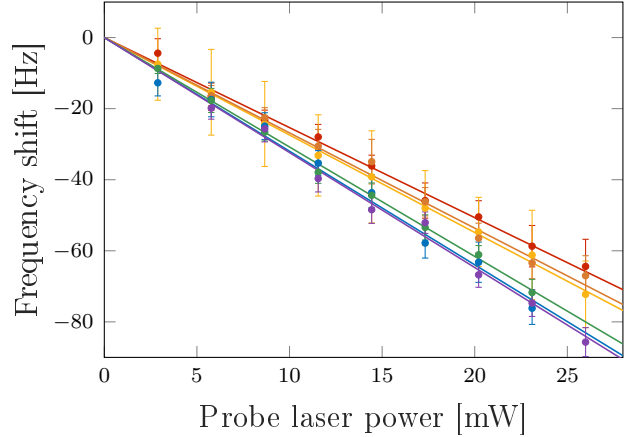
lattice trap depth of $22.9 E_R$ which was applied during the frequency comparison. This effect can therefore be neglected at the accuracy level of our clock. Hyperpolarizability and other higher order effects [41] have to be considered with narrower linewidth and are discussed in the outlook (5.3).

3.1.3 Polarizability Effects III: The Probe AC Stark Shift

During the magnetic field enhanced spectroscopy [18], both the intensity of the probe beam and the magnetic quench field cause frequency shifts. They can be chosen in a way where the total uncertainty gets minimized. In our case, the main uncertainty is given by the probe AC Stark shift due to parasitic reflection of the probe light at the cavity mirrors, shown in figure 3.5, which is leading to a standing wave with fluctuating amplitudes rather than a single travelling wave. Since both standing waves, those of the lattice and those of the clock laser, have different

Figure 3.6:

Measurement of the probe AC Stark shift on the clock transition of magnesium-24 in dependence of the clock laser power measured outside the enhancement cavity. Variations in the intra-cavity probe intensity are leading to an AC Stark slope variations beyond the error bars of each measurement.



periodicities, the overlap of the maxima varies from potential to potential. This finally leads to a reduction of the atomic excitation probability.

Additionally, the fraction of the clock laser used for intensity stabilization is sampled outside the cavity, the intra-cavity intensity depending on the length of the enhancement cavity can not be controlled sufficiently. This behaviour was revealed by a measurement of the AC Stark shift coefficient κ , shown in figure 3.6. There, each linear fit represents one AC Stark shift measurement that was repeated six times in a row, comprising nine different intensities, which were measured outside of the cavity. As the intracavity probe intensity did not directly correspond to the intensity measurement outside the cavity the slope differs for different measurements sets which in turn resulted in a higher total uncertainty for the probe AC Stark shift in the transition frequency of magnesium.

3.1.4 In Situ Measurement of the Probe AC Stark Shift

In order to avoid a dominant uncertainty or even a wrong estimate of the probe AC Stark frequency shift, we decided to track the induced frequency shift during the frequency comparison within an *in situ* measurement. For this purpose, we performed an interleaved measurement of the frequency with a probe beam power of 3 mW and 20 mW ³. During the whole frequency measurement only the error signal generated during the measurement with 3 mW probe laser power was used

³Since, besides the clock sequence a further sequence is applied, the clock's instability grows by $\sqrt{2}$.

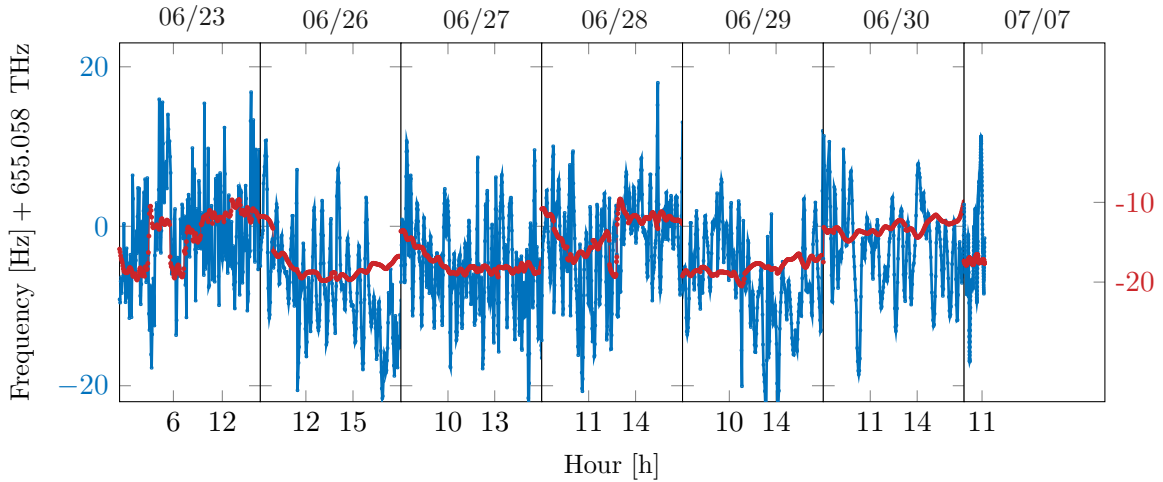


Figure 3.7:

The blue graph is representing the data of the ^{24}Mg frequency measurement compared against the H10 maser at PTB and the change in frequency due to the probe AC Stark inferred from the *in situ* measurement (red). The frequency correction due to probe AC Stark shift is approximately between -10 Hz and -20 Hz . The data was taken at seven days during the frequency comparison against PTB in the period between June the 23rd, 2017 and July the 7th, 2017.

to correct the clock laser frequency and will be referred to as the clock sequence in the following.

For the evaluation of the frequency difference between both sequences, both signals have been fitted using a smoothing spline. Linear fits to any point of both splines results in a time-depended AC Stark frequency shift measurement shown in figure 3.7. The induced probe AC Stark shift is fluctuating between roughly -10 Hz and -20 Hz and was finally post-corrected from the frequency data. The uncertainty of the probe induced AC Stark frequency shift was estimated by the standard deviation of the residual fluctuations to be 2.2 Hz .

	$ \nu [\text{Hz}] $	$ \Delta\nu [\text{Hz}] $	$ \nu_{\text{rel}} [10^{-15}] $	$ \Delta\nu_{\text{rel}} [10^{-15}] $
Probe AC Stark	0.0	2.2	0.0	3.4

Table 3.3: The contribution of the probe AC Stark shift to the uncertainty budget. The Frequency shift of the probe AC Stark shift is post-corrected but still contribut via the uncertainty.

3.1.5 Polarizability Effects IV: Blackbody Radiation Induced Shifts

Next to the lattice and probe light, also the blackbody radiation (BBR) causes a coupling the clock states with other electronic states. The impact off the thermal blackbody radiation on the atoms can also be described by equation (3.1), the polarizability (3.3) and by the power spectral density $\rho(\omega, T)$ described by

$$\rho(\omega, T) = \frac{\hbar}{\pi^2 c^3} \frac{\omega^3}{e^{h\nu/k_B T} - 1} d\omega. \quad (3.5)$$

The average energy field being present in equation (3.1) can be obtained by integrating over a continuous spectrum of frequencies of the spectral distribution $\langle \mathcal{E}^2 \rangle = 1/\epsilon_0 \int_0^\infty d\omega \rho(\omega, T)$. The frequency shift of the clock transition induced by blackbody radiation then becomes

$$\Delta E = -\frac{\hbar}{2\epsilon_0 \pi^2 c^3} \int_0^\infty d\omega \Delta\alpha(\omega) \frac{\omega^3}{e^{h\nu/k_B T} - 1}, \quad (3.6)$$

where $\Delta\alpha(\omega)$ denotes the differential frequency dependent polarizability between the ground and the excited state. The resulting energy change can be split into a static and a dynamic contribution:

$$\Delta E = \Delta E^{(\text{stat})} + \Delta E^{(\text{dyn})}, \quad (3.7)$$

where the static contribution can be assigned to the low frequency part of the blackbody radiation which can be calculated by applying the static polarizability with $\alpha(\omega \rightarrow 0)$

$$\alpha_i = \frac{2}{\hbar} \sum_k \frac{d_{ik}}{\omega_{ik}} \quad (3.8)$$

on the Stark shift

$$\delta E_i^{(\text{stat})} = -\frac{1}{2} \alpha_i \langle \mathcal{E}^2 \rangle. \quad (3.9)$$

The dynamic correction results by subtracting equation (3.9) from the total energy shift (3.6). Consequently, the frequency shift can be given by

$$\Delta\nu_{\text{BBR}} = -\frac{1}{2h} \Delta\alpha \langle \mathcal{E}^2 \rangle_T + \Delta\nu_{\text{dyn}}(T). \quad (3.10)$$

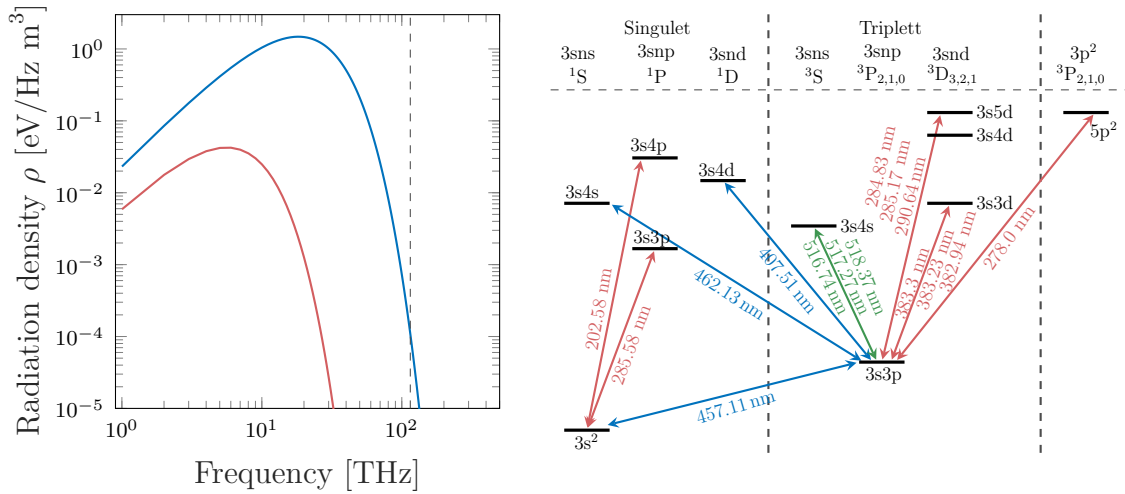


Figure 3.8:

(Left) Spectral density described by Plank's law at 310 K (blue) and 95 K (red). The dashed line indicates the ${}^3P_0 \rightarrow {}^3D_1$ transition of strontium at 115 THz coupling to the BBR. (Right) Level scheme of magnesium with the clock states 1S_0 and 3P_0 and all adjacent states.

The full discussion on the theory can be found in [8, 39, 42].

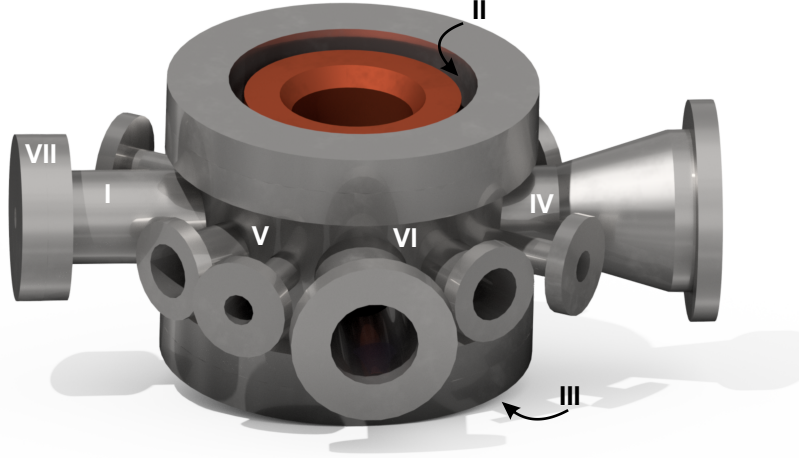
Theoretical Prediction

The most recent calculations of the polarizability for ${}^{24}\text{Mg}$ of [26] and [43] are resulting in $\alpha({}^1S_0) = 71.251(6)$ a.u. and $\alpha({}^3P_0) = 100.922(110)$ a.u.⁴, for the ground and the excited clock state, respectively. The uncertainty was estimated by the difference between a CI+ all order model (*all-order linearized coupled-cluster methods*) and a CI+MBPT (*many body perturbation theories*), which does not include all corrections to the effective Hamiltonian. Both methods differ by an uncertainty of the calculated BBR frequency shift of less than 1% and representing the limit for the uncertainty.

The dynamic contribution of the blackbody frequency shift is based on calculations and lifetime measurements of the 3D_1 state. S. G. Porsev [43] determined the dynamic correction for the 3P_0 to be 0.1 a.u. Comparing the differential dynamic correction and the differential static polarizability of 29.671 a.u. one will find the dynamic polarizability having an amount of less than one percent and hence, can be neglected at our accuracy level.

⁴Atomic units (*a.u.*) having the dimension of volume in units of a_0^3 with a_0 being the Bohr radius. The conversion to SI units is given by the factor $4\pi\epsilon_0 a^3$ [44]

Figure 3.9: Science chamber and the positions of the temperature sensors implemented in [45]. The sensors were placed at the hottest and coldest positions and also the positions in between to get a full expression of the temperature gradient.



The dynamic contribution of the polarizability depends on the frequency spectrum of the radiation, which is shown in figure 3.8 for a temperature of 310 K and 95 K. For higher temperature, the BBR spectrum involves higher frequency components coupling stronger to electronic states. The dashed line at 115 THz corresponds to the $2.6 \mu\text{m } ^3P_0 \rightarrow ^3D_1$ transition in strontium, indicating a contribution to the dynamic correction at room temperature. In magnesium the transitions with the lowest frequency coupling direct to one of the both clock states is the $3s3p ^3P_0 \rightarrow 3s4s ^3S$ transition at $\sim 580 \text{ THz}$ ($\sim 517 \text{ nm}$), shown in figure 3.8 on the right panel. This is the reason why the dynamic polarizability in magnesium is one order of magnitude smaller than in ytterbium (1.86 a.u.) and two orders of magnitude smaller than in strontium (12.37 a.u.).

Uncertainty of the BBR Shift of the Mg Lattice Clock

Besides the uncertainty of the computation of the polarizability and hence of the BBR shift, also the uncertainty in modeling the radiation emitted by the surrounding environment, i.e., its spectral emission and temperature, needs to be considered.

In order to estimate the radiation field at the position of the atoms, one has to consider the radiation of the emitters near by, like the oven or MOT coils together with the geometry of the science chamber. For this purpose D. Holtzwardt performed within his bachelor thesis [45] temperature measurements at seven positions across one side of the science chamber to determine temperature gradients,

shown in figure 3.9 . The temperature values were read out by an analog digital converter⁵ evaluated via LabView and are given in table 3.4. The uncertainty of each temperature value was estimated to be 2.3 °C, respectively.

Based on these temperature values, the mean ambient temperature at the position of the atoms was estimated to be 38.3 °C. The assumed error is derived from the difference between the mean temperature and the maximum/minimum temperature. This results in a frequency shift induced by the blackbody radiation of $-0.297(60)$ Hz.

Sensor	I	II	III	IV	V	VI	VII
Temperature	51.9	28.7	31.9	26.0	28.4	24.7	42.5
Uncertainty	2.3	2.3	2.3	2.3	2.3	2.3	2.3

Table 3.4: PT sensors placed at the science chamber with the positions shown in figure served to estimate the temperature. 2.2

In addition to this frequency shift, the influence of the oven was also taken into account. The thermal radiation of the oven heated up to 440 °C inside the science chamber is transported to the atoms via direct line of sight and multiple reflections from the science chamber walls. In our experiment we therefore use a mechanical shutter, made of Kapton film, which is placed in the main chamber close to the oven aperture in order to screen the atomic sample from this radiation.

During the frequency comparison it was used to partially screen the radiation of the oven propagating in the direction of the atoms. In some groups, the oven contribution was neglected when a shutter was used [46]. Since we can not verify an influence of the oven temperature with the performance of our clock, we made a worst case assumption and included the oven contribution in the estimated uncertainty. The radiation emitted by the oven passes through a 5 mm [28] aperture and its transmitted fraction is assumed to be reflected infinite times by the chamber walls with a reflectivity of 0.81 % for steel. In total the summed up radiation can lead to a frequency shift of -0.061 Hz and will be treated as uncertainty. All in all, both, the ambient temperature and the oven temperature lead to a frequency shift of $-0.3(1)$ Hz.

⁵Meilhaus Ekelectronic, RedLab 1608FS

	ν [Hz]	$\Delta\nu$ [Hz]	ν [10^{-15}]	$\Delta\nu$ [10^{-15}]
BBR ambient	-0.3	0.1	-0.5	0.1
BBR oven	0.0	0.1	0.0	0.1
BBR total	-0.3	0.1	-0.5	0.1

Table 3.5: Frequency shift and uncertainty induced by the blackbody radiation on the magnesium lattice clock.

3.2 2nd Order Zeeman Shift

In the case of bosonic magnesium, both electronic states, the 1S_0 and the 3P_0 , do not provide a permanent magnetic dipole moment. However, other states couple to the clock states and induce a *second order* Zeeman shift which can be written as

$$\Delta_B = \beta \mathbf{B}^2, \quad (3.11)$$

with β being the Zeeman shift coefficient, calculated for magnesium by Taichenachev et al. to -217 MHz/T^2 [18].

Measurement of the Magnetic Coefficient β

In this thesis the measurement of the quadratic Zeeman shift has been performed by generating a magnetic field with coils optimized for a better homogeneity field at the position of the atoms. The current coil stabilization described in the thesis of K. Zipfel [22] was verified by a high precision multi-meter⁶. The magnetic field strength of a given current has been measured using the $^1S_0(m_J = 0) \rightarrow ^3P_1(m_J = \pm 1)$ transition resulting in a sensitivity of $0.6569(2) \text{ G/A}$. A detailed description can be found in the previous section 2.2.2.

The measurement of the second order Zeeman shift has been performed at four different current values. In each case the frequency shift was measured for both directions of the current, i.e. both field directions. The measurement of the Zeeman shift has been repeated five times resulting in a shift coefficient of $\beta = 200.3(7.8) \text{ MHz/T}^2$, which slightly differs from the value of an earlier measurement performed by A. Kulosa [21] to be $-206.6(2.2) \text{ MHz/T}^2$. There the magnetic field was created by the MOT coils, which could be rapidly switched between the

⁶34461, Agilent

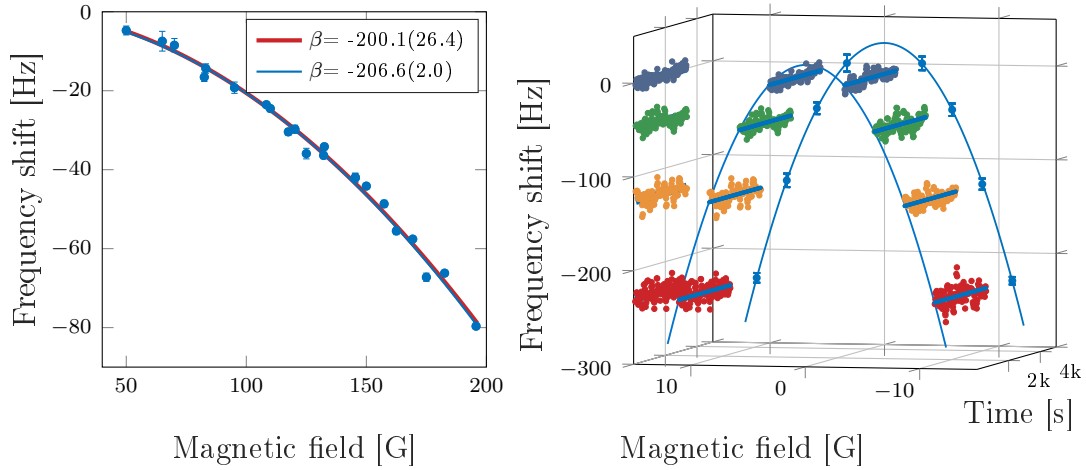


Figure 3.10:

(*Left*) Shown is the data measured by A. Kulosa. The blue graph is a fit to the data without an offset field. In comparison also a fit routine allowing for offsets fields (red fit). (*Right*) Measurement of the second order Zeeman shift coefficient β within this thesis. The blue line represents the mean value, the fit and the error bars. The negative values given for the magnetic field represent the change of the current direction in the coils.

Anti-Helmholtz configuration providing a quadropole field or the Helmholtz configuration for a homogeneous field with 2.49 G/A. The low uncertainty in the previous measurement of β can be assigned to an incomplete fit model, which was not allowing for an additional offset field. In fact, on the data obtained during the measurements of A. Kulosa, and is shown in figure 3.10 (*left panel*), a quadratic fit that allows an offset field, leads to $\beta = -200.1(26.4)$ MHz/T². For the new data, taken within this thesis both fitting routines are giving the same results.

The estimate of the quadratic Zeeman frequency shift is not affected by the discrepancy of the sensitivity coefficient β or the knowledge of its absolute value. During the frequency comparison a constant magnetic field of 6.66(7) G has been applied in order to enhance the strongly forbidden clock transition leading to a frequency shift of $-85.85(1.52)$ Hz. The uncertainty is composed of the uncertainty of the sensitivity parameter β and the uncertainty of the coil current creating the magnetic field.

	ν [Hz]	$\Delta\nu$ [Hz]	ν [10^{-15}]	$\Delta\nu$ [10^{-15}]
Second order Zeeman	-85.6	1.52	-130.7	2.3

Table 3.6: Frequency shift and uncertainty contribution of the magnetic field on the clock transition of magnesium.

3.3 Other Lattice Related Effects

Transitions between bands of different index

Even if spectroscopy in the Lamb-Dicke regime enables a Doppler- and recoil-free interrogation of atoms, a residual first-order Doppler shift can be induced by different effects, such as the excitation of several nearby transitions which is the case when atoms occupying higher bands in the optical lattice being not exactly at the magic frequency. The excitation probability of these atoms depends on the bandwidth and hence on the Rabi-frequency and is therefore reduced compared to the carrier transition. However, this effect can shift the transition frequency, shown in figure 3.11, and act like a residual Doppler shift of first order.

Higher-Order AC Stark Frequency Shift

For higher accuracies of the lattice AC Stark shift, it is no longer sufficient to consider only the first order AC Stark shift but also higher order frequency shifts resulting from the contribution of the electric quadrupole (α^{E2}) and the magnetic dipole (α^{M1}) polarizability and also the polarization dependent hyper-polarizability ($\beta^{1,c}$) for linear and circular polarized light. The total lattice AC Stark shift including higher order effects can be written as

$$\begin{aligned}
\delta\nu_c(I, n, \delta\nu, \xi) \approx & \left(\frac{\partial\Delta\alpha^{E1}}{\partial\nu} \delta\nu - \Delta\alpha^{qm} \right) (2n+1) \sqrt{\frac{E_R}{4\alpha^{E1}}} I^{1/2} \\
& - \left[\frac{\partial\Delta\alpha^{E1}}{\partial\nu} \delta\nu + \Delta\beta(\xi) (2n^2 + 2n + 1) \frac{3E_R}{4\alpha^{E1}} \right] I \\
& + \Delta\beta(\xi) (2n+1) \sqrt{\frac{E_R}{4\alpha^{E1}}} I^{3/2} - \Delta\beta(\xi) I^2,
\end{aligned} \tag{3.12}$$

with n the band index, the slope of the differential polarizability times the detuning from the magic wavelength $\frac{\partial\Delta\alpha^{E1}}{\partial\nu} \delta\nu$, the E2-M1 polarizability $\alpha^{qm} = \alpha^{E2} + \alpha^{M1}$ and the hyperpolarizability effect βI [41].

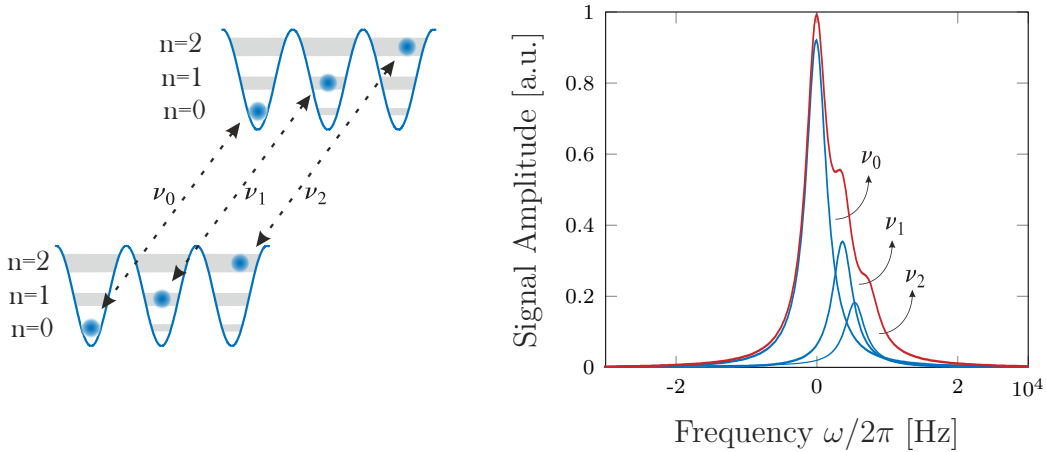


Figure 3.11:

(Left) Carrier transition of several bands in an optical lattice. (Right) Inhomogeneous broadening due to the excitation of multiple frequency shifted vibrational states of the carrier in a "non-magic" optical lattice. Source [47, 21]

Consequently, the influence of atoms located in higher bands will show not only a linear but also a non-linear behaviour. A nonlinear frequency shift of the clock transition was already investigated within the fitting routine shown in figure 3.4 in section 3.1.2. It was found that the amount of a nonlinear contribution results in a negligible frequency shift.

Residual First Order Doppler Shift

In the case of a non-homogeneous filling of the quasi-momentum band, tunneling between lattice sites can also introduce a residual first-order Doppler shift. The frequency shift of the carrier can be in this case in the order of the band structure [48]. However, 100 μ K hot magnesium atoms will equally populate the lowest band quasi momenta according to the Maxwell-Boltzmann distribution, if considering an optical lattice operated with our lattice parameters. This leads to a line-shape broadening instead of a frequency shift, which is described in more detail in [22]. The width of the second band is much broader compared to the first band. However, Line-pulling coming from population of higher bands can be neglected at our uncertainty level.

Relative motion of the lattice with respect to the spectroscopy light

A residual first order Doppler effect can also be caused by a longitudinal jitter between the clock laser and the lattice potential. A common method to reduce this effect evoked by a relative motion between both field along the propagation axis is to reference the clock laser to the lattice. In order to reduce this effect a fiber stabilization of the clock laser being referenced to to the outcoupling mirror of the optical lattice has been implemented and characterized in [22].

3.4 Second Order Doppler Shift

Even if the Doppler shift, discussed on the previous section, is suppressed in first order, higher order corrections of the Taylor expansion need to be taken into account. The second order Doppler effect is given by [49]

$$\Delta\nu_{2^{\text{nd}}\text{Doppler}} = \frac{1}{2}\beta^2\omega_L, \quad (3.13)$$

with the velocity v dependent coefficient $\beta = v/c$ and the laser frequency ω_L . The optical lattice is loaded from the *optical dipole trap* (ODT) with 100 μK hot atoms [26]. The atomic temperature within the lattice was estimated to be roughly 40 μK . However, the atomic velocity of 100 μK hot magnesium atoms is $v_{3\text{D}} = \sqrt{3}v_{1\text{D}} = 32.2 \text{ cm/s}$ leading to a second order Doppler shift of approximately 2.4 mHz. This very low frequency shift can be neglected at accuracies in the 10^{-15} level.

3.5 Collisional Frequency Shift

The frequency shift given by elastic collisions of atoms in the ground state can be described by [50, 51]

$$\delta\nu = \frac{4\pi\hbar^2\rho a_{\text{scat}}}{M}. \quad (3.14)$$

Here, ρ is the atomic density and a_{scat} the scattering length. The latter can be related to the scattering cross section. For bosons the cross section is given by

$$\sigma_l = (2l + 1) \frac{8\pi}{k^2} \sin^2 \delta_l(k), \quad (3.15)$$

with the partial wave number l , the ${}^1\Sigma_g^+$ phase shift for l-wave collisions and the relative wave number $k = \sqrt{2mE}/\hbar$.

At low atomic temperatures only s-wave collisions are likely and p-wave collisions are reduced due to the centrifugal barrier which is $\propto l$. Tiesinga *et al.* calculated the scattering length for collisions between two ground state magnesium atoms to be 1.4(5) nm using experimental data from *ab initio* results from the literature, as well as C_6 , C_8 , C_{10} long-range coefficients [52], with the resulting cross section shown in figure 3.12. A later fourier-transform spectroscopy performed by H. Knöckel et al. results in more accurate data yielding a scattering length of $a = 1.5(3)$ nm and agrees with the former determination by Tiesinga [53, 54].

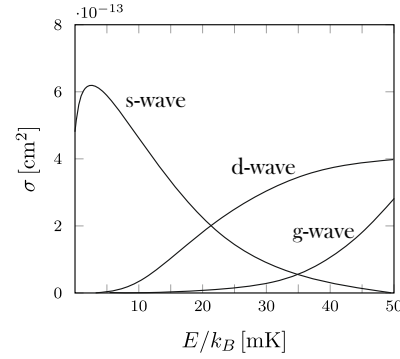


Figure 3.12: Cross section of ground state Mg+Mg collisions. *Source:* [52].

However, the density of the atoms trapped in the lattice cannot yet be measured with a sufficient accuracy in our experiment. Also our knowledge about collisional properties and related effects like a lifetime reduction, density-dependent broadening and a frequency shift are too low to simply calculate this systematic.

Measurement of the Collisional Frequency Shift

In our experiment, the density shift induced by atomic collisions can only be measured in dependence of the lattice loading time, by which atomic densities can be adjusted. In order to measure the atom number, a fluorescence detection of the atoms while captured in the T-MOT has been performed by the means of a photo multiplier (*PMT*). The optically pumped clock states could be successively detected, resulting in a the signal shown in Figure 3.13.

Unfortunately, one pair of the vacuum chamber viewports does not provide an adequate anti-reflex coating for the light of the T-MOT at 383 nm. Therefore, heating processes caused by the MOT coils cause slow polarization variations. Also heating effects at the AOM, which is used to switch the light, and on the fibers that guide the light of the T-MOT are leading to polarization variations. These thermal effects and also a detection noise cause to variations in the loading

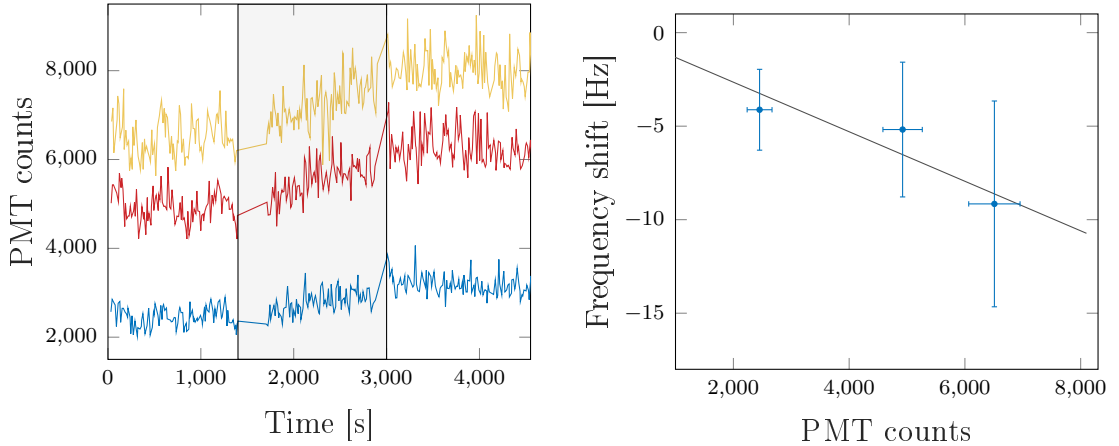


Figure 3.13:

(Left) The plot shows the change of the PMT counts during the measurement of the density shift, induced by polarization effects due to insufficient coatings on the viewports on the vertical T-MOT beam used for detection. The data sample between 30 s up to 1400 s and from 3000 s up to 4500 s have been used for two individual evaluations. (Right) Frequency dependence of the first data sample shown on the left in respect to the number of atoms being detected by the PMT. Here, the PMT counts corresponds to a dipole trap loading time of 300, 1000 and 1500 s.

efficiency, resulting in a drift and shot-to-shot fluctuations.

The density shift measurement was performed alternating by operating the clock with different loading times. The frequency dependence for three different lattice loading times and therefore three different PMT signal is shown in figure 3.13 with a slow change in the number of atoms over time (left panel). Therefore, the total measurement was split into three parts, where only parts without a drift in the number of atoms have been evaluated, separately. In total three data samples with around 100, 115 and 80 data points have been used to calculate a dependence of -6.245×10^{-4} Hz/PMT counts. During the frequency comparison an average PMT signal of 3067 was observed, with a minimum of 1008 and a maximum at 6423. This results in a frequency shift of $-1.9(2.1)$ Hz.

	ν [Hz]	$\Delta\nu$ [Hz]	ν [10^{-15}]	$\Delta\nu$ [10^{-15}]
Cold collisions	-1.9	2.1	-2.9	3.2

Table 3.7: Frequency shift and uncertainty contribution due to collisions at in magnesium lattice clock.

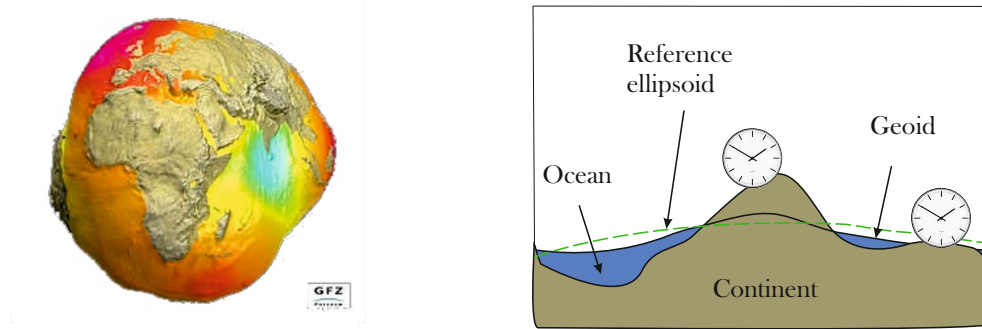


Figure 3.14:

(Left and right) The geoid is a physical surface used as a reference of equal gravitational potential for clocks, approximating the mean sea level. Its characteristic shape is given by the distribution of mass, due to the presence of oceans, mountains and inhomogeneities inside the earth, estimated by satellites. *Source:* Deutsches Geoforschungszentrum (GFZ). Comparing the frequency of two clocks at different heights leads to a direct measurement of the gravitational potential.

3.6 Gravitational Redshift

The last systematic shift considered in this thesis is the gravitational redshift being due to the gravitational potential at the position of the clock. The respective, relative frequency correction that has to be applied is given by

$$\frac{f_0 - f_{\text{clock}}}{f_0} = \frac{\Delta f}{f_0} = \frac{U_{\text{clock}} - U_0}{c^2} \approx 1.09 \times 10^{-16} \text{ m}^{-1}, \quad (3.16)$$

with the speed of light c and the gravitational potential $U_{\text{clock},0} = gh$ at the geoid, being valid only for small differences in altitude [55, 56, 57].

In order to estimate the height of our magnesium lattice clock in respect to the geoid we performed a measurement of the height between a reference point and the science chamber. The reference point, shown in figure 3.15, is mounted to the left of the west entrance next to the main entrance of the Leibniz University Hannover, represented graphically in figure 3.16. The height of the reference point in respect to the geoid estimated in 1992 to be 56.304m above the geoid and was pro-



Figure 3.15: Picture of the reference Point of the LUH in respect to the geoid. *Source:* [58].

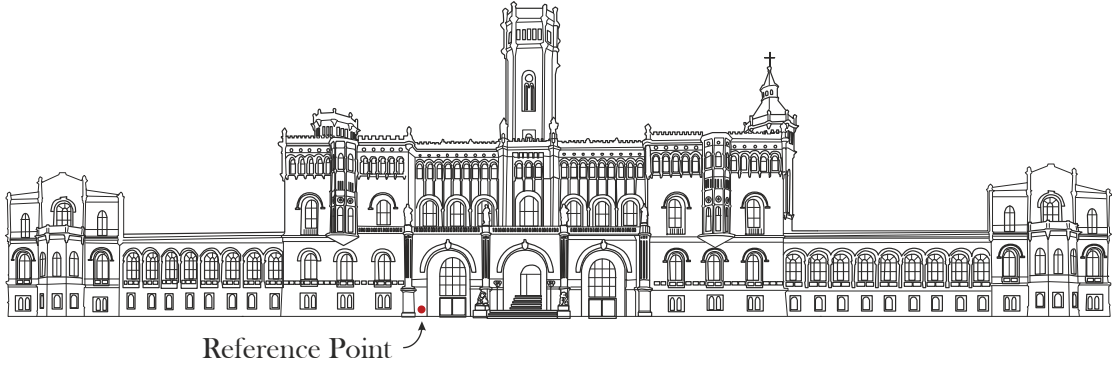


Figure 3.16: Position of the reference point at the LUH [58].

vided by H. Denker from the *Institut für Erdvermessung* (IFE) [58]. The height between the reference point and the magnesium clock is estimated in this thesis to 7.14 m with an uncertainty of 0.5 m leading to a total height of $63.304 \text{ m} \pm 0.5 \text{ m}$. As a consequence, a frequency correction of 4.5(4) Hz has to be applied to the transition frequency of the magnesium lattice clock.

	ν [Hz]	$\Delta\nu$ [Hz]	ν [10^{-15}]	$\Delta\nu$ [10^{-15}]
Grav. red shift	4.5	0.4	6.9	0.5

Table 3.8: Frequency shift and uncertainty contribution given by the gravitational potential for the magnesium lattice clock.

3.7 Summary

This chapter reported the determination of the influence of frequency shifting effects on the $^1S_0 - ^3P_0$ transition frequency as summarized in table 3.10. All measurements are limited by the tunnel-limited resolution of the carrier. The uncertainty of the density shift is also influenced by the T-MOT. There, thermal effects and detection noise are leading to variations in the loading efficiency. The uncertainties of the determination of the density and AC Stark induced shifts would benefit from longer averaging times combined with a larger range of parameter values.

Table 3.9: Error budget of the ^{24}Mg lattice clock

	ν [Hz]	$\Delta\nu$ [Hz]	ν_{rel} [10^{-15}]	$\Delta\nu_{\text{rel}}$ [10^{-15}]
Lattice AC Stark shift	*	3.5	*	5.4
Probe AC Stark	*	2.2	*	3.4
Cold collisions	-1.9	2.1	-2.9	3.2
Second order Zeeman	-85.6	1.5	-130.7	2.3
BBR total	-0.3	0.1	-0.5	0.1
Systematic total	-87.8	4.6	-134.0	7.0
Grav. red shift	4.5	0.4	6.9	0.5
Mg Total	-83.3	4.6	-127.1	7.1

Table 3.10: Summary of the error budget of the magnesium clock at the IQ at the Leibniz University Hannover. All systematics shifts and uncertainties are based on the parameter used during the frequency comparison. A post-correction was been performed at the lattice and probe AC Stark frequency shift which is marked by an asterisk symbol (*).

The blackbody radiation shift is one of the most crucial and fundamental uncertainties in state-of-the-art lattice clocks, which have already reached inaccuracies of 10^{-17} and below, like for example the strontium lattice clocks. The contribution to the blackbody radiation is due to the low sensitivity of magnesium to BBR and accurate calculations performed by M. S. Safronova and S. G. Porsev not limiting our clock at the present uncertainty level.

Measurement of the $^1S_0 \rightarrow ^3P_0$ Transition Frequency in Magnesium

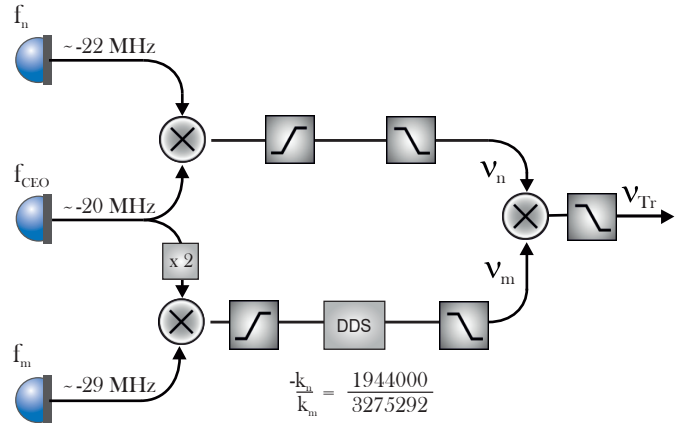
Atomic transition frequencies have to be measured with respect to secondary or primary¹ frequency standards. The later one is defined since 1967 on a caesium-133 transition. The primary frequency standards at the PTB in Braunschweig are based on caesium-133 fountain clocks. A magnesium clock realized with a Ramsey-Bordé interferometer on the intercombination transition ($^1S_0 \rightarrow ^3P_1$) was already compared against a hydrogen maser (H5) being referenced to a caesium fountain clock (CSF1) at the PTB via a 73 km long optical fiber link. The transition frequency of the intercombination transition was determined at this time with an uncertainty of 7×10^{-14} [59].

This chapter presents the first frequency measurement with lattice trapped magnesium atoms and also the first direct frequency measurement of the strictly forbidden $^1S_0 \rightarrow ^3P_0$ transition. The magnesium lattice clock was compared to the CSF2 primary standard and also the ytterbium-171 ion clock. The total measurement time of the magnesium clock was more than 48 hours.

The determined absolute frequency of the magnesium lattice clock against the caesium fountain clock complies within the uncertainties to the sum of the frequency values of the $^1S_0 \rightarrow ^3P_1$ intercombination transition [59, 60] and the $^3P_1 \rightarrow ^3P_0$ transition [61] obtained in former measurements.

¹A primary frequency standard is utilized for the realisation of the SI second with the lowest possible uncertainty.

Figure 4.1:
Setup of the the transfer beat at our experiment [38]. The beat between the CEO and the probe/link laser are mixed with the CEO frequency of the comb. The transfer beat at the IQ was set up by S. Rühmann [38].



4.1 The Comparison of Remote Clocks

4.1.1 The Transfer Beat

The frequency comparison of the clocks was realized by means of *frequency combs* providing a spectrum of equally spaced comb modes separated by the repetition rate² (f_{rep}) and shifted in respect to zero frequency by the CEO frequency³ (f_{CEO}). The frequency of the k th mode can be determined from the product of the mode number k and the repetition rate plus the CEO frequency. In our case, the CEO frequency and the repetition rate are referenced using a maser⁴. Since the repetition rate is up-scaled with the mode number, the noise of the maser would also be up-scaled and hence, would limit the statistical uncertainty. However, the frequency noise of the repetition frequency can be suppressed by a *transfer beat measurement* proposed by H.R. Telle [62] by measuring the frequency ratios instead of the differences.

Both beat-notes f_n and f_m are mixed with the CEO frequency resulting in

$$\nu_n = f_{\text{CEO}} + f_n \quad (4.1)$$

²The repetition rate is associated to the rate between the train of ultrashort pulses. The frequency offset results from the intracavity dispersion leading to a difference between the phase and the group velocity

³The CEO frequency is the Carrier-envelope offset.

⁴VCH-1006, VREMYA-CH, provided by A. Bauch, PTB

and

$$\nu_m = \frac{k_n}{k_m}(f_{\text{CEO}} + f_m), \quad (4.2)$$

whereas one signal (ν_m) is processed with a direct-digital synthesis IC (DDS). With this the transfer beat

$$\nu_{\text{Tr}} = \nu_n - \nu_m = \nu_n - \frac{k_n}{k_m}\nu_m \quad (4.3)$$

inherits only the ratio between the mode numbers and the beat- notes.

The complete setup with all components which were used for the transfer beats at the IQ and the PTB during the frequency comparison is shown in figure 4.2. The absolute frequency of the magnesium clock could thus be determined by following transfer beats:

$$\nu_{\text{Mg,Cs}} = \nu_{\text{Tr}(\text{MgClock,Link})} + \nu_{\text{Tr}(\text{Link,MNPQ})} + \nu_{\text{Tr}(\text{MNPQ,H10})}. \quad (4.4)$$

Whereas, the frequency of the magnesium lattice clock in respect to the ytterbium ion clock could be determined by

$$\nu_{\text{Mg,Yb}} = \nu_{\text{Tr}(\text{MgClock,Link})} + \nu_{\text{Tr}(\text{Link,MNPQ})} + \nu_{\text{Tr}(\text{MNPQ,NIRP})} + \nu_{\text{Tr}(\text{NIRP,Yb})}. \quad (4.5)$$

4.1.2 Remote Frequency Transfer

Frequency comparison between remote clocks can either be performed via an optical fiber link [63] or satellite based signal transfer. A clock comparison on a global scale is today only possible via satellite based techniques, but is limited at instability levels of $\sim 10^{-16}$. Whereas, a distribution of frequency signals via optical fiber links is limited in the distance between the laboratories and requires set-up of individual fiber connections but in turn provides lower instabilities, faster averaging and unprecedented accuracy.

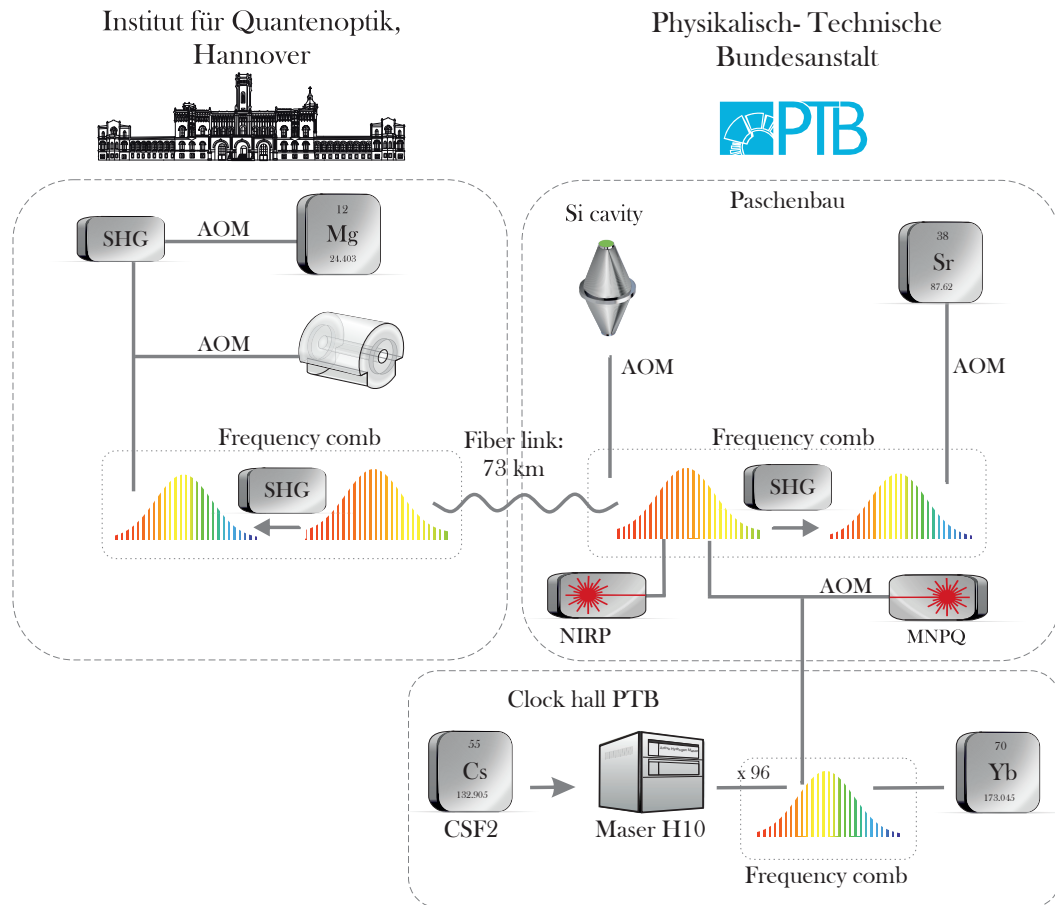


Figure 4.2: Scheme of the link between the magnesium lattice clock at the Institut für Quantenoptik, LUH and the clocks at the PTB in Braunschweig via 73 km long telecommunication fiber link.

Optical Fiber Network

Today Telekom fiber networks allow to distribute ultra stable frequencies thousands of kilometers. Already previous measurement between the IQ and the PTB employed an optical link cover an distance of 73 km [60].

Before the latest comparison, the fiber link operating at 1542nm was rebuild and improved within a collaboration by the group of G. Grosche⁵ from the PTB. It enables an accurate dissemination of frequencies with instabilities below 1×10^{-19} via optical fibers [65] to many long- distance places simultaneously [66, 67], see figure 4.4 left panel.

The fiber path can be described by an asymmetric Michelson interferometer where all phase fluctuation are accumulated along the path. Finally, this phase fluctuations are compensated by AOM1 placed at the front of the link up to the limit set by the propagation delay of the light [68]. In order to distinguish between the light being reflected anywhere along the link and the light being reflected at the end of the link a second

AOM2 is placed at the end of the fiber. This AOM is used to shift the frequency of the link light which is in general a couple of tens of MHz. At any point along the optical fiber, here point B, the counter propagating light fields can be partially extracted, superimposed and detected. The obtained beat signal is divided by two and imprinted on the forward propagating light in order to get a stable signal ν_B . Due to this, the additional phase ϕ_{BC} between point B and the end, point C, is detected and added, whereby the phase at this point is behaving like the phase at the end of the link.

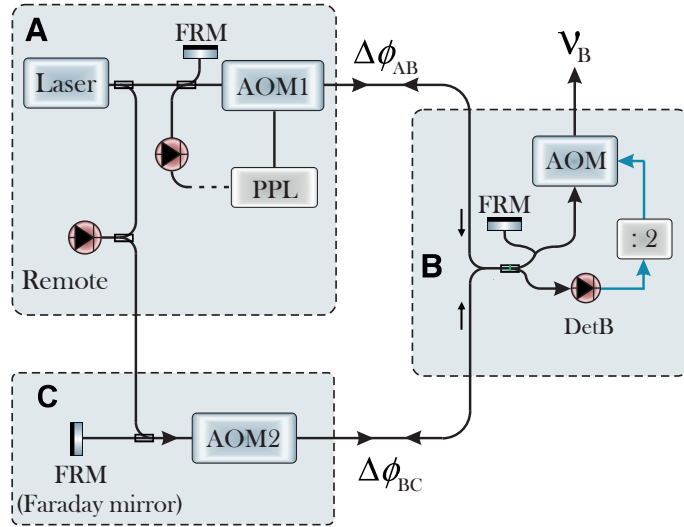
This method was recently implemented and results in an instability and uncertainty below $5 \times 10^{-17}(1s)$ and is two orders of magnitude lower than the uncer-



Figure 4.3: Optical fiber networks in Europe. Frequency links are shown in green, frequency links commissioned in yellow and time links in blue [64].

⁵Optical link: T. Waterholter and A. Kuhl
Data analysis: S. Koke

Figure 4.4:
Setup of the fiber stabilization scheme between the PTB and IQ. Points A and C are placed at the PTB, whereas point B is placed at the IQ, for testing purpose.



tainty of our lattice clock [66]. The accuracy of the link was verified within a loop measurement at the remote detector by the comparison of the direct light of the link laser utilized for stabilization and the light of the link laser which was send there and back.

4.2 Absolute Frequency Measurement of the Magnesium Lattice Clock

The absolute frequency measurement was performed against the PTB hydrogen maser H10 being referenced to the fountain clock CSF2. The clock's systematic uncertainty is determined to 1.7×10^{-16} with an effective frequency instability of $1.5 \times 10^{-13} (\tau/s)^{-1/2}$ [69, 70, 71, 72], shown by the ADEV (*Allan deviation*) in figure 4.5.

During the frequency measurement the CSF2 has been in a non-regular operation mode, which was leading to an increased instability at shorter timescales. However, the instabilities of both, that one of the H10 Maser itself and that of the H10 Maser, corrected by the ^{133}Cs signal, approach each other at averaging times above 10^3 s. The increased systematic uncertainty of the CSF2 clock was estimated by S. Weyers to 1×10^{-15} with an instability of $1.1 \times 10^{-13} (\tau/s)^{-1/2}$ [73].

The measurement against the caesium fountain corrected maser clock yields 83037

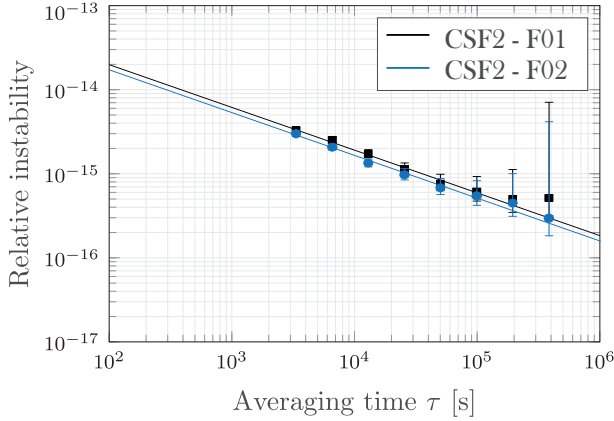


Figure 4.5:

Allan standard deviation of the frequency comparison of the CSF2 at the PTB and the SYRTE-FOx, at the LNE-SYRTE, Observatoire de Paris, *Source:* [71]. The caesium-133 clock reaches an instability of 1×10^{-15} at an averaging times of around 3×10^4 seconds.

data points, which results in an overlap of about 23.07 hours between both clocks. With this, we were able to reach a statistical uncertainty of 7.6×10^{-15} without the *in situ* correction and 3.9×10^{-15} after post-correction (figure 4.6) of the varying probe AC Stark shift resulting from the *in situ* measurement described in section 3.1.4.

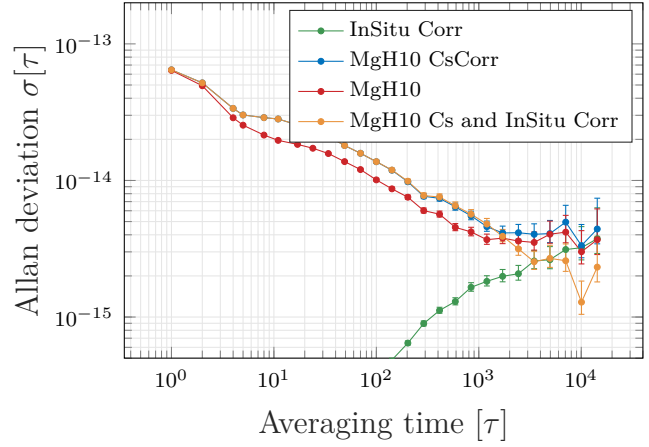
After the application of post-corrections given by the *in situ* measurement, by the lattice AC Stark shift and the remaining systematics we can determine the absolute frequency of the $^1S_0 \rightarrow ^3P_0$ clock transition of the ^{24}Mg lattice clock to 655 058 646 681 864.1(5.3) Hz. All effects contributing to the uncertainty of the knowledge of the transition frequency can be found in table 4.1.

From earlier frequency measurements of the intercombination transition $^1S_0 \rightarrow ^3P_1$ (655 659 923 839 769 (47) Hz) and the transition $^3P_1 \rightarrow ^3P_0$ (601 277 157 860 (20) Hz) in magnesium-24 [7, 61], the clock transition frequency can be determined to be 655 058 646 681 870 (51) Hz. The transition frequency measured with the direct measurement of the clock transition lies within the uncertainty of the previous indirect measurement with an uncertainty improvement of approximately one order of magnitude.

The overall uncertainty of the magnesium-24 frequency determination is limited by the systematic uncertainty of the magnesium clock. As already discussed in the previous chapter, ongoing work on improvements on the lattice power and the enhancement factor of the lattice cavity will lead to higher trap depth. This will allow a reduction of the uncertainties being limited by the current tunnel-limited resolution and thus will improve the systematic uncertainty of magnesium.

Figure 4.6:

Allan deviation of the ^{24}Mg lattice clock versus the CSF2 at the PTB. After removing the correction corresponding to the changing probe AC Stark shift the stability could significantly be improved for higher averaging times. The full discussion on the stability of the ^{24}Mg lattice clock can be found in [22].



Effect	$\Delta\nu_{\text{rel}} [10^{-15}]$
^{24}Mg systematic uncertainty	7.0
CSF2 systematic uncertainty	1.0
Gravitational red shift: ^{24}Mg	0.5
Gravitational red shift: CSF2	0.0
Statistical uncertainty: CSF2 and ^{24}Mg comparison	3.9
Transfer scheme	0.0
Link ⁶	0.0
Total uncertainty	8.1

Table 4.1: Uncertainty budget of the absolute frequency measurement of the ^{24}Mg lattice clock versus the CSF2. The uncertainties being related to the transfer scheme, the Link and also the Gravitational red shift are in the range of 10^{-17} and below and do not contribute significantly to the total uncertainty.

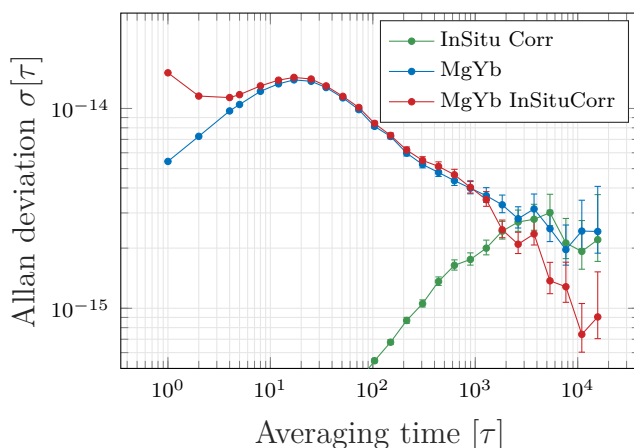


Figure 4.7:

Allan deviation of the frequency comparison between the magnesium-24 lattice clock and the ytterbium-171 ion clock at the PTB. The achieved instability at longer averaging times comply with the stability achieved with caesium clock, indicating magnesium as the limiting factor.

4.3 $^{171}\text{Yb}^+ / ^{24}\text{Mg}$ Optical Frequency Measurement

Optical lattice clocks have already reached uncertainties in the low 10^{-18} regime [15]. Hence, absolute frequency measurements of these clocks are limited by the primary frequency standards. In order to overcome this limitation a unit-less frequency ratio of two optical frequency standards can be determined.

One of the optical frequency standards at the PTB is the Ytterbium-171 ion clock with two transitions being suitable for clock operation. The quadrupole (E2) transition $^2\text{S}_{1/2}(F=0) - ^2\text{D}_{3/2}(F=2)$ with a lifetime of 53 ms with a recommended frequency value of 688 358 979 307.8(36) Hz. The second transition is based on the octupole (E3) transition $^2\text{S}_{1/2}(F=0) - ^2\text{F}_{7/2}(F=3)$ with a transition frequency of 642 121 496 772 645.0(6) Hz [74]. The lifetime of the excited state of the octupole transition is in the order of several years inferring a linewidth in the nHz range. This transition is almost unaffected by spontaneous decay leading to an instability of $5.3 \times 10^{-15} / \sqrt{\tau(s)}$ [75, 76, 77]. The biggest uncertainty contribution of the ytterbium ion clock is given by the residual motion of the ion. Nevertheless, to reduce probe induced frequency shifts this clock was operated during a frequency comparison versus caesium fountain clock with the generalized hyper-Ramsey excitation scheme leading to a total uncertainty of 3.2×10^{-18} [78, 79].

The overlap between the magnesium lattice clock and the ytterbium clock offers 91770 data points with a total overlap time of 25.49 hours. The statistical uncertainty of the comparison is given by the achieved instability of 1.5×10^{-15} after post correction of the *in situ* frequency shift and is limited by the magnesium lattice clock. All the effects contributing to the total uncertainty are shown in table.4.2.

Within this thesis the frequency ratio between the ^{24}Mg lattice clock and the ^{171}Yb ion clock was determined to $^{171}\text{Yb}^+ / ^{24}\text{Mg} = 0.980\,250\,394\,411\,629(7)$, being limited by the magnesium clock. Together with the frequency value of the ^{171}Yb ion clock of $642\,121\,496\,772\,645.0$ Hz with an uncertainty of 6×10^{-16} [74] we could determine the absolute frequency of the ^{24}Mg clock after consideration off all post-corrections to $655\,058\,646\,681\,864.0(4.7)$ Hz.

Effect	$\Delta\nu_{\text{rel}} [10^{-15}]$
^{24}Mg systematic uncertainty	7.0
$^{171}\text{Yb}^+$ systematic uncertainty	<0.1
Gravitational red shift: ^{24}Mg	0.5
Gravitational red shift: $^{171}\text{Yb}^+$	0.0
Statistical uncertainty: $^{171}\text{Yb}^+$ and ^{24}Mg comparison	1.5
Transfer scheme	0.0
Link	0.0
Total uncertainty	7.2

Table 4.2: Uncertainty budget of the frequency measurement of the ^{24}Mg lattice clock against the $^{171}\text{Yb}^+$ clock. Here again, the uncertainties being related to the transfer scheme, the Link and also the Gravitational red shift are in the range of 10^{-17} and below, and do not contribute significantly to the total uncertainty.

4.4 Summary

Within this thesis a first full characterization of a lattice clock based on bosonic magnesium has been demonstrated. Furthermore, the first frequency measurement of lattice trapped magnesium atoms and the first absolute frequency determination of the strictly forbidden $^1S_0 \rightarrow ^3P_0$ clock transition of the bosonic magnesium has been performed. A performance of more than seven hours of up-time per day on average could be demonstrated.

The frequency measurement was performed via a 73 km optical link between the LUH, Hannover and the PTB, Braunschweig which has been set up by the group

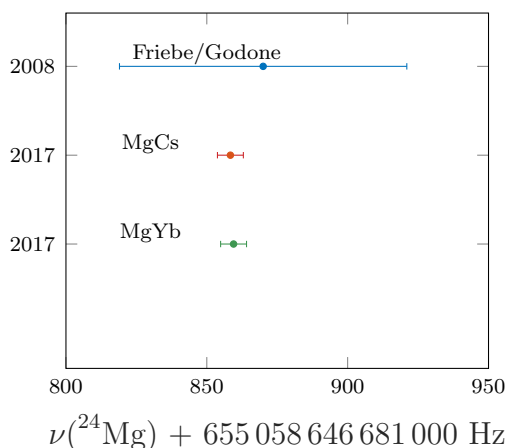


Figure 4.8:

Results of the previous indirect measurements of the clock transition performed by Friebe and Godone and the measurement of the $^1S_0 \rightarrow ^3P_0$ clock transition of ^{24}Mg performed within this thesis. All measurements comply within the uncertainty.

of G. Grosche (T. Waterholter, A. Kuhl and S. Koke). The transfer beat at the Institute of Quantum optics was set up by S. Rühmann.

The absolute frequency of magnesium-24 was determined against the caesium fountain clock (CSF2) operating with a frequency uncertainty of 1×10^{-15} with a total overlap time of 23.07 hours. The total uncertainty of the measurement was limited by the systematic uncertainty of the magnesium clock of 7.0×10^{-15} and led to a total uncertainty of 8.1×10^{-15} . The determined absolute frequency of $655\,058\,646\,681\,864.1(5.3)$ Hz lies within the error bars of the combination of earlier measurements of the $^1S_0 \rightarrow ^3P_1$ and $^3P_1 \rightarrow ^3P_0$ transitions [61, 7, 59]. It's uncertainty has been reduced by approximately one order of magnitude.

Within this frequency measurement campaign also the first measurement of the frequency ratio between the magnesium clock and a ytterbium-171 ion clock has been performed. The determined frequency ratio is $^{171}\text{Yb}^+ / ^{24}\text{Mg} = 0.980\,250\,394\,411\,629(7)$.

All in all, the first optical lattice clock based on magnesium has been demonstrated within this thesis. All leading dominant effects in the uncertainty budget of magnesium are of technical nature. The instability of the magnesium clock of 1.5×10^{-15} was influenced by the additional spectroscopy sequence, within the *in situ* measurement. The system was recently upgraded to primarily address the technical limitations of this work, paving the way for reduced uncertainty in future frequency measurement campaigns.

Outlook

Concluding this thesis, I will discuss the next steps necessary for improving the accuracy of the magnesium lattice clock. For an evaluation of systematic effects with high accuracies still the broad transition linewidth is the main hindrance. The linewidth of 51(3) Hz was an important milestone, but needs to be further reduced to the sub-Hz regime by enhancing the trap depth or lifting the degeneracy of adjacent lattice sites within an accelerated lattice e.g. by gravity.

However, deeper trapping potentials involve in principle larger Stark shifts and also higher order frequency shifts will become relevant at a level of 10^{-16} . Those compensate each other in the case of magnesium and others at a so called operational magic wavelength, to be distinguished from the first order magic wavelength. It will be necessary to study the interplay of these effects in magnesium.

5.1 Reducing the Resolvable Transition Linewidth

Further Reduction of the Linewidth I: Increase the Trap Depth

Broadening due to tunneling in the optical lattices are related to the energy quasimoments. In the case of equally populated quasimomentums, this is given by

$$\Delta E_0 \approx E_R \left(\frac{U_0}{E_R} \right)^{3/4}. \quad (5.1)$$

Since, this expression is related to the recoil energy $E_R = \hbar^2 k^2 / (2m)$, both, a short magic wavelength and also a small mass are liable for a higher energy width and therefore a broader transition linewidth of the resonance curve. Unfortunately, both criteria are met for magnesium. In order to reduce broadening of the transition linewidth by tunneling effects, the trap depth can be further increased with respect to equation 5.1. In the case of a horizontally oriented optical lattice intensities of 488.8 kW/cm^2 are required for a transition linewidth resolution of one Hz.

Such deep lattices can be achieved by a combination of several measures. A Verdi G 12 W pumping a Tekhnoscan Ti:Sa (Tis-SF-07) for generating the lattice light has to be upgraded to 18 W. The Ti:Sa was also operated at the edge of its wavelength range and also required very high maintenance. For a more accurate characterization of the clock, it was necessary to replace it with a system adapted to our requirements, which has been recently done by N. Jha. In a next step also the finesse of the lattice enhancement cavity should be further increased by the implementing new viewports of the vacuum chamber, causing less losses inside the resonator. The targeted intensity which can be achieved with both implementations is about 430 kW/cm^2 and corresponds to a bandwidth of approximately 2 Hz. This is one order of magnitude lower, compared to the resolved linewidth within [22] and this thesis and two orders of magnitude compared to the achieved linewidth during the frequency comparison.

Further Reduction of the Linewidth II: Tilting the Lattice

Tunnel effects can also be reduced by lifting the degeneracy between different lattice sites of a vertically aligned lattice, like depicted in figure 5.1. In this case, lattice intensities of only 214 kW/cm^2 would be required for a resolution of one Hz of the carrier for magnesium. This is about half the resolution of a horizontally aligned lattice. But a change of the orientation of the lattice requires extensive modifications of the setup. However, an experimentally feasible tilting of the lattice by only 5 de-

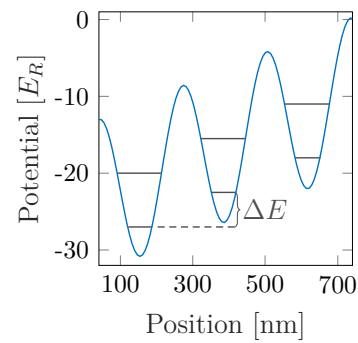


Figure 5.1:

At low bandwidth already a small tilt of the optical lattice can be sufficient in order to lift the degeneracy of neighbouring lattice sites.

greens can lift the degeneracy by 12 Hz. This would slightly relax the stringent lattice power requirement from 488.8 kW/cm^2 to 410 kW/cm^2 .

5.2 Improvement of Systematic Uncertainties

The Probe AC Stark shift

This thesis is a first analysis of possible effects modifying the transition frequency, given in Table 3.10. The experiments revealed, that in our current setup parasitic reflections of the spectroscopy light resulted in a standing wave and hence an inhomogeneous and varying light shift. In order to increase the out-coupling of the probe light, dichroic mirrors being highly reflective for the probe light and highly transmissive for the lattice light should be installed in the near future. The probe light passing the science chamber will at first pass these dichroic mirror, next the folding mirror and finally the out-couple mirror of the enhancement cavity and vice versa, figure 3.5. This additional loss channel, which will be passed twice, should reduced the dependency of the AC Stark frequency shift on the enhancement cavity dramatically. Also a redesign of the enhancement cavity from a folded into a linear design would lead to a reduction of parasitic reflections resulting and a more simple setup.

Relation between the Magnetic Field and the Probe Beam

Once the intensity fluctuations are under control, the uncertainty of the probe AC Stark shift is reduced. The uncertainty of both, the AC Stark shift and the Zeeman shift, then needs to be balanced. Since both shift coefficients are not known, a contribution to a future error budget by the induced frequency shift can only be estimated, respectively. The high second-order Zeeman shift in magnesium can be reduced by lowering the magnetic field and enhancing the probe beam intensity. According to equation 2.5, applying a magnetic field of 4.5 G and a probe intensity of 20 kW/cm^2 , a Rabi frequency of approximately 4.5 Hz can be inferred, which is resulting in a Zeeman frequency shift of 40.6 Hz and an AC Stark frequency shift of 42 Hz. Within a sufficient long average time the uncertainty of both values can finally be averaged down to sub-hertz regime.

With the lattice clock based on bosonic strontium presented in [46], a second order Zeeman shift of only 0.9 Hz and a shift of 0.4 Hz due to the probe laser was

Effect	α [Hz/(T $\sqrt{\text{mW}/\text{cm}^2}$)]	β [MHz/T ²]	κ [mHz/(mW/cm ²)]
Sr	198	-23.3	-18
Mg	98	-217	-0.5

Table 5.1: Values for the coupling coefficient α , the 2nd order Zeeman shift coefficient β and the AC Stark shift coefficient α given in [18].

observed on the basis of a 4 ms long probe pulse and a transition line width of 220 mHz. From the coefficients given in table 5.1, with α being related to the Rabi frequency ($\Omega_{\text{R}}/2\pi = \alpha\sqrt{I}|B|$), β to the second-order Zeeman shift and κ to AC Stark shift, similar frequency shifts can be achieved for magnesium as for strontium, once similar line width and spectroscopy times can be realized.

Blackbody Induced Frequency Shift

The uncertainty the blackbody induced frequency shift is on one hand given by the uncertainty of the polarizability and on the other hand on the knowledge of the temperature. The first again splits in an contribution of the static and dynamic part of the polarizability. The static polarizability of magnesium is given to be 29.671(116) a.u. leading to an uncertainty of the frequency correction of 1.8×10^{-18} . The dynamic polarizability is less than 1% of the static polarizability and can therefore be neglected. However, currently the uncertainty of the blackbody radiation frequency shift is 8.5×10^{-17} . This is caused by the uncertainty about the knowledge of the temperature to which the atoms are exposed to.

The temperature was estimated by means of temperature sensors which had been attached to the vacuum chamber. Since this measurement could be not performed in real time during the frequency comparison, the uncertainty in temperature was estimated by the difference between the mean temperature and the maximum temperature. In order to reduce the uncertainty due to BBR, the temperature measurement should be performed in real time. For this purpose, the temperature sensors must be recalibrated and reattached to the chamber. The electronics and software set up in [45] only needs small modifications.

Once the temperature can be monitored in real time, the uncertainty can be estimated relating to the convention of systematic errors given in [80]. In the case

where only the determination of the upper and lower limit is possible, the assumption can be made that the probability density is constant within the interval and vanishes outside the interval. This means that the spectrum of the temperature radiation can be described with a temperature which lies in the middle between the two limit temperatures $T_i = (T_{\max} + T_{\min})/2$. The associated variance of the temperature is $(\delta T)^2 = (T_{\max} - T_{\min})^2/12$. The uncertainty of the temperature can be decreased with this procedure from 13.6 °C to 7.85 °C. Thus the uncertainty due to the BBR induced frequency shift can be further decreased from 8.5×10^{-17} to 4.8×10^{-17} . A further reduction requires a better cooling of the MOT coils and less heat conduction between the oven and the science chamber or cooling of the science chamber at the position of the oven.

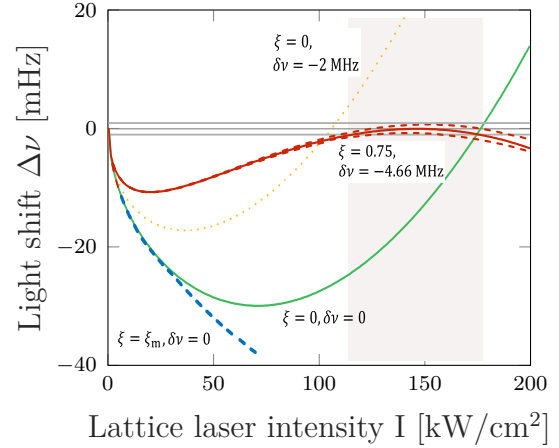
Collisional Frequency Shift

Collisions between magnesium atoms in the lattice haven't been investigated in detail yet. However, three effects can be related to collisions: lifetime reduction, density dependent broadening and also a frequency shift.

The frequency shift induced by collisions have been already discussed in section 3.5. The performed measurement unfortunately had to be split into time slots because of a drift in the PMT signal caused by a change in the atom number detected by the T-MOT. This led to a smaller amount of data and thus to a shorter averaging time for each measured value.

Since the atoms are detected by the triplet MOT a robust operation of this trap needs to be ensured. The intensity of the MOT beams is controlled directly behind the laser system by means of a stabilization scheme. But variations of the polarization caused by thermal effects on the optical fibers, an AOM and viewports with an inadequate coating in the z-direction have been limiting this measurement to 1400 s. However, a replacement of the viewports will involve a disassembly of the optics of the science chamber. Therefore, a first step is to reduce the transition linewidth, which also reduces the uncertainty of this measurement, and a second step is to investigate the polarization changes behind the optical fibers.

Figure 5.2:
Operational magic wavelength for mercury. Besides the lattice detuning the *degree of polarization* can be used in order to reduce the sensitivity to intensity gradients and also in order to reduce the AC Stark light shift for a desired lattice intensity. *Source:* [81].



5.3 Operational Magic Wavelength

Higher order AC Stark shifts like shifts resulting from the electric quadrupole and the magnetic dipole polarizability and also the hyper-polarizability can be used to operate the optical lattice in a regime called the *operational magic wavelength* [81, 82] allowing to control the lattice AC Stark shift within the 10^{-18} regime. The lattice AC Stark shift was already discussed in section 3.3, equation 3.12, but is given here again for clarity¹

$$\begin{aligned} \delta\nu_c(I, n, \delta\nu, \xi) \approx & \left(\frac{\partial\Delta\alpha^{E1}}{\partial\nu} \delta\nu - \Delta\alpha^{qm} \right) (2n+1) \sqrt{\frac{E_R}{4\alpha^{E1}}} I^{1/2} \\ & - \left[\frac{\partial\Delta\alpha^{E1}}{\partial\nu} \delta\nu + \Delta\beta(\xi) (2n^2 + 2n + 1) \frac{3E_R}{4\alpha^{E1}} \right] I \\ & + \Delta\beta(\xi) (2n+1) \sqrt{\frac{E_R}{4\alpha^{E1}}} I^{3/2} - \Delta\beta(\xi) I^2. \end{aligned} \quad (5.2)$$

In ytterbium and mercury the hyperpolarizability effect has an opposite sign for linear and circular polarized light. This can be utilized to tune the light shift close to zero by tuning the *degree of polarization* ($\xi = 1/\sqrt{1 - \Delta\beta^c/\Delta\beta^l}$ with $\Delta\beta^{l,c} = \beta_e^{l,c} - \beta_g^{l,c}$). In addition, all parameters can be selected to minimize the sensitivity of the frequency shift to intensity gradients, as shown in 5.2.

¹Here, n is describing the band index, the slope of the differential polarizability times the detuning from the magic wavelength is given by $\frac{\partial\Delta\alpha^{E1}}{\partial\nu} \delta\nu$, the E2-M1 polarizability is $\alpha^{qm} = \alpha^{E2} + \alpha^{M1}$ and the polarization dependent hyper-polarizability ($\beta^{l,c}$) for linear and circular polarized light.

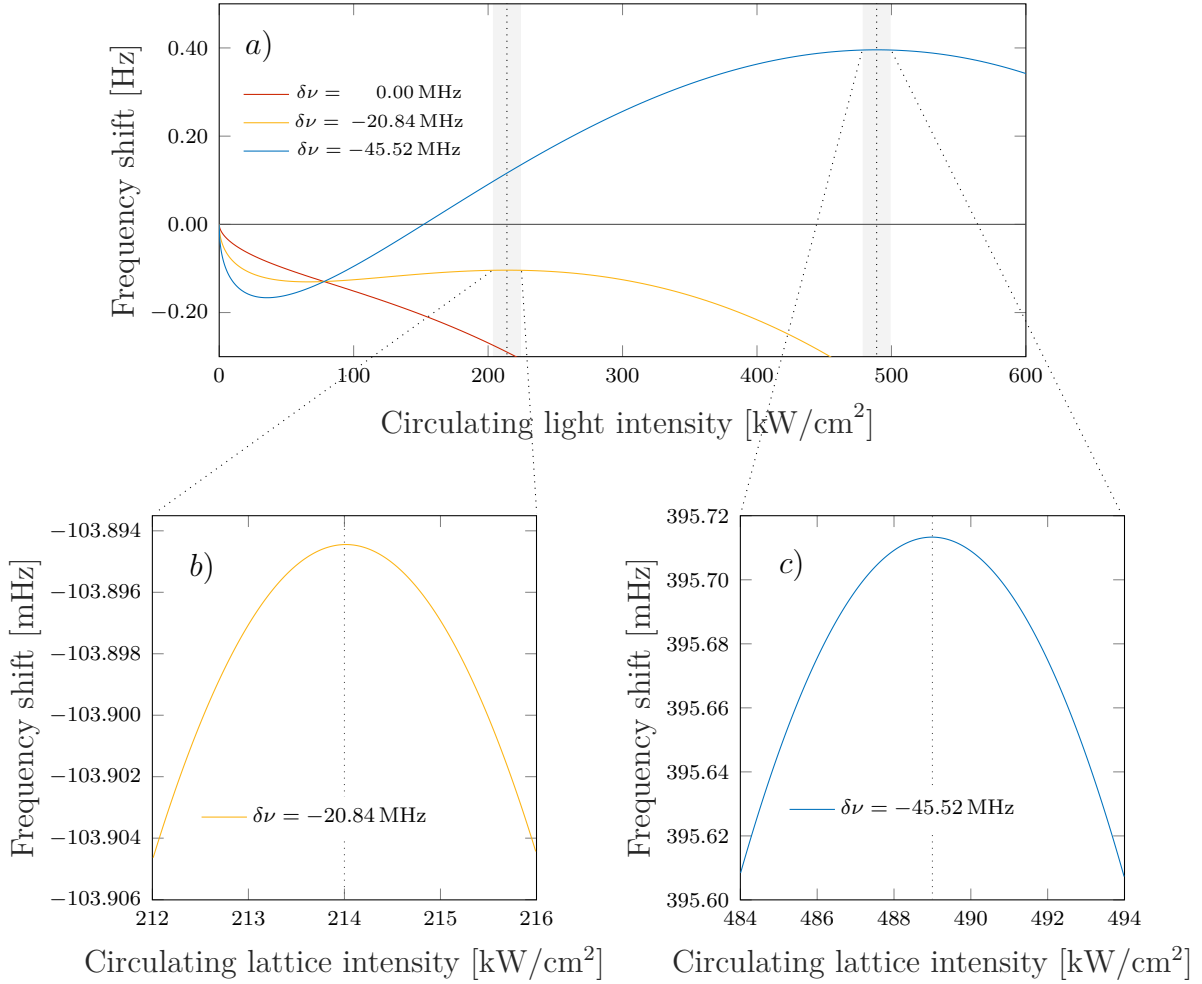


Figure 5.3:

Graph (a): Operational magic wavelength for magnesium atoms with an average band occupation of 2.5 in dependence of the lattice intensity and detuning of the lattice wavelength in respect to the magic wavelength. The dotted lines represent the calculated intensity needed for a bandwidth of one Hz of the lowest band in the case of vertical/modulated lattice (~ 214 kW/cm²) or a horizontal aligned (~ 489 kW/cm²).

Graphs (b) and (c): Zoom into the upper picture to the maxima for the case of a vertically aligned lattice (b) with a detuning in respect to the magic wavelength of ~ 21 MHz and a horizontally aligned lattice (c) with an detuning of ~ 45 MHz. The range of the x-axis is indicating an intensity variation of 1% of the applied intensity.

In strontium and magnesium the hyperpolarizability for both, linear and circular light polarization, has the same sign, therefore ξ can not be used for manipulation of the lattice light shift. The only remaining parameter is the detuning of the lattice frequency with respect to the magic wavelength. Simulations of the operational magic wavelength for magnesium based on the values given in [41] and shown in table 5.2 are shown in figure 5.3. The dotted lines in figure 5.3(a) denote the required intensities for a tunneling limited one Hz resolution of the carrier for a vertical and a horizontal orientated lattice, respectively. For both intensities, the lattice detuning can be chosen in such a way, that the function describing the frequency shift has a maxima.

The plot on the left side (b) of figure 5.3 shows the result of the simulations with parameters optimized for a vertical/accelerated lattice whereas the plot (c) are optimized for a horizontal lattice. As can be seen from these calculations, operating in such a regime, the lattice AC Stark shift is reduced to mHz regime for a 1% change in light intensity. This can be even reduced to approximately 100 μ Hz for a vertical orientated lattice with a detuning of -20.84 MHz, in respect to the magic wavelength.

	Mg
$\alpha^{E1} [\frac{\text{kHz}}{\text{kW/cm}^2}]$	17.5
$\Delta\alpha^{\text{qm}} [\frac{10^{-9}}{\text{kW/cm}^2}]$	5.48
$\Delta\beta^l [\frac{\mu\text{Hz}}{(\text{kW/cm}^2)^2}]$	$111 + 5.88i$
$\Delta\beta^c [\frac{\mu\text{Hz}}{(\text{kW/cm}^2)^2}]$	$1735 + 8.69i$
$\frac{\partial(\Delta\alpha^{E1})}{\partial\nu} [\frac{10^{-9}}{\text{kW/cm}^2}]$	0.420
$E_R [\text{kHz}]$	37.9

Table 5.2: Frequency shift coefficients for ^{24}Mg calculated by V. D. Ovsianikov [41].

5.4 Cooling of Magnesium

Lowering the temperature of the atomic ensemble is crucial once the clock reach a lower uncertainty as many effects altering the resonance frequency depend on this feature. Examples are the energy dispersion due to occupation of different quasi momenta and bands as well as the spatially inhomogeneous higher order dynamic AC Stark effects.

The reduction of the population of atoms of higher-order vibrational states is already implemented by a reduction of the trap depth by variation of the lattice

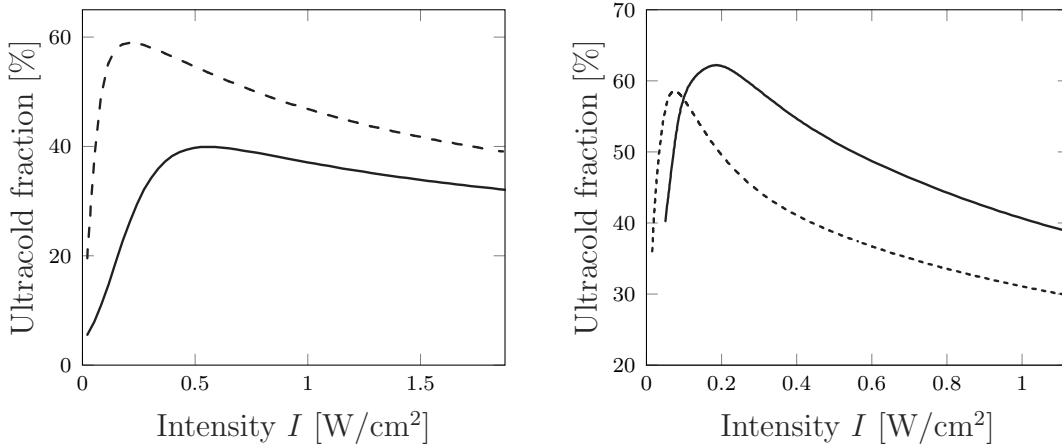


Figure 5.5:

Simulations of the ultracold atomic fraction in sub-Doppler cooling of magnesium. (*Left*) Ultracold fraction in the $\sigma_+\sigma_-$ configuration at detuning of $\delta = -5\Gamma \approx -2\pi \times 130$ MHz. The dashed line represents the semi classical approach, whereas the solid line the full quantum simulation represents. (*Right*) Ultracold fraction in the $\text{lin} \perp \text{lin}$ configuration in the full quantum simulation at detunings of $\delta = -2\Gamma$ (dashed line) and $\delta = -5\Gamma$ (solid line). *Source:* [84]

intensity, described in 2.2.8, which is leading to a mean population of $n = 2.4$ bands with $\sim 10^3$ atoms. However, this method involves a loss of trapped atoms. Instead of releasing the hottest atoms it would be more advantageous to cool the atoms down to the ground band and hence improve the *signal to noise ratio*.

One possible scheme is given by *sideband-resolved laser cooling* [83]. Here the interrogation laser of the clock transition $^1S_0 \rightarrow ^3P_0$ is detuned by the trap frequency ν_z towards the frequency of the first red sideband $h\nu_L = h(\nu_0 - \nu_z)$. The atomic energy is then reduced by an average of ν_z by spontaneous photon emission. Basically, atoms are optically pumped by this scheme to the vibrational ground state of the trap. However, considering the long life time of the meta stable state 3P_0 the limits on the applicability get obvious.

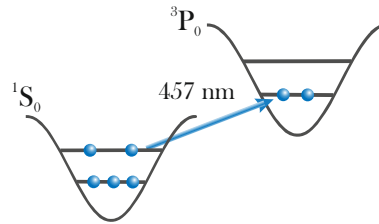


Figure 5.4:

Scheme of sideband cooling. The interrogation laser is applied on the clock transition ν_0 detuned by the trap frequency ν_z . Due to spontaneous emission the atoms emit on average the energy of ν_0 .

Cooling of atoms can even be performed before atoms are transferred into the optical lattice. O. N. Prudnikov and colleagues performed simulations on deep² sub-Doppler laser cooling schemes for magnesium with different laser field configurations [84]. Since, sub-Doppler laser cooling is performed in general at low saturation values, in general, an approximation of the density matrix is used. Prudnikov instead performed his simulations taking all quantum effects into account, the detuning, the optical depth and also the recoil effect.

It turned out that laser cooling in $\sigma_+\sigma_-$ light configuration, like it is used at magneto-optical trapping, seems to be less efficient due to quantum recoil effects in respect to the results achieved with the semiclassical approach. Figure 5.5 shows in the left panel both simulations, where the ultracold fraction drops from 60% to 40% when taking all quantum effects into account. However, the simulations for laser cooling in the $\text{lin} \perp \text{lin}$ configuration seems to be more efficient as shown in figure 5.5 in the right panel. Laser cooling with this light configuration can be applied on magnesium in the absence of the dipole trap, but with the presence of the MOT beams at 383 nm. Parameters being optimal at different detuning are shown in table 5.3.

Applying the cooling scheme in our experiment would imply at first loading $^3\text{P}_2$ atoms in the dipole trap at 1064 nm. After switching off the dipole trap the atoms would be exposed by the cooling laser and finally recaptured in the dipole trap and further transfer into the optical lattice.

δ/Γ	$k_{\text{B}}T[\hbar\Gamma]$	$I[\text{mW}/\text{cm}^2]$
-0.5	0.167	70
-1.0	0.078	80
-2.0	0.070	150
-5.0	0.064	300

Table 5.3: Optimal parameter for sub-Doppler cooling of Mg in $\text{lin} \perp \text{lin}$ configuration.

²A deep potential is in this case achieved by a small detuning

5.5 Priority recommendation of new implementations at the magnesium experiment

Finally, I would like to advise an order for implementing the further steps discussed in this chapter. It is based on best ratio between effort and possible impact on the experimental operation or characterization of the clock respectively. The ones with lowest effort are as follows:

- A good control of the probe AC Stark shift will reduce the instability by a factor of $\sqrt{2}$ by dropping the additional in-situ measurement. As described, only the implementation of a dichroic mirror is necessary, which can be done without any great effort.
- An upgrade of the grating laser system to get higher power and also an upgrade of the cavity optics to improve the fineness which was recently done by N. Jha.
- The knowledge in frequency of the lattice laser is limited by the Wavemeter. A beat- measurement against the optical frequency comb can be realized via an optical fiber, guiding the light to the resonator lab.

Since tilting the lattice or increasing the finesse has little effect on the linewidth, replacing the Ti:Sa is more promising, even though this step is more expensive and labour-intensive. Nevertheless, this step would enhance the lattice power to a regime, which would not only allow to further reduce the transition line width but also would allow to perform a higher order AC Stark shift characterization. Real-time measurement of temperature at the PT sensors is easy to implement, but need not be realized before the BBR-induced frequency shift becomes noticeable.

Once a smaller uncertainty contribution of the probe and lattice AC Stark shift is achieved investigations can be made on the apparatus to make it more robust and reduce atomic fluctuations which are necessary for characterization of a collisional frequency shift.

Appendix A

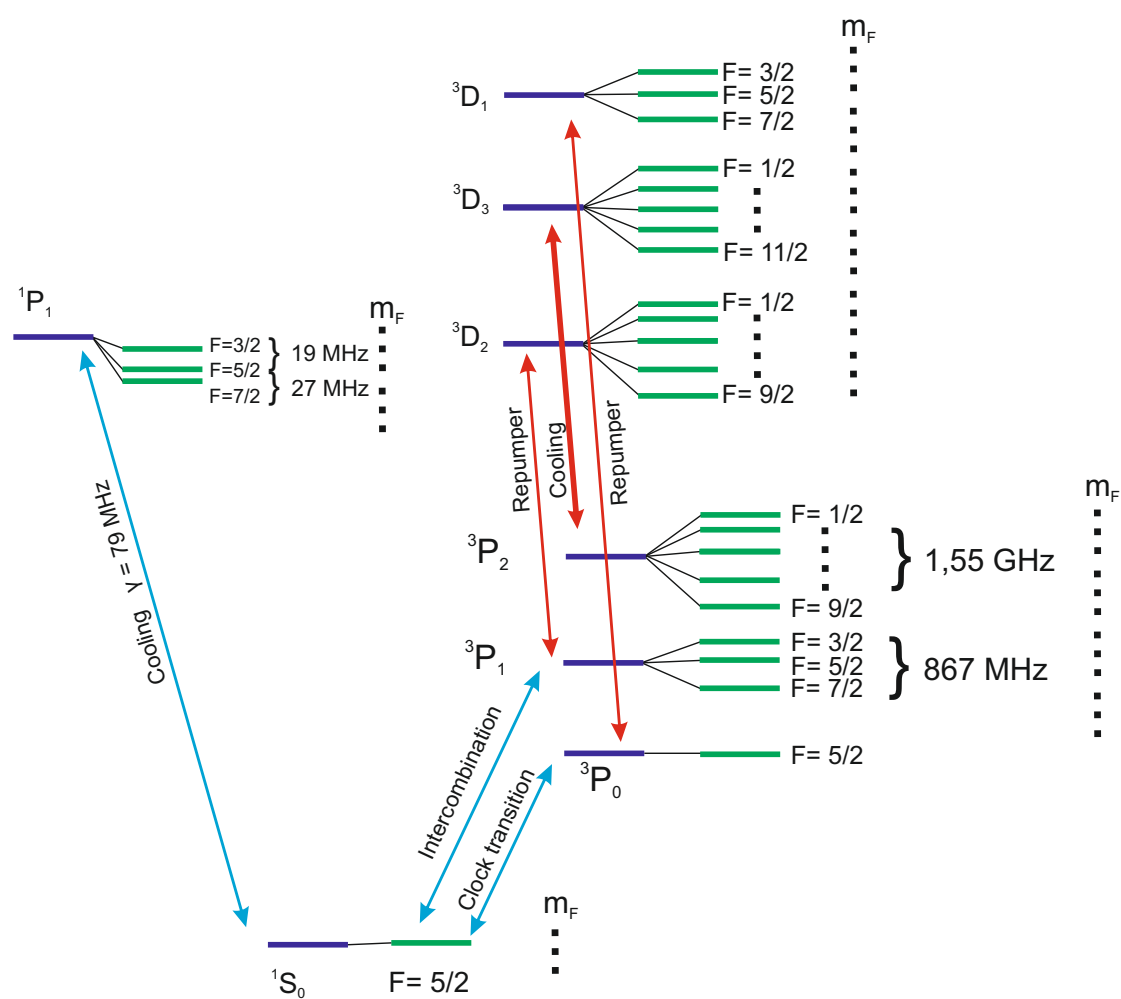


Figure 5.6: Extended ^{25}Mg - Level scheme

Appendix B

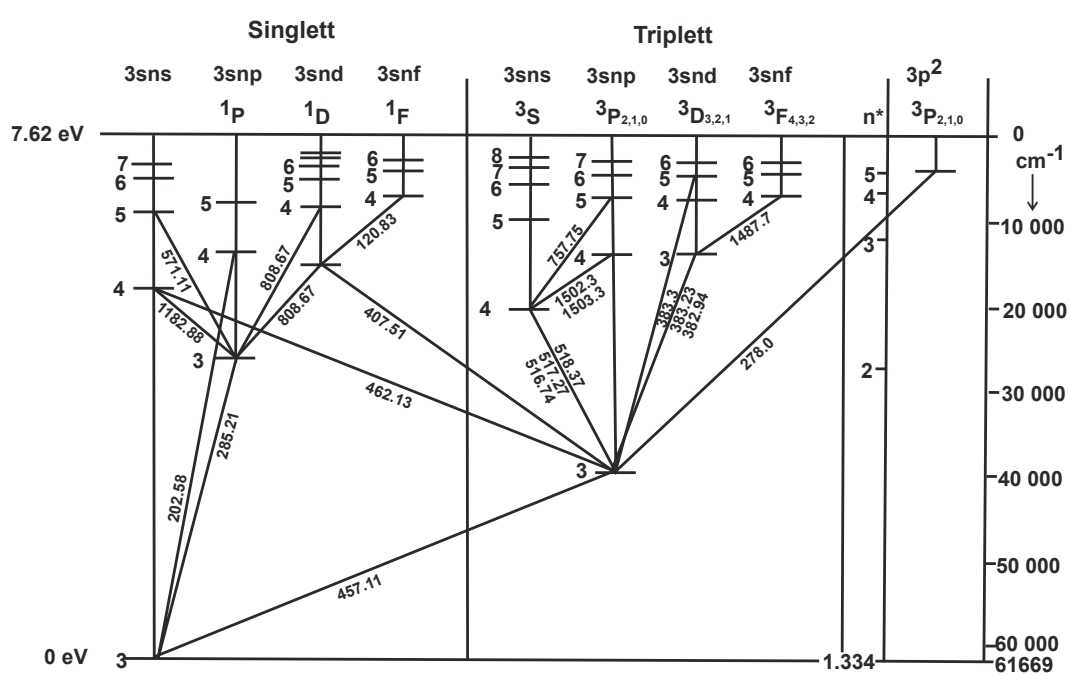


Figure 5.7: Extenden ^{24}Mg - Level scheme

Appendix C

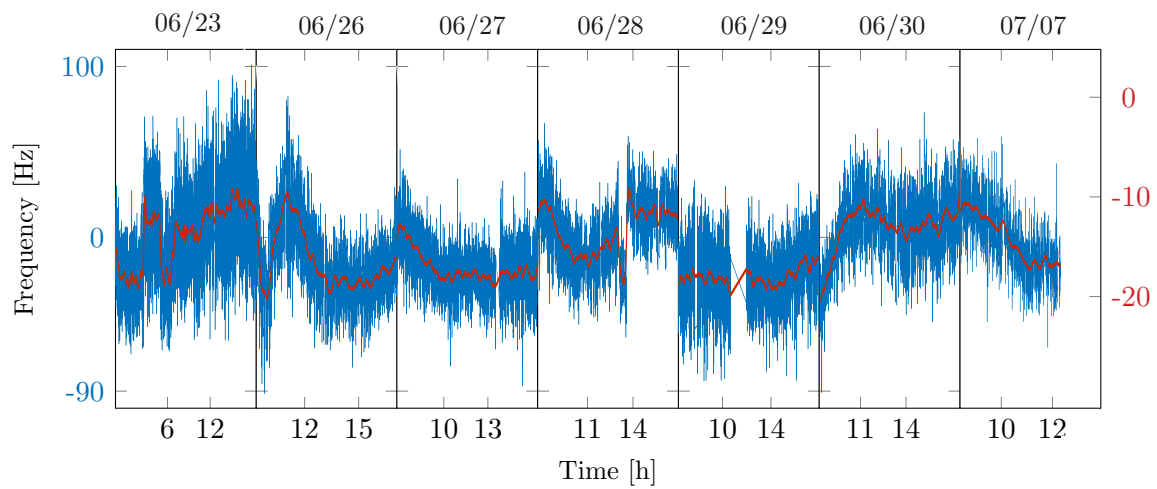


Figure 5.8:

Difference of both data sets sampled at the frequency comparison with probe beam intensities of 3 mW and 20 mW (*blue*) and the fitted smoothing spline (*red*) used for correction of the AC Stark frequency shift.

BIBLIOGRAPHY

- [1] Theodor W. Hänsch.
Nobel Lecture: Passion for precision.
Reviews of Modern Physics, 78(4):1297–1309, nov 2006.
[doi: 10.1103/revmodphys.78.1297](https://doi.org/10.1103/revmodphys.78.1297).
- [2] Bureau International des Poids et Mesures.
The international System of Units (SI), 8th edition, 2006.
- [3] Bureau International des Poids et Mesures.
SI Brochure: The International System of Units (SI).
2006.
- [4] The Earth's gravity field (geoid) as it will be seen by GOCE.
https://de.wikipedia.org/wiki/Internationales_Einheitensystem#SI-Basiseinheiten.
- [5] Bureau International des Poids et Mesures.
On the revision of the International System of Units (SI), Draft Resolution A
26th meeting of the CGPM (13 - 16 November 2018).
- [6] Internationales Einheitensystem.
https://de.wikipedia.org/wiki/Internationales_Einheitensystem.
- [7] Jan Friebe.
Ein optischer Frequenzstandard mit lasergekühltem Magnesiumatomen.
PhD thesis, Gottfried Wilhelm Leibniz Universität Hannover, 2010.
- [8] Fritz Riehle.
Frequency Standards.
Wiley - VCH Verlag GmbH Co. KGaA, 2004.

-
- [9] Andrew D. Ludlow, Martin M. Boyd, Jun Ye, E. Peik, and P. O. Schmidt.
Optical atomic clocks.
Reviews of Modern Physics, 87(2):637–701, jun 2015.
doi: [10.1103/revmodphys.87.637](https://doi.org/10.1103/revmodphys.87.637).
- [10] W. Paul, H. P. Reinhard, and U. von Zahn.
Das elektrische Massenfilter als Massenspektrometer und Isotopentrenner.
Zeitschrift für Physik, 152(2):143–182, apr 1958.
doi: [10.1007/bf01327353](https://doi.org/10.1007/bf01327353).
- [11] Wolfgang Paul.
Electromagnetic traps for charged and neutral particles.
Reviews of Modern Physics, 62(3):531–540, jul 1990.
doi: [10.1103/revmodphys.62.531](https://doi.org/10.1103/revmodphys.62.531).
- [12] R. H. Dicke.
The Effect of Collisions upon the Doppler Width of Spectral Lines.
Physical Review, 89(2):472–473, jan 1953.
doi: [10.1103/physrev.89.472](https://doi.org/10.1103/physrev.89.472).
- [13] M. Takamoto, F. L. Hong, R. Higashi, and H. Katori.
An optical lattice clock.
Nature, 2005:321–324, 435.
doi: [10.1038/nature03541](https://doi.org/10.1038/nature03541).
- [14] W. F. McGrew, X. Zhang, R. J. Fasano, S. A. Schäffer, K. Beloy, D. Nicolodi,
R. C. Brown, N. Hinkley, G. Milani, M. Schioppo, T. H. Yoon, and A. D.
Ludlow.
Atomic clock performance enabling geodesy below the centimetre level.
Nature, 564(7734):87–90, December 2018.
doi: <https://doi.org/10.1038/s41586-018-0738-2>.
- [15] T.L. Nicholson, S.L. Campbell, R.B. Hutson, G.E. Marti, B.J. Bloom, R.L.
McNally, W. Zhang, M.D. Barrett, M.S. Safronova, G.F. Strouse, W.L.
Tew, and J. Ye.
Systematic evaluation of an atomic clock at 2×10^{-18} total uncertainty.
Nature Communications, 6(1), apr 2015.
doi: [10.1038/ncomms7896](https://doi.org/10.1038/ncomms7896).
- [16] M. S. Safronova, S. G. Porsev, U. I. Safronova, M. G. Kozlov, and Charles W.
Clark.

- Blackbody-radiation shift in the Sr optical atomic clock.
Physical Review A, 87(1), jan 2013.
doi: [10.1103/physreva.87.012509](https://doi.org/10.1103/physreva.87.012509).
- [17] K. Beloy, J. A. Sherman, N. D. Lemke, N. Hinkley, C. W. Oates, and A. D. Ludlow.
Determination of the $5d6s^3D_1$ state lifetime and blackbody-radiation clock shift in Yb.
Physical Review A, 86(5), nov 2012.
doi: [10.1103/physreva.86.051404](https://doi.org/10.1103/physreva.86.051404).
- [18] A. Taichenachev, V. Yudin, C. Oates, C. Hoyt, Z. Barber, and L. Hollberg.
Magnetic Field-Induced Spectroscopy of Forbidden Optical Transitions with Application to Lattice-Based Optical Atomic Clocks.
Physical Review Letters, 96(8), mar 2006.
doi: [10.1103/physrevlett.96.083001](https://doi.org/10.1103/physrevlett.96.083001).
- [19] Temmo Wübenna.
Spektroskopie des $^1S_0 \rightarrow ^3P_0$ Uhrenübergangs von ^{24}Mg in einem optischen Gitter bei der vorhergesagten magischen Wellenlänge.
PhD thesis, 2012.
- [20] K. Zipfel.
Aufbau und Charakterisierung eines Überhöhungsresonators für die optische Speicherung von Magnesium Atomen bei magischer Wellenlänge.
Master's thesis, Institut für Quantenoptik, 2011.
- [21] André Kulosa.
Lamb-Dicke Spectroscopy of the $^1S_0 \rightarrow ^3P_0$ Transition in ^{24}Mg and Precise Determination of the Magic Wavelength.
PhD thesis, Gottfried Wilhelm Leibniz Universität Hannover, 09 2015.
- [22] Klaus Zipfel.
Hochauflösende Spektroskopie und Stabilitätsanalyse eines Magnesium Frequenzstandards.
PhD thesis, Leibniz Universität Hannover, 2019.
- [23] J. S. Coursey, D. J. Schwab, J. J. Tsai, , and R. A. Dragoset.
Atomic Weights and Isotopic Compositions.
NIST Standard Reference Data 144.

-
- [24] P. L. Hansen, K. T. Therkildsen, N. Malossi, B. B. Jensen, E. D. van Ooijen, A. Bruschi, J. H. Müller, J. Hald, and J. W. Thomsen.
Measurement of the $3s3p^3P_1$ lifetime in magnesium using a magneto-optical trap.
Physical Review A, 77(6), jun 2008.
doi: [10.1103/physreva.77.062502](https://doi.org/10.1103/physreva.77.062502).
- [25] Andrei Derevianko.
Feasibility of Cooling and Trapping Metastable Alkaline-Earth Atoms.
Physical Review Letters, 87(2), jun 2001.
doi: [10.1103/physrevlett.87.023002](https://doi.org/10.1103/physrevlett.87.023002).
- [26] A.P. Kulosa, D. Fim, K.H. Zipfel, S. Rühmann, S. Sauer, N. Jha, K. Gibble, W. Ertmer, E.M. Rasel, M.S. Safronova, U.I. Safronova, and S.G. Porsev.
Towards a Mg Lattice Clock: Observation of the $^1S_0 - ^3P_0$ Transition and Determination of the Magic Wavelength.
Physical Review Letters, 115(24), dec 2015.
doi: [10.1103/physrevlett.115.240801](https://doi.org/10.1103/physrevlett.115.240801).
- [27] Tanja Mehlstäubler.
Neuartige Kühlmethode für einen optischen Magnesium-Frequenzstandard.
PhD thesis, Gottfried Wilhelm Leibniz Universität Hannover, 2005.
- [28] Nils Rehbein.
Realisierung neuer Laserkühlverfahren und Spektroskopielaser für einen optischen Magnesium-Frequenzstandard.
PhD thesis, Leibniz Universität Hannover, 2006.
- [29] Karsten Moldenhauer.
Sub-Doppler-Kühlung und magnetische Speicherung von Magnesiumatomen bei Temperaturen unter 1 mK.
PhD thesis, Leibniz Universität Hannover, 2008.
- [30] A. Ashkin and J. P. Gordon.
Stability of radiation-pressure particle traps: an optical Earnshaw theorem.
Optics Letters, 8(10):511, oct 1983.
doi: [10.1364/ol.8.000511](https://doi.org/10.1364/ol.8.000511).
- [31] H.J. Metcalf and P van der Straten.
Laser Cooling and trapping.
1999.

-
- [32] M. Riedmann.
Optisches Speichern von Magnesium.
PhD thesis, Fakultät für Mathematik und Physik der Gottfried Wilhelm Leibniz Universität Hannover, 2010.
- [33] Jan Friebe.
Effiziente Erzeugung von ultraviolettem Licht mit neuartigen Kristallstrukturen.
Diploma thesis, Institut für Quantenoptik, Universität Hannover, 2005.
- [34] Alexander Voskrebenezv.
Aufbau und Test eines Lasersystems zur Kühlung metastabiler Magnesiumatome.
Diploma thesis, Institut für Quantenoptik, Universität Hannover, 2007.
- [35] M. Riedmann, H. Kelkar, T. Wübbena, A. Pape, A. Kulosa, K. Zipfel, D. Fim, S. Rühmann, J. Friebe, W. Ertmer, and E. Rasel.
Beating the density limit by continuously loading a dipole trap from millikelvin-hot magnesium atoms.
Physical Review A, 86(4), oct 2012.
doi: [10.1103/physreva.86.043416](https://doi.org/10.1103/physreva.86.043416).
- [36] J. Heinze.
Frequenzstabilisierung basierend auf einem Transferresonator, 2015.
- [37] A. Pape.
Hochstabiler Lokaloszillator für einen optischen Magnesium-Frequenzstandard.
PhD thesis, 2012.
- [38] Steffen Rühmann.
Frequenzstabilisierung eines hochstabilen Lasersystems bis zum Thermischen-Rausch-Limit und Berechnungen eines Laser-Synergie-Konzeptes.
PhD thesis, 2018.
- [39] John W. Farley and William H. Wing.
Accurate calculation of dynamic Stark shifts and depopulation rates of Rydberg energy levels induced by blackbody radiation. Hydrogen, helium, and alkali-metal atoms.
Physical Review A, 23(5):2397–2424, may 1981.
doi: [10.1103/physreva.23.2397](https://doi.org/10.1103/physreva.23.2397).

-
- [40] Anders Brusch, Rodolphe Le Targat, Xavier Baillard, Mathilde Fouché, and Pierre Lemonde.
Hyperpolarizability Effects in a Sr Optical Lattice Clock.
Physical Review Letters, 96(10), mar 2006.
doi: [10.1103/physrevlett.96.103003](https://doi.org/10.1103/physrevlett.96.103003).
- [41] V D Ovsianikov, S I Marmo, S N Mokhnenko, and V G Palchikov.
Higher-order effects on uncertainties of clocks of Mg atoms in an optical lattice.
Journal of Physics: Conference Series, 793:012020, jan 2017.
doi: [10.1088/1742-6596/793/1/012020](https://doi.org/10.1088/1742-6596/793/1/012020).
- [42] Thomas Middelmann.
Bestimmung des Einflusses thermischer Strahlung auf eine optische Strontium- Gitteruhr.
PhD thesis, Fakultät für Mathematik und Physik der Gottfried Wilhelm Leibniz Universität Hannover, 2013.
- [43] Sergey G. Porsev and Andrei Derevianko.
Multipolar theory of blackbody radiation shift of atomic energy levels and its implications for optical lattice clocks.
Physical Review A, 74(2), aug 2006.
doi: [10.1103/physreva.74.020502](https://doi.org/10.1103/physreva.74.020502).
- [44] Mariana Safronova (private communications).
- [45] D. Holtzwardt.
Untersuchung zur minimierung der thermischen Unsicherheit für einen gitterbasierten Frequenzstandard mit ^{24}Mg , 2015.
- [46] S. Orogliã, M.S. Pramod, S. Schiller, Y Singh, K. Bongs, R. Schwarz, A. Al-Masoudi, S. Herbes, S. Häfner, U. Sterr, and Ch. Lisdat.
A high-performance optical lattice clock based on bosonic atoms.
arXiv:1803.03157v1, 2018.
- [47] L. Yi, S. Mejri, J. J. McFerran, Y. Le Coq, and S. Bize.
Optical Lattice Trapping of ^{199}Hg and Determination of the Magic Wavelength for the Ultraviolet $^1S_0 \leftrightarrow ^3P_0$ Clock Transition.
Phys. Rev. Lett., 106(7):0733005, 2011.
doi: [10.1103/PhysRevLett.106.073005](https://doi.org/10.1103/PhysRevLett.106.073005).

-
- [48] Pierre Lemonde and Peter Wolf.
Optical lattice clock with atoms confined in a shallow trap.
Physical Review A, 72(3), sep 2005.
doi: [10.1103/physreva.72.033409](https://doi.org/10.1103/physreva.72.033409).
- [49] A. D. Ludlow.
The Strontium Optical Lattice Clock: Optical Spectroscopy with Sub-Hertz Accuracy.
PhD thesis, Brigham Young University, , Colorado, 2002.
- [50] Paul J. Leo, Paul S. Julienne, Fred H. Mies, and Carl J. Williams.
Collisional Frequency Shifts in ^{133}Cs Fountain Clocks.
Physical Review Letters, 86(17):3743–3746, apr 2001.
doi: [10.1103/physrevlett.86.3743](https://doi.org/10.1103/physrevlett.86.3743).
- [51] Martin W. Zwierlein, Zoran Hadzibabic, Subhadeep Gupta, and Wolfgang Ketterle.
Spectroscopic Insensitivity to Cold Collisions in a Two-State Mixture of Fermions.
Physical Review Letters, 91(25), dec 2003.
doi: [10.1103/physrevlett.91.250404](https://doi.org/10.1103/physrevlett.91.250404).
- [52] E. Tiesinga, S. Kotochigova, and P. S. Julienne.
Scattering length of the ground-state Mg+Mg collision.
Physical Review A, 65(4), apr 2002.
doi: [10.1103/physreva.65.042722](https://doi.org/10.1103/physreva.65.042722).
- [53] H. Knöckel, S. Rühmann, and E. Tiemann.
The $X^1\Sigma_g^+$ ground state of Mg_2 studied by Fourier-transform spectroscopy.
The Journal of chemical physics, 138(094303), 2013.
doi: <https://doi.org/10.1063/1.4792725>.
- [54] Torben Schulze.
Quantum degenerate mixtures of ^{23}Na – ^{39}K and coherent transfer paths in NaK molecules.
PhD thesis, Leibniz Universität Hannover, 2018.
- [55] R. F. C. Vessot, M. W. Levine, E. M. Mattison, E. L. Blomberg, T. E. Hoffman, G. U. Nystrom, B. F. Farrel, R. Decher, P. B. Eby, C. R. Baugher, J. W. Watts, D. L. Teuber, and F. D. Wills.

- Test of Relativistic Gravitation with a Space-Borne Hydrogen Maser.
Physical Review Letters, 45(26):2081–2084, dec 1980.
doi: [10.1103/physrevlett.45.2081](https://doi.org/10.1103/physrevlett.45.2081).
- [56] K. P. Nikolaos and M. A. Weiss.
The relativistic redshift with 3×10^{-17} uncertainty at NIST, Boulder, Colorado, USA.
Metrologica, 40:66–73, 2002.
- [57] Heiner Denker, Ludger Timmen, Christian Voigt, Stefan Weyers, Ekkehard Peik, Helen S. Margolis, Pacôme Delva, Peter Wolf, and Gérard Petit.
Geodetic methods to determine the relativistic redshift at the level of 10^{-18} in the context of international timescales: a review and practical results.
Journal of Geodesy, 92(5):487–516, dec 2017.
doi: [10.1007/s00190-017-1075-1](https://doi.org/10.1007/s00190-017-1075-1).
- [58] Heiner Denker (private communications).
- [59] J Friebe, M Riedmann, T Wübbena, A Pape, H Kelkar, W Ertmer, O Terra, U Sterr, S Weyers, G Grosche, H Schnatz, and E M Rasel.
Remote frequency measurement of the $^1S_0 \rightarrow ^3P_1$ transition in laser-cooled ^{24}Mg .
New Journal of Physics, 13(12):125010, dec 2011.
doi: [10.1088/1367-2630/13/12/125010](https://doi.org/10.1088/1367-2630/13/12/125010).
- [60] A. Pape, O. Terra, J. Friebe, M. Riedmann, T. Wübbena, E. M. Rasel, K. Predehl, T. Legero, B. Lipphardt, H. Schnatz, and G. Grosche.
Long-distance remote comparison of ultrastable optical frequencies with 10^{-15} instability in fractions of a second.
Optics Express, 18(20):21477, sep 2010.
doi: [10.1364/oe.18.021477](https://doi.org/10.1364/oe.18.021477).
- [61] A. Godone and C. Novero.
Lifetime measurement of the Mg I intercombination line.
Physical Review A, 45(3):1717–1721, feb 1992.
doi: [10.1103/physreva.45.1717](https://doi.org/10.1103/physreva.45.1717).
- [62] H.R. Telle, B. Lipphardt, and J. Stenger.
Kerr-lens, mode-locked lasers as transfer oscillators for optical frequency measurements.

- Applied Physics B: Lasers and Optics*, 74(1):1–6, jan 2002.
doi: [10.1007/s003400100735](https://doi.org/10.1007/s003400100735).
- [63] O. Terra, G. Grosche, and H. Schnatz.
Brillouin amplification in phase coherent transfer of optical frequencies over 480 km fiber.
Optics Express, 18(15):16102, jul 2010.
doi: [10.1364/oe.18.016102](https://doi.org/10.1364/oe.18.016102).
- [64] Fritz Riehle.
Optical clock networks.
Nature Photonics, 11:25, January 2017.
- [65] Long-Sheng Ma, Peter Jungner, Jun Ye, and John L. Hall.
Delivering the same optical frequency at two places: accurate cancellation of phase noise introduced by an optical fiber or other time-varying path.
Optics Letters, 19(21):1777, nov 1994.
doi: [10.1364/ol.19.001777](https://doi.org/10.1364/ol.19.001777).
- [66] Gesine Grosche.
Eavesdropping time and frequency: phase noise cancellation along a time-varying path, such as an optical fiber.
Optics Letters, 39(9):2545, apr 2014.
doi: [10.1364/ol.39.002545](https://doi.org/10.1364/ol.39.002545).
- [67] Christian Grebing, Ali Al-Masoudi, Sören Dörscher, Sebastian Häfner, Vladislav Gerginov, Stefan Weyers, Burghard Lipphardt, Fritz Riehle, Uwe Sterr, and Christian Lisdat.
Realization of a timescale with an accurate optical lattice clock.
Optica, 3(6):563, may 2016.
doi: [10.1364/optica.3.000563](https://doi.org/10.1364/optica.3.000563).
- [68] P. A. Williams, W. C. Swann, and N. R. Newbury.
High-stability transfer of an optical frequency over long fiber-optic links.
J. Opt. Soc. Am. B, 25(8):1284–1293, Aug 2008.
doi: [10.1364/JOSAB.25.001284](https://doi.org/10.1364/JOSAB.25.001284).
- [69] S Weyers, V Gerginov, M Kazda, J Rahm, B Lipphardt, G Dobrev, and K Gibble.
Advances in the accuracy, stability, and reliability of the PTB primary fountain clocks.

- Metrologia*, 55(6):789–805, oct 2018.
doi: [10.1088/1681-7575/aae008](https://doi.org/10.1088/1681-7575/aae008).
- [70] S Weyers, V Gerginov, N Nemitz, R Li, and K Gibble.
Distributed cavity phase frequency shifts of the caesium fountain PTB-CSF2.
Metrologia, 49(1):82–87, nov 2011.
doi: [10.1088/0026-1394/49/1/012](https://doi.org/10.1088/0026-1394/49/1/012).
- [71] J Guéna, S Weyers, M Abgrall, C Grebing, V Gerginov, P Rosenbusch, S Bize, B Lipphardt, H Denker, N Quintin, S M F Raupach, D Nicolodi, F Stefani, N Chiodo, S Koke, A Kuhl, F Wiotte, F Meynadier, E Camisard, C Chardonnet, Y Le Coq, M Lours, G Santarelli, A Amy-Klein, R Le Targat, O Lopez, P E Pottie, and G Grosche.
First international comparison of fountain primary frequency standards via a long distance optical fiber link.
Metrologia, 54(3):348–354, may 2017.
doi: [10.1088/1681-7575/aa65fe](https://doi.org/10.1088/1681-7575/aa65fe).
- [72] V Gerginov, N Nemitz, S Weyers, R Schröder, D Griebisch, and R Wynands.
Uncertainty evaluation of the caesium fountain clock PTB-CSF2.
Metrologia, 47(1):65–79, dec 2009.
doi: [10.1088/0026-1394/47/1/008](https://doi.org/10.1088/0026-1394/47/1/008).
- [73] Stefan Weyers (private communications).
- [74] Recommended Values of Standard Frequencies for Applications Including the Practical Realization of the Meter and Secondary Representation of the Definition of the Second, Approved by the CIPM in October 2015.
- [75] Nils Huntemann.
High-Accuracy Optical Clock Based on the Octupole Transition in $^{171}\text{Yb}^+$.
PhD thesis, Gottfried Wilhelm Leibniz Universität Haanover, 2014.
- [76] N. Huntemann, B. Lipphardt, Chr. Tamm, V. Gerginov, S. Weyers, and E. Peik.
Improved Limit on a Temporal Variation of m_p/m_e from Comparisons of Yb^+ and Cs Atomic Clocks.
Physical Review Letters, 113(21), nov 2014.
doi: [10.1103/physrevlett.113.210802](https://doi.org/10.1103/physrevlett.113.210802).

-
- [77] Chr. Tamm, N. Huntemann, B. Lipphardt, V. Gerginov, N. Nemitz, M. Kazda, S. Weyers, and E. Peik.
Cs-based optical frequency measurement using cross-linked optical and microwave oscillators.
Physical Review A, 89(2), feb 2014.
doi: [10.1103/physreva.89.023820](https://doi.org/10.1103/physreva.89.023820).
- [78] N. Huntemann, C. Sanner, B. Lipphardt, Chr. Tamm, and E. Peik.
Single-Ion Atomic Clock with 3×10^{-18} Systematic Uncertainty.
Physical Review Letters, 116(6), feb 2016.
doi: [10.1103/physrevlett.116.063001](https://doi.org/10.1103/physrevlett.116.063001).
- [79] N. Huntemann, M. Okhapkin, B. Lipphardt, S. Weyers, Chr. Tamm, and E. Peik.
High-Accuracy Optical Clock Based on the Octupole Transition in $^{171}\text{Yb}^+$.
Physical Review Letters, 108(9), feb 2012.
doi: [10.1103/physrevlett.108.090801](https://doi.org/10.1103/physrevlett.108.090801).
- [80] GUM.
Guide to the Expression of Uncertainty in Measurements, ISO/TAG 4. (ISO,1993) (corrected and reprinted 1995) in the name of the BIPM, IEC, IFCC, ISO, UPAC, IUPAP, and OILM , ISBN 92-67-10188-9,1995.
- [81] Hidetoshi Katori, V. D. Ovsiannikov, S. I. Marmo, and V. G. Palchikov.
Strategies for reducing the light shift in atomic clocks.
Physical Review A, 91(5), may 2015.
doi: [10.1103/physreva.91.052503](https://doi.org/10.1103/physreva.91.052503).
- [82] R.C. Brown, N.B. Phillips, K. Beloy, W.F. McGrew, M. Schioppo, R.J. Fasano, G. Milani, X. Zhang, N. Hinkley, H. Leopardi, T. H. Yoon, D. Nicolodi, T.M. Fortier, and A.D. Ludlow.
Hyperpolarizability and Operational Magic Wavelength in an Optical Lattice Clock.
Physical Review Letters, 119(25), dec 2017.
doi: [10.1103/physrevlett.119.253001](https://doi.org/10.1103/physrevlett.119.253001).
- [83] F. Diedrich, J. C. Bergquist, Wayne M. Itano, and D. J. Wineland.
Laser Cooling to the Zero-Point Energy of Motion.
Physical Review Letters, 62(4):403–406, jan 1989.
doi: [10.1103/physrevlett.62.403](https://doi.org/10.1103/physrevlett.62.403).

- [84] O. N. Prudnikov, D. V. Brazhnikov, A. V. Taichenachev, V. I. Yudin, A. E. Bonert, R. Ya. Il'enkov, and A. N. Goncharov.
Quantum treatment of two-stage sub-Doppler laser cooling of magnesium atoms.
Physical Review A, 92(6), dec 2015.
doi: [10.1103/physreva.92.063413](https://doi.org/10.1103/physreva.92.063413).

LIST OF FIGURES

1.1	SI base units	4
1.2	Principle of an optical clock	5
2.1	Levelscheme of magnesium	10
2.2	Scheme of the science chamber	12
2.3	Homogeneous magnetic field	14
2.4	Level scheme of the triplet system	19
2.5	Lattice Potential	21
2.6	Scheme of the lattice set up	22
2.7	Experimental sequence	23
2.8	ULE Cavity	25
2.9	Experimental sequence	26
2.10	Scan of a 51(3) Hz broad clock transition	27
2.11	Scheme of the stabilization of the clock laser to the clock transition	28
3.1	Polarizabilities for Mg clock levels	31
3.2	AC Stark shift measurement	32
3.3	Determined magic Wavelength	32
3.4	Measurement of higher order AC Stark shift	34
3.5	Clock laser and lattice set up	35
3.6	AC Stark measurement	36
3.7	Data of the ^{24}Mg frequency measurement compared against the H10 maser at the PTB and the change in frequency due to the changing probe AC Stark shift	37
3.8	Relevant levels of magnesium of BBR calculations	39
3.9	Temperature sensors at the science chamber	40

3.10	Second order Zeeman measurements	43
3.11	Linebroadening due to occupation of higher vibrational states	45
3.12	Cross section of ground state Mg+Mg collisions	47
3.13	Measurement of the density shift	48
3.14	Geoid	49
3.15	Picture of the reference Point	49
3.16	Position of the reference Point at the LUH	50
4.1	Setup of a transfer beat	54
4.2	Scheme of the link between the magnesium lattice clock at the Institut für Quantenoptik, LUH and the clocks at the PTB in Braunschweig	56
4.3	Optical Fiber network in Europe	57
4.4	Link setup	58
4.5	Allan standard deviation of the frequency comparison of the CSF2 at the PTB and the SYRTE-FOx, at the LNE-SYRTE, Observatoire de Paris	59
4.6	Allan deviation of the ^{24}Mg lattice clock versus the CSF2 at the PTB	60
4.7	Allan deviation of the frequency comparison between the Mg lattice clock and the Yb ion clock at the PTB	61
4.8	Frequency of the clock transition	63
5.1	Tilted Potential	66
5.2	Operational magic wavelength for mercury	70
5.3	Simulations on the operational magic wavelength for magnesium	71
5.5	Simulations on sub-Doppler cooling of magnesium	73
5.4	Scheme of sideband cooling	73
5.6	Extend ^{25}Mg - Level scheme	77
5.7	Extend ^{24}Mg - Level scheme	79
5.8	Difference of both data sets sampled at the frequency comparison with probe beam intensities of 3 mW and 20 mW (<i>blue</i>) and the fitted smoothing spline (<i>red</i>) used for correction of the AC Stark frequency shift.	81

LIST OF PUBLICATIONS

Publications in pre-reviewed journals:

- A. P. Kulosa, D. Fim, K. H. Zipfel, S. Rühmann, S. Sauer, N. Jha, K. Gibble, W. Ertmer, E. M. Rasel, M. S. Safronova, U. I. Safronova, S. G. Porsev
"Towards a Mg Lattice Clock: Observation of the $^1S_0 - ^3P_0$ Transition and Determination of the Magic Wavelength",
Physical Review Letters, 115(24), dec 2015
DOI: 10.1103/PhysRevLett.115.240801

- M. Riedmann, H. Kelkar, T. Wübbena, A. Pape, A. Kulosa, K. Zipfel, D. Fim, S. Rühmann, J. Friebe, W. Ertmer, and E. Rasel
"Beating the density limit by continuously loading a dipole trap from millikelvin-hot magnesium atoms",
Physical Review A, 86(4), oct 2012
DOI: 10.1103/PhysRevA.86.043416

Dominika Fim

Curriculum Vitae

Krasseltweg 56
30657 Hannover

Personal Details

Date of birth October 26, 1978
Place of birth Beuthen, Poland
Marital status married

Study and Diploma Thesis

since 11/2011 **Doktoral candidate at the Institut für Quantenoptik.**
09/2010 – 09/2011 **Diploma thesis**, Title: *Entwicklung von Lasersystemen zur optischen Speicherung von ^{24}Mg bei der magischen Wellenlänge*, Supervisor: Prof. Dr. E. M. Rasel.
10/2005 – 11/2011 **Study of Physics**, (Degree: *Diploma*), Leibniz Universität Hannover.

Higher Education

08/2004 – 07/2005 **Specialized Secondary School, Berufsoberschule Technik Hannover**, (Degree: *"Allgemeine Hochschulreife"-General matriculation standard*).
08/2003 – 07/2004 **Technical Secondary School, Fachhochschule Hildesheim**, (Degree: *"Fachhochschulreife"-Advanced technical college certificate*).

Train and Work Experience as Dental Technician

02/1999 – 07/2003 **Employed as dental technician.**
09/1995 – 01/1999 **Training as dental technician**, (Degree: *Journeyman's certificate*).

Education

09/1991 – 07/1995 **Secondary school, Gottfried-Linke-Realschule, Salzgitter**, (Degree: *Secondary level I*).

Research Assistant

02/2008 – 10/2010 **Research assistant at the Institut für Quantenoptik,
*Leibniz Universität Hannover.***

Study abroad

08/2009 – 09/2009 **Australia.**

Language

German Native language

Polish Native language

English Proficient

Spanish Basic knowledge

DANKSAGUNG

Als erstes möchte ich mich bei Prof. Dr. Ernst M. Rasel dafür bedanken, dass er mir die Möglichkeit gegeben hat in seiner Gruppe zuerst eine Diplomarbeit anzufertigen und anschließend zu promovieren. Ernst hat großes Interesse und Unterstützung gezeigt in Bezug auf experimentelle und physikalische Fragestellungen, in der fachlichen Weiterbildung durch das Ermöglichen von den Teilnahmen an Konferenzen, Workshops und Schulungen, aber auch bei persönlichen Belangen. Ich möchte mich auch für seine aufrichtige Freude und das Lob bedanken, wenn es positive Nachrichten gab, aber auch für seine Geduld und Ansporn, wenn diese etwas auf sich warten ließen.

Als nächstes möchte ich Prof. Dr. Ertmer danken, der bereits als Prüfer in einer mündlichen Prüfung und Koreferent für die Diplomarbeit mitgewirkt hat und auch jetzt das Koreferat für diese Doktorarbeit übernommen hat. Prof. Ertmer hat immer Interesse für das Magnesium Experiment gezeigt und hat dieses wo nötig und möglich unterstützt.

Des Weiteren, möchte ich Prof. Dr. Kai Bongs von Univeristy of Birmingham für die freundliche Übernahme des externen Koreferats bedanken. Aber auch für die freundliche Zusammenarbeit, Koordination und Unterstützung innerhalb des FACT Programms. At this point, I would also like to thank Yesphal Singh: the cooperation with you took place in a friendly atmosphere and was always very productive.

Mein Dank gilt ebenfalls an Prof. Dr. Klemens Hammerer für die Übernahme der Leitung des Prüfungsvorsitzes.

Ein großen Beitrag zum Gelingen dieser Arbeit, insbesondere für die Durchführung der Frequenzmessung, haben mehrere Arbeitsgruppen an der PTB geleistet. Dafür möchte ich mich Bedanken, und zwar bei:

- Dr. Christian Lisdat und seinen Teammitgliedern, die uns bei dem Vergleich gegen die Strontium Uhr unterstützt haben und einen großen Beitrag zur Vorbereitung auf die Frequenzmessung geleistet haben. Insbesondere an Dr. Ali Al-Masoudi, der das Strontium-Experiment „online“ -gehalten hat, wenn wir es benötigt haben.

- Dr. Gesine Grosche für Ihre Arbeit an einem stabilen Frequenztransfer und der Ausweitung nach Hannover. An Dr. Alexander Kuhl und Dr. Thomas Waterholter, die den Faserlink nach Hannover instandgehalten haben sowie neue Techniken implementiert haben. Ein großer Dank gilt Dr. Sebastian Koke, der Klaus Zipfel und mich bei der Auswertung der Messkampagne unterstützt hat.
- Dr. Stefan Weyers für den Abgleich gegen einen Cäsium Frequenzstandard, sowie den Austausch und Erläuterungen bezüglich der Auswertungen der Messkampagne.
- Dr. Ekkehard Peik und Nils Huntemann für das Ermöglichen eines Frequenzvergleich gegen die Ytterbium-Ionenuhr.
- Dr. Andreas Bauch für die Bereitstellung eines passiven Wasserstoff-Masers für die Messkampagne sowie Unterstützung bei der Instandhaltung dessen.

Am Magnesium Experiment habe ich zuerst als hilfswissenschaftliche Mitarbeiterin während des Physikstudiums angefangen zu Arbeiten. Vom ersten Tag an habe ich viel Unterstützung und ein freundliches Arbeitsklima von den Teammitgliedern erfahren. Hierfür möchte ich mich bedanken bei Dr. Jan Friebe, Dr. Matthias Riedmann und Dr. Andre Pape. Aber auch bei den Teammitgliedern die mich später während der Diplomarbeit und Doktorarbeit begleitet haben möchte ich mich für die tolle Zusammenarbeit bedanken: Bei Dr. Temmo Wübbena für seine positive Einstellung, Dr. André Kulosa für seine ebenfalls sehr fröhliche Art, positive Einstellung und seine musikalischen Untermalungen.

Mein besonderer Dank gilt den Teammitgliedern die mich zuletzt begleitet haben: Waldemar Friesen-Piepenbrink, Nandan Jha, Steffen Sauer, Dr. Steffen Rühmann und Dr. Klaus Zipfel. Vielen Dank für eure Unterstützung im Laboralltag, der durchaus fordernd sein kann. Für eure Hilfe während der Frequenzmessung, die nicht selbstverständlich war, für die zahlreichen Noteinsätze: wenn man von einem Tag auf den anderen etwas auf die Beine stellen muss und in diesen Momenten alle an einem Strang gezogen haben. Danke, dass die gegenseitige Unterstützung, im Laboralltag aber auch bei allem anderen selbstverständlich ist. Vielen Dank!

Des Weiteren möchte ich mich bei allen weiteren Kollegen am Institut bedanken. Für eure außerordentliche Hilfsbereitschaft, den wissenschaftlichen Austausch sowie das familiäre Umfeld, welches ihr ausmacht. Insbesondere möchte ich mich bei allen Bedanken, die mir persönlich bei technischen Fragen mit Rat und Tat zu Seite standen. Des Weiteren möchte ich mich bei Kai-Martin Knack, der mir mit seiner Expertise im Bereich der Elektronik viel beigebracht hat und an der

Umsetzung viele Projekte maßgeblich beteiligt war bedanken. Ein Dank gilt ebenfalls dem Team der Feinmechanik Werkstatt, dem Sekretariat, insbesondere Frau Göldner- Pauer, sowie Frau Ohlendorf.

Um diese Arbeit zu Verfassung benötigte ich einen Tapetenwechseln. Zuflucht konnte ich in den Büros anderer Arbeitsgruppen finden: Für eure Gastfreundlichkeit möchte ich mich Bedanken bei: Sebastian, Baptist, Knut, Kai, Maike, Holger, Sina, Nina und Hendrik.

Mein herzlicher Dank gilt allen die aus Kommilitonen und Arbeitskollegen, Freunde wurden und dass ihr mich in dieser Zeit begleitet habt. Danke, nicht nur für die vielen schönen Momente, sondern auch für die besonderen Momente die mir für immer in Erinnerung bleiben. Schön das es euch gibt: Torben, Sebastian, Maral, Kulli, Klaus, Steffen S. Steffen R, Waldemar, Nandan, Phillip, Henning, Baptist, Knut, Holger, Felix, Robin, Wolfgang.

Zuletzt möchte ich Jens, meinem Engel Florian, Mama, Papa, Schnauzkuh, Elodie, Kenny, Olli, Annelie, Jenny, Natalia und Christina vom ganzen Herzen für eure Unterstützung, Motivation, den Rückhalt und eure Aufmunterung danken.